Laser Interference Fringe Tomography - A Novel 3D Imaging Microscopy Technique

by

Farnoud Kazemzadeh

A thesis
presented to the University of Waterloo
in fulfillment of the
thesis requirement for the degree of
Master of Applied Science
in
Systems Design Engineering

Waterloo, Ontario, Canada, 2011

I hereby declare that I am the sole author of this thesis. This is a true copy of the thesis, including any required final revisions, as accepted by my examiners.

I understand that my thesis may be made electronically available to the public.

Abstract

Laser interference fringe tomography(LIFT) is within the class of optical imaging devices designed for volumetric microscope applications. LIFT is a very simple and cost-effective three-dimensional imaging device which is able to reliably produce low-quality imagery. It measures the reflectivity as a function of depth within a sample and is capable of producing three-dimensional images from optically scattering surfaces. The first generation of this instrument is designed and prototyped for optical microscopy. With an imaging spot size of 42 μm and a 180 μm axial resolution kernel, LIFT is capable of producing one- and two- dimensional images of various samples up to 1.5 mm thickness. The prototype was built using commercial-off-the-shelf components and cost $\sim$ \$1,000. It is possible that with effort, this device can become a reliable, stable, low-quality volumetric imaging microscope to be readily available to the consumer market at a very affordable price.

This document will present the optical design of LIFT along with the complete mathematical description of the instrument. The design trade-offs and choices of the instrument are discussed in detail and justified. The theoretical imaging capabilities of the instrument are tested and experimentally verified. Finally, some imaging results are presented and discussed.

Acknowledgments

Contents

List of Figures

xi

List of Tables

Chapter 1

Introduction

Recently, the development and improvement of imaging technologies has become more prolific. The applications of these technologies vary from resolving sub-cellular structures in biological applications (e.g., a confocal microscope (CM)) to detecting suspicious objects while going through airport security (e.g., an X-Ray backscatter imager). Over the past two decades the field of biomedical and diagnostic imaging has witnessed a fast moving trend in the development and application of imaging instruments. Imaging instruments which were in their infancy not too long ago are now main stream imaging techniques used for diagnostic medicine. Other applications, however, seem to have stagnated with technologies developed decades ago.

Imaging is done over a wide range of wavelengths, from long radio wavelengths (Magnetic resonant imaging (MRI)) to short X-Ray wavelengths (X-Ray imager). Imaging techniques vary depending on what part of the electromagnetic spectrum is used for imaging. Different imaging techniques are referred to as *imaging modality*. Some of the most prevalent imaging techniques along with their main applications are shown in Table 1.1.

Table 1.1: Various imaging modalities along with their popular applications. Note: this is a relevant selection of imaging modalities and their applications.

Modality	Application
MRI	full-body medical imaging, improvised explosive device detection
X-ray	imaging bone structure, weld inspection, airport and border security
OCT	opthalmology, tissue biopsy, material thickness/density analysis
Ultrasound	medical diagnostic and therapeutic procedures, internal flaws in material
Microscopes	biological science, cellular and sub-cellular biology, chemistry

An application that is shared by all the modalities mentioned in Table 1.1 is medical imaging. A common theme shared among all of these devices is their high price of procurement, maintenance and operation. A very common metric used for classifying an imaging device is the imaging resolution. Figure 1.1 shows a plot of the price of most widely used imaging devices as a function of their imaging resolution. Depending on the required resolution of the imaging application, a device exists to acquire the image. This figure also shows that there exists no imaging solution less expensive than $\sim$ \$7,000, which is denoted by the dashed line in Figure 1.1.
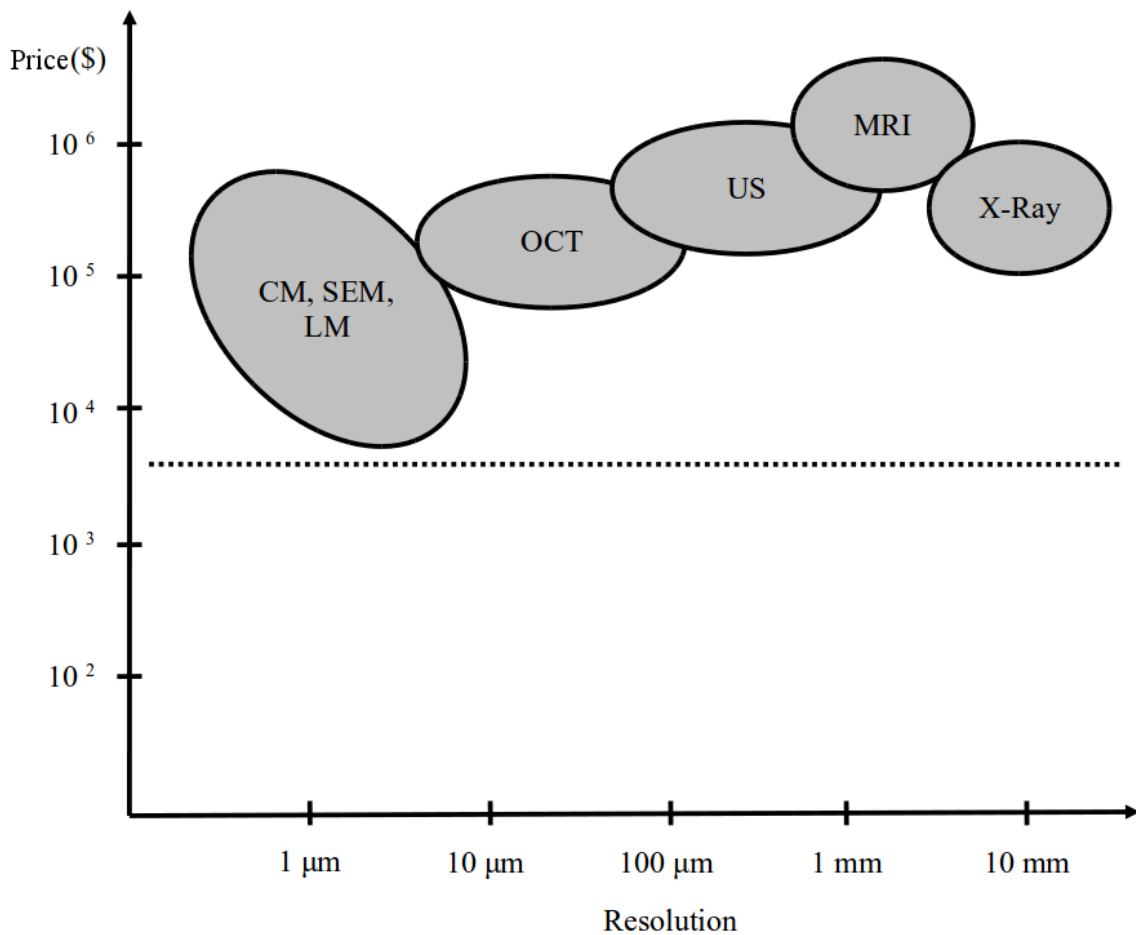
Figure 1.1: A graphical representation of the cost of a device and its imaging capability (resolution) of X-Ray, MRI, ultrasound (US), optical coherence tomography (OCT), CM, scanning electron microscope (SEM), and light microscope(LM) [1].

For most of the imaging modalities, increased resolving power usually comes at the

cost of reduced imaging depth [10]. As an example, MRI has the capability to image the entire human body at millimeter resolution whereas a CM can image at micron or sub-micron resolution but can only image to a few micron depth. All of the imaging modalities mentioned above are capable of acquiring three-dimensional images with the exception of the microscopes. It appears that at the highest imaging resolution, volumetric imaging is sacrificed.

Optical interferometric imaging technologies have been used in astronomy since the early 1900's. In the late 1900's this technology was adapted for smaller-scale aplications such as medical imaging. A device such as an OCT was invented in the mid 1990's for examining and studying ocular diseases [9, 13]. In recent years the value of this device has been realized and its applications have been expanded to many other fields mentioned previously.

The operating principle of optical interferometry is that the intensity of the light originating from a source is split into two or more parts, where each part then travels a different distance before it is recombined. The result of the recombination is an interference pattern that conveys information about the source. If this principle were to be applied for microscopy, the sample of interest will have to be luminescent. Since inanimate objects, dead biological tissue, and live tissue are not luminous in optical wavelengths, optical interferometric microscopy becomes very difficult. This issue is overcome by illuminating these objects and interfering the light that is reflected or backscattered from them.

The result of interfering the backscattered light from a sample is a one-dimensional intensity map which corresponds to the amplitude of the reflected/backscattered light as a function of depth into the sample. This is referred to as the *depth profile* or an *A-scan*. Assembling many A-scans will produce a two-dimensional image called a *B-scan*, and by assembling many B-scans a three-dimensional volumetric image of the sample can be acquired. An optical interferometer microscope such as an OCT system operates based on the above description.

There has been increasing interest in using a volumetric imaging device, such as OCT, for optical biopsy and pathological studies of tissue [26, 12]. This shows the importance and versatility of such devices for applications that they may not have been originally be designed for. However, the high price and the complexity of operation and maintenance of

3

these instruments prevents the exploration of uses of these devices for other applications. Almost all of these devices will have to be operated by a trained technician, require routine maintenance, and are to be operated out of a tightly controlled environment.

Laser interference fringe tomography (LIFT) is a tomographic interferometric imaging instrument proposed for volumetric microscopy. LIFT uses the principle of coherence in interferometry to produce 'depth profiles' and is capable of producing three-dimensional images. LIFT is designed to address the lack of any imaging technique that can provide a reasonable resolution at extremely low cost, a low quality imaging device. LIFT is designed to be a very simple instrument using a minimal number of optical elements along with an inexpensive light source.

Motivated by the operation principles of an optical interferometric volumetric imaging device, the topic of this thesis is to propose a new imaging modality along with a new instrument. This device is designed to be simple to use and maintain as well as being affordable. The imaging capability of the device is to be initially probed in this document but it is designed for imaging resolution of tens to hundreds of microns with medium to high imaging depth capability.

The following chapters will describe the scientific fundamentals and design and performance of LIFT. Chapter 2 will provide the reader with the fundamental optical concepts integral to the understanding of LIFT. In Chapter 3 the optical design of the instrument is described and the mathematics behind LIFT are presented. This chapter then goes on to examine the design constraints on the instrument and attempts to overcome these obstacles. Chapter 4 outlines the imaging and performance capabilities of LIFT, lays out an image acquisition procedure, briefly describes the data reduction and processing pipeline, and presents some imaging test done by the LIFT prototype. Chapter 5 summarizes the document.

Chapter 2

Background

In this chapter a few concepts integral to the remainder of this document are described and discussed. The topics in this chapter are divided into two main sections: optical imaging and interferometry. The topics discussed are: interaction between light and a material and the paraxial approximation to geometrical optics. Under the umbrella of interferometry which exploits the wave treatment of light, the concept of interference is introduced, interference between two light waves are described, and finally an example of one of the first interferometers is presented. The imaging modality and the device described in this document will draw heavily from the information presented in this chapter.

2.1   Optical Imaging

Optical imaging is simply recording the light intensity on a camera in optical (visible) wavelengths. Passive optical imaging is done when the electromagnetic wave is produced by the object of interest and received by a detector. Active optical imaging is when the object is illuminated by a light source and the measured quantity is the returning light that has interacted with the object of interest. The theoretical performance of these active imaging instruments can be characterized fundamentally, based on the optical elements used in the device itself. This section will discuss the most significant of these characterization criteria.

2.1.1 Light-Material Interaction

In general, light rays generated by a source will propagate in the medium and encounter boundaries when arriving at new media. When light interacts with a medium it can be directly reflected from the surface of a material, which is referred to as specular reflection. It can travel directly through a material without interacting with it, which is referred to as direct transmission. Other than the two outcomes mentioned above, light will interact with the material and be scattered inside the material. The light is then destined to either be absorbed by the material or emerge via diffuse reflection or transmission [5].

Light is said to be interacting when it encounters a change in the index of refraction

$$n = \sqrt{\epsilon\,\mu}. \tag{2.1}$$

The refractive index of a material is purely based on the material's electric permittivity (ϵ) and electric permeability (μ) relative to that of the vacuum. These values differ for different materials and are well understood for almost all materials. At these interfaces, light is destined to one or all of the above-mentioned situations. For reference, the index of refraction of air is ~ 1.0 and biological tissue ~ 1.3.

2.1.2 Paraxial Optics

Light rays that arrive at optical components at small angles are referred to as paraxial rays [3]. The region that encompasses these rays is the paraxial region in geometrical optics. Computations of propagation of light rays can be significantly simplified by employing a few approximations in the theory.

Snell's law of refraction

$$n_a\,sin\,\theta_a = n_b\,sin\,\theta_b, \tag{2.2}$$

describes the transmission or reflection of light rays when interacting with a material of a different index of refraction. Snell's law takes into account the angle at which the light illuminates the boundary between the two differing refractive indexes. The presence of the sine function in Equation 2.2 makes the computation of this phenomena rather complex. For small θ_a and θ_b, a small angle approximation can be employed and Snell's law takes

the form

$$n_a \; \alpha_a = n_b \; \alpha_b. \tag{2.3}$$

where the paraxial angle is defined as $\alpha = \theta \simeq sin\ \theta$. In the paraxial region the tangent of a shallow angle can be approximated as the sine of that angle and ultimately be approximated by the paraxial angle α. The cosine of a paraxial angle is approximated to be 1.

The small angle approximation in the paraxial region should only be employed for $\theta \leq 10°$ [3]. Although according to Figure 2.1 the percent error in this approximation is negligible ($< 1\%$) for $\theta < 15°$, this approximation should only be employed for angles in the paraxial region. An error of 1% can be very significant if the light rays travel large distances and the sine and tangent of an angle in the paraxial region can no longer be approximated by a paraxial angle anymore.
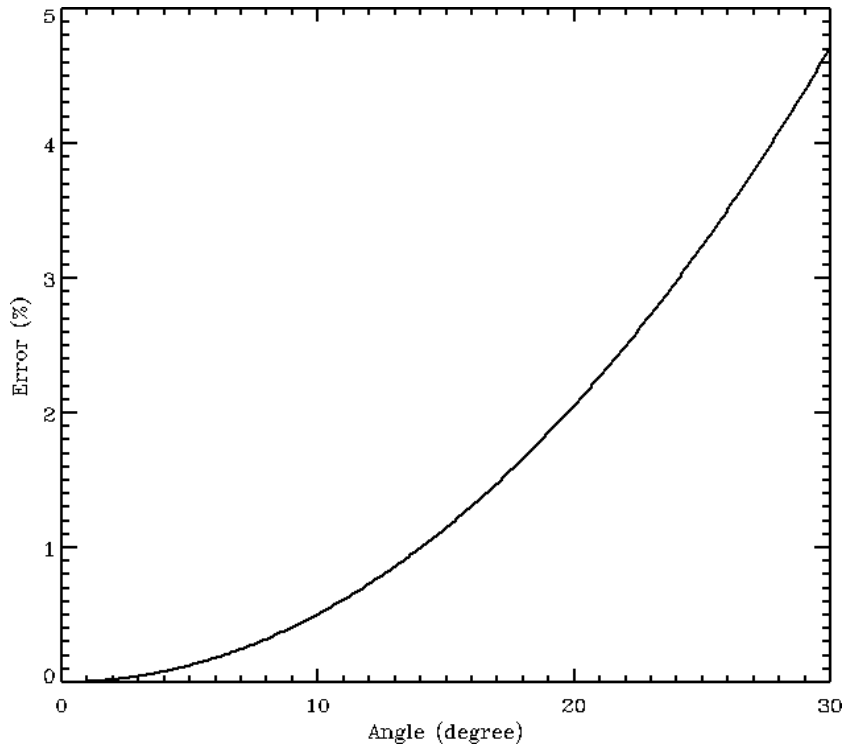
Figure 2.1: A plot of error in the small angle approximation of $\theta = sin\ \theta$ as a function of θ.

2.1.3 Imaging Central Wavelength

the light source is very important in imaging microscopy. Even though any imaging system can be tailored to satisfy any requirements, one has to be cognoscente of the trade-offs that arise from any decision. The choice of wavelength, for example, is very important which will be shown in the following sub-sections. It has direct impact on the imaging resolution and the depth of field of the microscope. The choice of wavelength will also dictate the material that is utilized in the instrument. For example, in the visible wavelengths the optical elements will be made of glass but at extreme infra-red and ultraviolet wavelengths, the optical elements will be made of silicon carbide and aluminum lithium-fluoride [28]. In medical imaging there is a window between 650-1300 nm where scattering from tissue is minimized and significant depth can be probed before any major absorption event [24, 41]. In short, the type of application will determine the central wavelength of the light source utilized in an imaging instrument.

2.1.4 Gaussian Beam Optics

Ideally the output intensity profile of a laser source is Gaussian. Although reality is far from ideal, it turns out that the Gaussian approximation of the intensity profile of a laser source is sufficient for any first-order analysis of the behavior of the beam. The output of most laser sources available through any optical equipment provider is a collimated pencil beam, which means a planar light train of a constant diameter exits the laser. However, the plane wavefronts begin to develop a curvature the farther the beam travels from the source, as well as the beam size diverges ever so slightly. In light of this it is important to minimize the distance that the laser beam travels before being used in the optical system. Using the Gaussian beam optics framework the size of a focused laser beam can be determined and a method of 'cleaning' the beam is shown. The idea of depth of focus, which is an important aspect in microscopic imaging, is presented.

Spot Size

When a collimated (planar) beam of a circular aperture, uniformly illuminated (constant intensity profile) is brought to focus using a lens, the theoretical result is the Fraunhofer

diffraction of a circular aperture [7]. This pattern has a bright circular region in the center, known as the 'Airy disk' and is surrounded by a series of concentric bright rings, Figure 2.2. The functional form of it is the first-order Bessel function of the first kind and is simply modeled by $\frac{sin^2(\theta)}{\theta}$ [20]. In other words, the electric field observed at the focal point of a lens is the Fourier transformation of the field before going through the lens, multiplied by the aperture function of the lens [17]. The Fourier treatment of light and its interactions with optical elements is beyond the scope of this thesis.
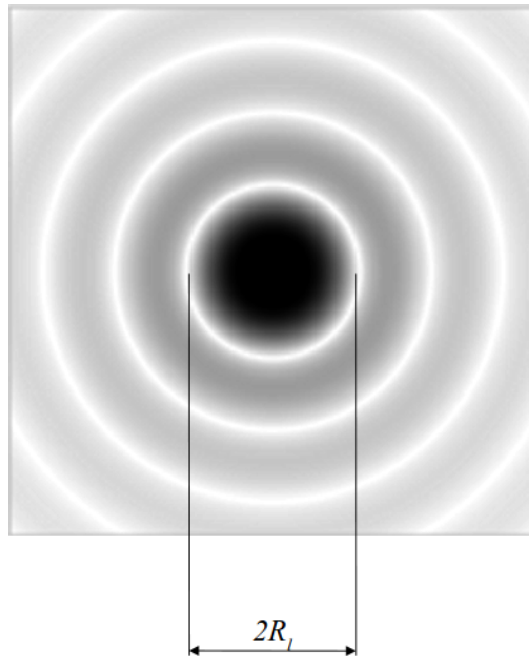
Figure 2.2: Airy pattern due to Fraunhofer diffraction of a uniformly illuminated circular aperture, with the spot size denoted by 2R$_l$.

The diameter of the central lobe of the Airy pattern, the Airy disk, is denoted by 2R$_l$ in Figure 2.2. It is simply limited by the optical diffraction limit and is determined by [7]

$$2R_l = \frac{2.44 \, \lambda_\circ \, f}{n \, D},$$
(2.4)

where R_l is the diameter of the spot, $\lambda_\circ$ is the wavelength of the light, f is the focal length of the lens, n is the refractive index of the medium, and D is the diameter of the incoming beam.

In imaging instruments, the quantity R$_l$ is referred to as the theoretical lateral resolution of the instrument or the beam waste. The actual lateral resolution is in all cases larger

9

than the diffraction limited lateral resolution. An instrument with $2R_l$ spot size is able to probe structure of R_l size. The parameters most easily manipulated to control lateral resolution are wavelength of light, the focal length of the focusing lens, and the diameter of the incoming beam.

Depth of Field

The depth of focus is the amount of defocus that the receiving object may undergo before the recorded image becomes unacceptable [16]. When a beam of light is focused using a lens, the beam does not come to focus at a point. The diameter of the beam is narrowed until it reaches its diffraction limit (Equation 2.4) at the focal plane and then it begins to expand out again.
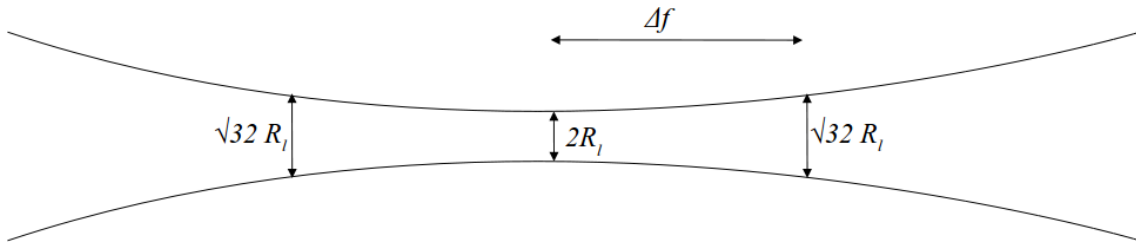
Figure 2.3: Change in wavefront diameter going toward and through the focal plane.

Figure 2.3 shows the convergence and divergence of the beam going toward and past the focal plane, respectively. In this figure, Δf is the Rayleigh range and is defined to be the distance between where the focused beam diameter is $\sqrt{32}R_l$ going toward and away from the focal plane [20]. This quantity is mathematically described for any optical setup by [11, 34]

$$\Delta f = \pm \frac{1.22^2 \ \pi \ \lambda_\circ \ f^2}{n \ D^2}.$$

(2.5)

Outside of the region of $f \pm \Delta f$ the lateral resolution of the device suffers because the beam size is diverging from the focused size. Based on the above relationship it is clear that with a smaller spot size (higher lateral resolution) comes a smaller depth of focus. Finding the fine balance between the two is strictly application dependent and is addressed in later phases of instrument building.

2.2 Interferometry

Interferometry is the study of interactions between waves such as light, sound, etc. The interference patterns provide subtle and precise information about the wavefronts that are interfering. By studying the interference pattern, information about the origin of the wavefronts can be discerned and some properties of the source of the wavefronts can be studied. Interferometers enable measurements not otherwise achievable through direct imaging. Interferometry has many scientific and industrial applications such as metrology, surface profiling, astrophysics, etc.

An interferometric device divides the incoming beam of light into two beams and re-combines them to produce an interference pattern. There are in general two methods of splitting a light beam. In one, the beam is split by passing through a partially reflective-transmitive element, referred to as the amplitude-splitting method. An examples of an amplitude-splitting interferometers is the Michelson [2, 7, 19, 22, 25]. Alternatively, the incoming beam is sub-sampled by placing two apertures in-line with each other in the path of the beam, which is referred to as the wavefront-splitting method. an example of this method is Young's double-slit interferometer [7, 25]. After the division of the original beam, the resulting two beams will have to be overlapped in order to produce interference. All interferometers operate based on one of the above-mentioned methods, albeit amplitude-splitting interferometers seem to be the most widely used.

2.2.1 Interference of Light

Light interacts with the physical environment through scattering (reflection), refraction, and diffraction but light can also interact with itself through interference. Interference is the super-position of two or more light waves or in general, electromagnetic waves [19]. If two beams of light originating from the same source were superposed, the expectation would be to see the sum of their irradiances in the region of overlap of the two beams but this is not the case. In fact, the phenomenon observed in the region of overlap is a pattern of alternating dark and light bands occurring periodically, called interference fringes [2, 7, 25].

Interference theory exploits the wave-like nature of light. Interference will be discussed

more generally in terms of coherence in a later section. In this section it is assumed that the interfering electric fields are planar and monochromatic. Plane waves are produced by a monochromatic point source at infinity and are approximated very well by a collimated light beam emerging from a lens [19]. The superposed light waves are represented in their complex notation by

$$\mathbf{E}(\mathbf{r}, t) = E_0 \ exp[i(\omega_\circ t - \mathbf{k}_0 \cdot \mathbf{r} + \varphi_0)] + E_1 \ exp[i(\omega_\circ t - \mathbf{k}_1 \cdot \mathbf{r} + \varphi_1)], \qquad (2.6)$$

where E_n is the amplitude of the electric field of the beam, the mean angular frequency of the electric field is $\omega_\circ = 2\pi\nu_\circ$ which is related to the mean frequency of the light beam, $\mathbf{k}_n = \frac{2\pi}{\lambda}$ is the wavenumber, and φ_n is the initial phase of each electric field. The total phase of the electromagnetic wave can be represented by $\phi_n = \varphi_n - \mathbf{k}_n \cdot \mathbf{r}$.

The two interfering waves are denoted as 0 and 1. The physical observation of the electromagnetic wave is done by measuring the square of the real part of the electric field, $\Re\{\mathbf{E}^2\}$. Since the fluctuations of the optical frequency are much faster than the integration time of any optical detector, the observable measured by a detector is the time average of the square of the real part [25]. The observed intensity is

$$I = \epsilon \ \mu < \Re\{\mathbf{E}^2\} >, \qquad (2.7)$$

with ϵ and μ are the permitivity and the permeability of the medium that the waves exist in respectively. The angled brackets denote time-average of the observed electric field.

Using the complex notation of $T^2 = T \cdot T^*$ with * denoting the complex conjugate, so $E = E \cdot E^*$. Therefore, the measured intensity of the two superposed waves is represented as

$$I = \epsilon \ \mu \ [|\mathbf{E}_0|^2 + |\mathbf{E}_1|^2 + \Re\{\mathbf{E}_0 \cdot \mathbf{E}_1^* + \mathbf{E}_0^* \cdot \mathbf{E}_1\}], \qquad (2.8)$$

which can alternatively be written as

$$I = \epsilon \ \mu \ [I_0 + I_1 + \sqrt{I_0 I_1} \ \Re\{e^{2i(\omega t(\phi_1 - \phi_2))}\}]. \qquad (2.9)$$

Ultimately, the interference can be represented in terms of

$$I = \epsilon \ \mu \ [I_0 + I_1 + 2\sqrt{I_0 I_1} \ cos(\Delta\phi)], \qquad (2.10)$$

where $\omega t(\phi_1 - \phi_2) = \Delta\phi$ is the total phase difference between the two light waves which gives rise to the sinusoidal interference pattern. The maximum intensity is observed when

the total phase difference is an even-integer multiple of π and minimum intensity is observed when it is an odd-integer multiple of π.

The first two terms in Equation 2.10 are simply the sum of the intensity of each individual plane wave. The third term is the vector dot product between the two waves which manifests itself in the polarization and the initial phase of the plane waves [7]. The relative difference in time of flight or the distance traveled by each plane wave can also give rise to a phase difference. When the interferometric term is greater than zero it is referred to as constructive interference and when smaller than zero it is referred to as destructive interference [25].

The visibility of the interference pattern is described by

$$\mathcal{V} = \frac{I_{max} - I_{min}}{I_{max} + I_{min}}, \tag{2.11}$$

where I_{max} and I_{min} are the maximum and minimum intensity of the fringe pattern as observed on the detector. Equation 2.11 essentially describes the dynamic range of the interference pattern and normalizes it by the average intensity value. The visibility will have a value between 0 and 1 and will be maximized when the two waves have equal intensities [19].

2.2.2   Optical Coherence and Interference

The treatment of interference in the previous section was for completely monochromatic light with perfect coherence. Coherence in general terms describes the correlation between two or more waves. Optical coherence means that the electromagnetic radiation, light, is of the same origin. Two main manifestations of coherence are temporal and spatial coherence [25, 32, 33]. Crudely, temporal coherence means that the radiation has been emitted at the same time, and spatial coherence means that the radiation has been emitted from the same location. For any observable interference to occur the light waves have to be both temporally and spatially coherent [33]. The concept of coherence is paramount in describing interference of quasi-monochromatic light sources such as lasers, and low coherence light sources such as super luminescent diodes.

Temporal Coherence

Formally, temporal coherence is a length of time outside of which the delay between the two beams, as a result of time of flight difference, will not produce any interference pattern. The quantity, coherence time is defined as [33]

$$\Delta t \sim \frac{1}{\Delta \nu}, \tag{2.12}$$

where $\Delta \nu$ is the bandwidth of the light or the full-width-half-maximum. According to Equation 2.12, the larger the bandwidth of the light source the shorter the coherence time and the less coherent the light is. And the corresponding path difference over which the two waves will maintain their coherence is

$$\Delta l \sim (\frac{\lambda_\circ}{\Delta \lambda}) \lambda_\circ, \tag{2.13}$$

also referred to as the coherence length. $\lambda_\circ$ denotes the central wavelength of the light and $\Delta \lambda$ is the bandwidth. So for a laser light source of $\lambda_\circ = 653$ nm with a $\Delta \lambda_\circ \sim 0.18$ nm, the coherence length is $\Delta l \sim 2.5$ mm. On the other hand, for a frequency stabilized Helium-Neon laser, of $\lambda_\circ = 633$ nm and $\Delta \lambda_\circ \sim 0.001$ nm, the coherence length is on the order of meters [33].

Spatial Coherence

Two light beams originating from a single source exhibit spatial coherence. Typically, the idea of spatial coherence arises in wavefront-splitting interferometers, where the wavefront is sampled in two or more different locations and overlapped for interference. Light originating from a source can only be sampled over a prescribed area over which it is spatially coherent, described by [33]

$$\Delta A \sim (\frac{\lambda_\circ^2 R^2}{S}), \tag{2.14}$$

where R is the distance from the source to the sampling plane containing two or more pupils, and S is the area of the source. Larger R and smaller S will result in larger coherence area and therefore higher spatial coherence. Laser sources have the potential of producing light of very high spatial coherence [36], specially as the laser emission wavelength approaches infra-red regions of the spectrum. The high spatial coherence of lasers manifest itself in the speckle pattern that is associated with any laser source.

Interference in Terms of Coherence

For two quasi-monochromatic light beams to interfere, they have to be spatially and temporally coherent. Consider that the light from a laser source has been divided into two beams, and through a series of optical fold-flats the beams are overlapped at the observation focal plane. The beams have to travel the distance of $\mathbf{r}_0$ and $\mathbf{r}_1$ and the time elapsed for each beam to reach the observation plane is t_0 and t_1. The resulting electric field at the observation location is

$$\mathbf{E}(\mathbf{r}, t) = E_0(\mathbf{r}_0, t - t_0) + E_1(\mathbf{r}_1, t - t_1). \tag{2.15}$$

The observable intensity of the overlapped beam is defined by Equation 2.7 and in this case yields

$$I = \epsilon \, \mu [I_0 + I_1 + 2\Re\{\Gamma(\mathbf{r}_0, \mathbf{r}_1, \tau)\}], \tag{2.16}$$

where $\tau = t_0 - t_1 = \frac{\mathbf{r}_0 - \mathbf{r}_1}{c}$, the time of flight deference. The function $\Gamma(\mathbf{r}_0, \mathbf{r}_1, \tau)$ is the mutual coherence function describing the time-averaged correlation between the two light beams (electric fields) at the observation plane, and is defined as [33]

$$\Gamma(\mathbf{r}_0, \mathbf{r}_1, \tau) = < E_0^*(\mathbf{r}_0, t) E_1(\mathbf{r}_1, t + \tau) > . \tag{2.17}$$

It is conventional to normalize the mutual coherence function to yield the complex degree of coherence

$$\gamma(\mathbf{r}_0, \mathbf{r}_1, \tau) = \frac{\Gamma(\mathbf{r}_0, \mathbf{r}_1, \tau)}{\sqrt{I_0 I_1}}, \tag{2.18}$$

and further specify it to be

$$\gamma(\mathbf{r}_0, \mathbf{r}_1, \tau) = |\gamma(\mathbf{r}_0, \mathbf{r}_1, \tau)| e^{i(\omega_\circ \tau)}. \tag{2.19}$$

Finally, the result of the overlap of two quasi-monochromatic light beam can be described using Equations 2.16 and 2.19 and is

$$I = \epsilon \, \mu [I_0 + I_1 + 2\sqrt{I_0 I_1}|\gamma(\mathbf{r}_0, \mathbf{r}_1, \tau)| cos(\omega_\circ \tau)]. \tag{2.20}$$

Equation 2.20 is the total optical intensity of the overlapping light beams at the observation plane. As before, the sinusoidal behavior which would result in an interference pattern is observed. The dependence on τ demonstrates the dependence on the difference in path that each beam has traveled, referred to as the optical path difference. The fringe visibility is described similar to Equation 2.11, using the optical intensity described in this section.

15

2.2.3 Young's Experiment

Thomas Young, in an effort to establish the wave nature of light, proposed an experiment in which the result of the superposition of two spherical, uniform, and quasi-monochromatic light waves are studied. The experiment consists of illuminating two identical slits, in-line with each other with the light emerging from a single pinhole, simulating a single coherent source. Thereafter, the wavefronts that emerge from the slits are coherent and will interfere.

According to Equation 2.10, interference arises due to the phase difference between the two superimposed light waves. There will be a phase difference if there is a difference in the distance traveled between the two waves from their source, the screen containing the two slits in this case, to the location of observation, the detector plane. This difference in path is referred to as the optical path difference (OPD) and is denoted by Λ. The relationship between the phase difference and the OPD is [19]

$$\Delta\phi = \frac{2\pi}{\lambda_\circ}\,\Lambda.$$
(2.21)

The phase difference changes by 2π every time the OPD increases by one wavelength.
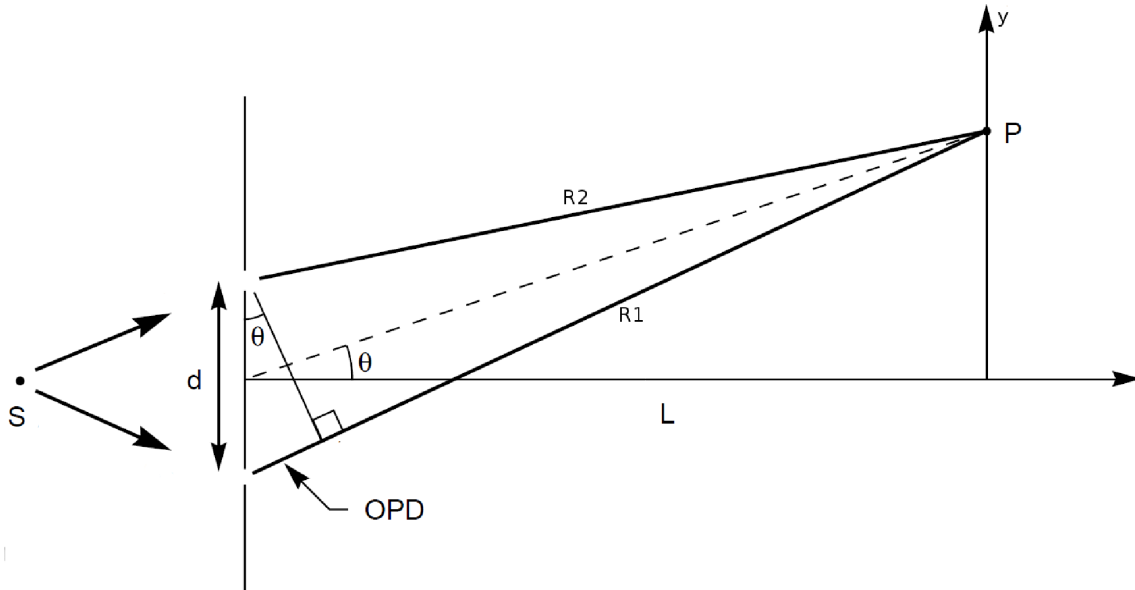
Figure 2.4: Young's double-slit experiment.

In Young's experiment, Figure 2.4, Young simulates a single coherent light source by passing light through a pinhole. The light emerging from the first pinhole (S) illuminates a screen containing two slits separated by a distance d. The light then diffracts from the slits and is observed on a viewing screen of distance L away. The interference pattern is observed at an arbitrary point P, on the detector plane.

Based on the discussion from the previous sections, the interference pattern observed on the detector will have a prescribed fringe frequency described by

$$\mathcal{F} = \frac{d}{L \, \lambda_\circ}, \tag{2.22}$$

with units of inverse meters with $\lambda_\circ$ being the central wavelength of the light. Equation 2.22 can provide information about separation of the two slits, the distance to the detector plane and the wavelength of light in the interferometer.

Chapter 3

Design of the Laser Interference Fringe Tomography Instrument

This chapter describes the instrument proposed in this document. First, an overview of the imaging modality along with a description of the instrument is presented. Then, the mathematical theory of the instrument is described which enables a better theoretical understanding of the instrument and its design. Following that is an in-depth presentation of the design constraints and where applicable trade-off studies for various design choices. Finally, the prototype is presented and the choice made for each sub-system is justified.

3.1   The Optical Design

Laser interference fringe tomography (LIFT) is in the class of diffuse optical imaging devices designed for three-dimensional microscopic imaging applications. LIFT is designed to be a very simple and cost-effective imaging device with modest performance capabilities. It measures the reflectivity as a function of depth within a sample and is capable of producing three-dimensional, tomographical images from optically scattering media. LIFT provides a low-cost solution for the various imaging applications introduced in Chapter 1 where none existed previously, see Table 1.1 and Figure 1.1.

The invention of OCT proved that the properties of a low-coherence light source and the principles of interferometry can enable optical imaging. By capitalizing on the higher spatial and temporal coherence of a quasi-monochromatic light source such as a laser, and

the interferometric properties of the electromagnetic radiation (light), LIFT is capable of probing into a sample.

LIFT is a wavefront splitting interferometer. It samples two disjoint sections of the scattered light returning from a sample and, by overlapping the two, produces an interference pattern. From the interference pattern a depth-profile can be reconstructed. LIFT is designed to be a very simple instrument using minimal critical optical elements as the laser light will have to interact with minimal optical components on its path to the detector. In general, interferometric devices have a very low tolerance for misalignment because they incorporate many optical elements that manipulate the light in its path. LIFT, on the other hand, seems to have a high tolerance for misalignment. Reducing alignment complexities will result in a more user-friendly and reliable instrument. The operation of the instrument will be much simpler and measurements can be done more quickly with higher precision and accuracy.

The optical design of the first generation of LIFT is shown in Figure 3.1. The light from the laser source is focused on the surface of the sample by a lens. The light is then scattered off of the surface or from any depth into the sample in all directions in the hemisphere toward the lens. If the sample is thin enough, some light may be able to travel through the sample. Any light returning from the sample is treated as if it is originating from a source of size R_l, which is the size of the focused spot described in Equation 2.4.

The light emanating from the sample that illuminates the focusing lens, becomes collimated as it passes through the lens. The collimated aperture of light falls onto a mask with two holes, pupils, and only the light that goes through the pupils is allowed to continue downstream. The light beams emerging from the pupils are then reflected off of two mirrors: a relay mirror which bends the path of the beam and places it on the detector and a manipulating mirror on kinematic holders for ease of adjustment of the direction of the beams. Using the manipulating mirror, the beams are overlapped at the imaging plane of the detector. As a result of the overlap, an OPD is introduced between the two beams. If the OPD is smaller than the coherence length of the laser, an interference pattern is observed on the detector. The frequency of the interference pattern signifies the depth at which the signal has originated from. The intensity of the signal represents the strength of the reflectivity at that depth.
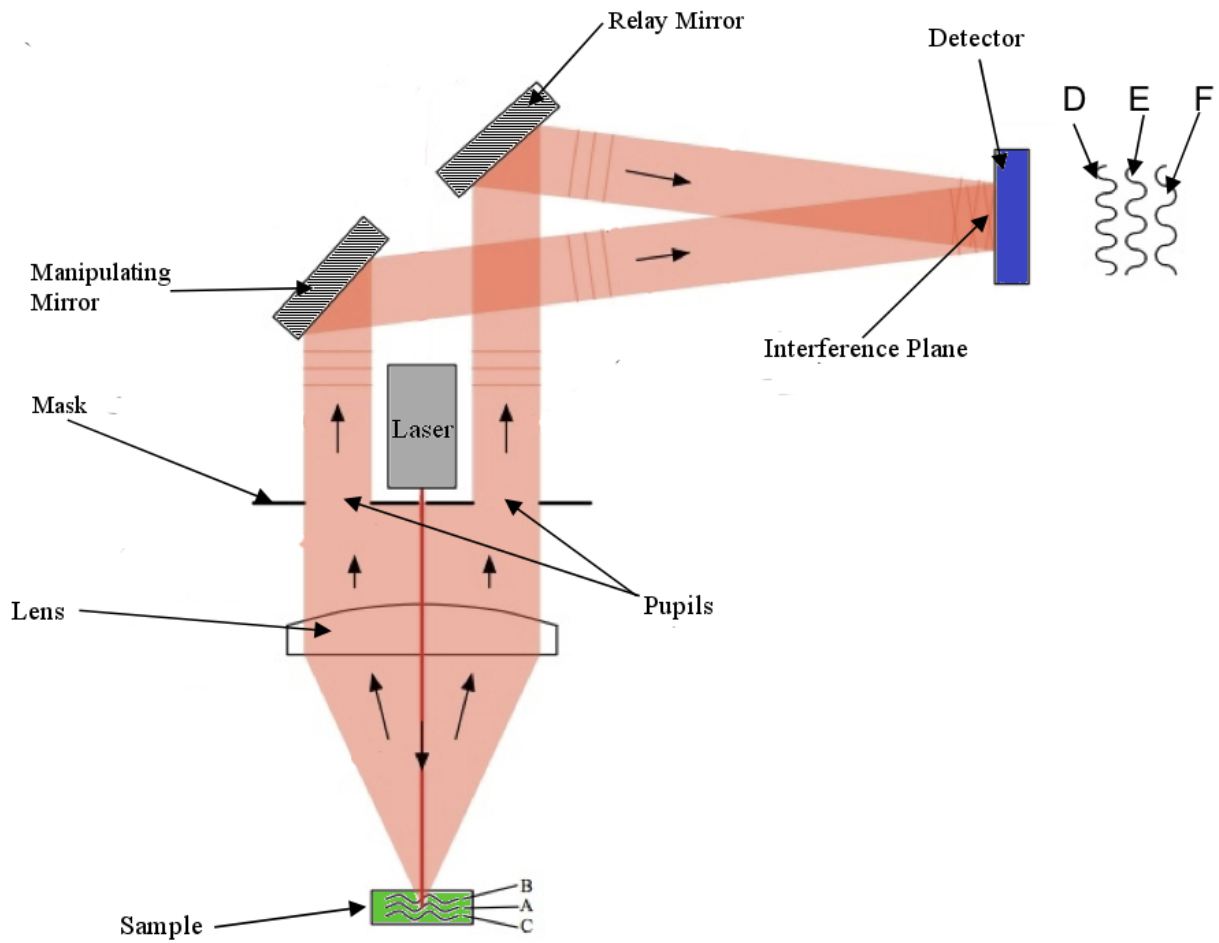
Figure 3.1: The annotated optical design of LIFT with the elements labeled. The sinusoidal interference pattern of frequencies D, E, and F correspond to the light returning from depths C, A, and B, respectively.

In general, a lens will collimate the exiting light if a light point-source is placed at the focal plane of the lens. The meaning of collimated light is that the wavefront has no curvature and is planar. If the point source is placed in front or behind the focal plane of the lens, the wavefront exiting the lens will no longer be collimated and will be under- or over-collimated and will have a convex or a concave shape, respectively. However, when the curved wavefront travels sufficiently far from the lens and is sampled over a small area it tends to appear planar [19]. For the purpose of this document, since the distance at which the light is sampled is much greater than the aperture of the lens, all wavefronts are assumed to be planar whether they are emitted from the focal plane or not. The treatment of curved wavefronts concerning the topics discussed in this document are beyond the scope of the work presented here.

In LIFT, the collimated light beams emerging from the pupils will be parallel to each other over a sufficiently long distance. The light that is originated from in front of the focal plane is under-collimated, therefore the beams out of the pupils will be diverging. Conversely, the light originated from behind the focal plane is over-collimated, therefore the beams out of the pupils will be converging. Figure 3.2 is a graphical representation of this phenomenon. A point source in LIFT refers to a location on a sample at which point the illuminating laser light is scattered from isotropically.
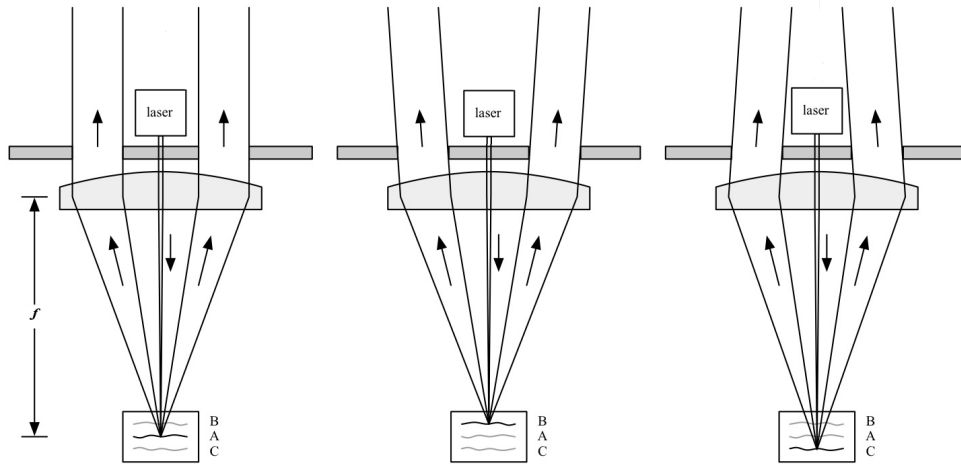
Figure 3.2: The behavior of light emerging from the pupils in the mask when the light returns from the focal plane of the lens (level A), in front of the focal plane (level B) and behind the focal plane (level C). The light is collimated, under-collimated, and over-collimated in the three cases, respectively. Image taken from [23].

21

A mirror is an example of an on-axis specular scatterer (a surface reflector). This means that it reflects almost all the light at an angle equal to the incoming beam but symmetric about the normal to the surface of the mirror. Mirrors are used as calibration targets for majority of diffuse optical imagers. However, LIFT only works if the sample is an isotropic scatterer so there is a need for a 'mirror-like' sample that produces specular scattering in order to derive the mathematical model of LIFT and for the calibration of the instrument. The sample that minimally absorbs the illuminating light and prevents any penetration is a sandblasted (roughened) metallic surface. A sandblasted aluminum block was used for this purpose and it is hereafter referred to as the 'aluminum phantom'.

3.2 The Theory

It is very important that any physical system be mathematically described and modeled. Starting from the fundamental physical properties of electromagnetic waves – light in this case – and the basis of the principles of interferometry, a mathematical model of LIFT is derived.

The LIFT instrument is designed based on the *a priori* assumption that a depth profile can be retrieved from an interference pattern. The overlap of the light beams from two pupils, sampled from the full collimated aperture of emanating light, would give rise to this interference pattern. The interference will be visible in the plane of the detector if the two beams are spatially and temporally coherent.

It is the angle at which the two beams are subtended at with respect to each other that gives rise to the interference pattern observed on the detector plane. More generally, the angle between the two beams generates an OPD (Λ). If Λ is within the coherence length of the light source, then the interference pattern is observed with good visibility.

In LIFT, before the two beams are directed off of the manipulating mirrors there is no difference in their respective paths. There is a difference in path introduced between the manipulating mirrors and the detector. It is worth mentioning that the mathematical treatment of LIFT is at this point purely geometrical and is heavily influenced by the Paraxial approximation of geometrical optics. The in-depth Fourier analysis of this device is beyond the scope of this work.
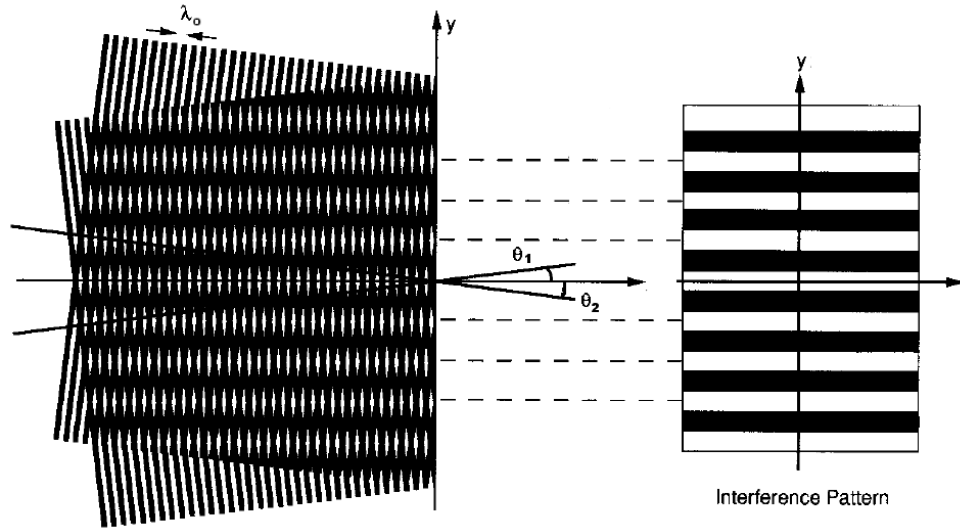
Figure 3.3: General geometry for interference for two planar electromagnetic waves onto an interference plane, along with a sketch of the interference pattern. Image taken from [19].

In a general case, one of the planar beams is relayed onto the observation plane at an angle of θ_1 and the other is relayed and overlayed onto the first beam at an angle of θ_2. The quantity of interest here is the relative angle between the two beams $\theta = \theta_2 - \theta_1$, see Figure 3.3. The interference pattern is observed as vertical lines across the observation plane. These convey constructive and destructive interference referred to respectively as bright and dark fringe.

Figure 3.3 is simplified to just one wavelength of each of the wavefronts, it is shown in Figure 3.4. Where the wavefront subtended to the normal of the observation plane at an angle of θ_1, it is shown in solid lines and the wavefronts subtended to the normal of the observation plane at an angle of θ_2, is shown in dashed lines. The total angle difference θ between the two beams is also denoted as well as the distance between two interference minima, y.

The distance between each interference maximum on the detector plane is derived geometrically and is given by

$$y = \frac{\lambda_\circ}{2 \, sin \, \frac{\theta}{2}},$$ (3.1)

in units of meters. This derived quantity is verified by [19] and [14]. Simply by inverting

Equation 3.1, the fringe frequency $\mathcal{F}$ is calculated.
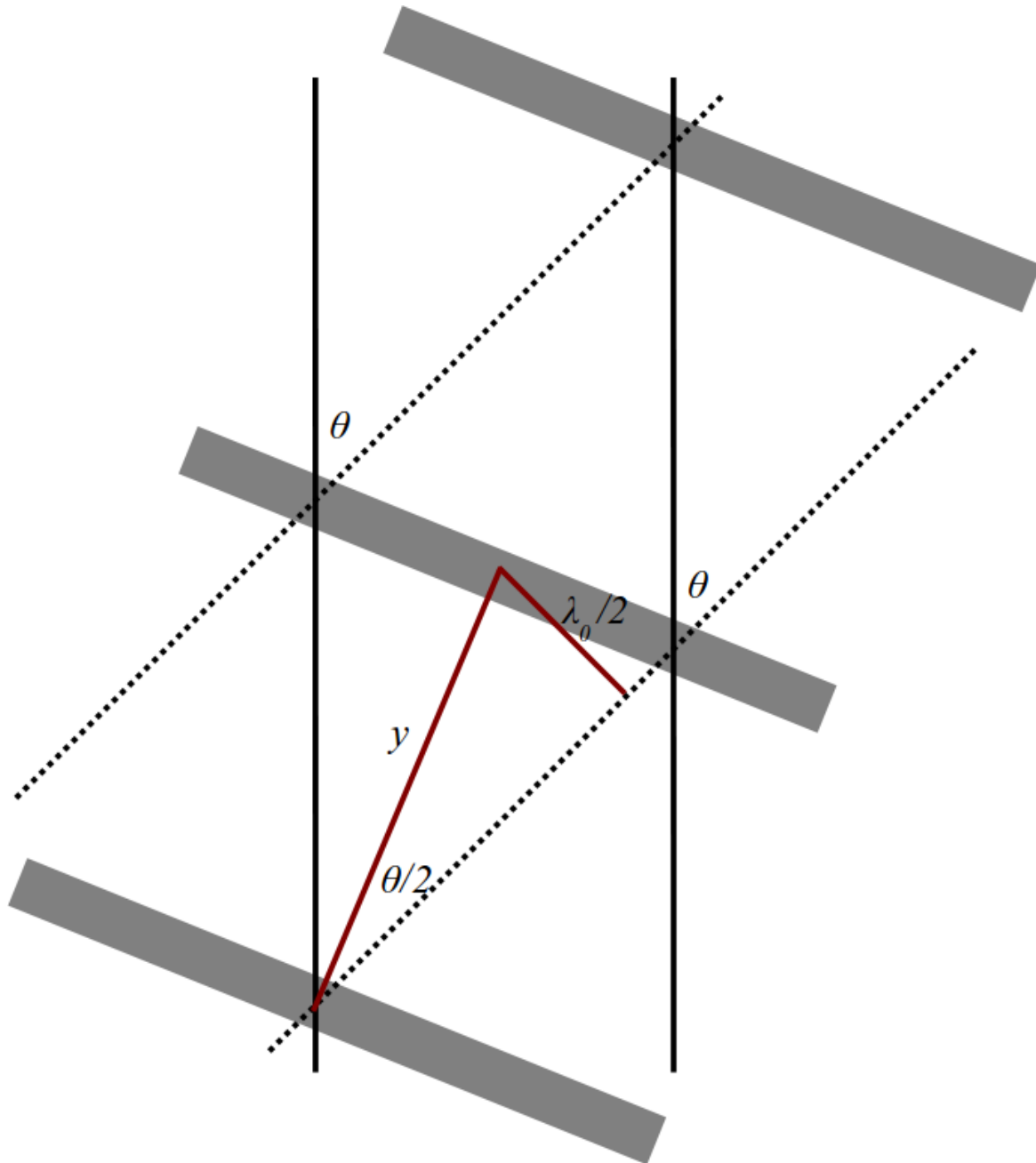
Figure 3.4: One wavelength of wavefront one (solid lines) and wavefront two (dashed lines) crossing each other at an angle of θ. The gray bars represent the interference maxima and are not drawn to scale. They are used for ease of visualization.
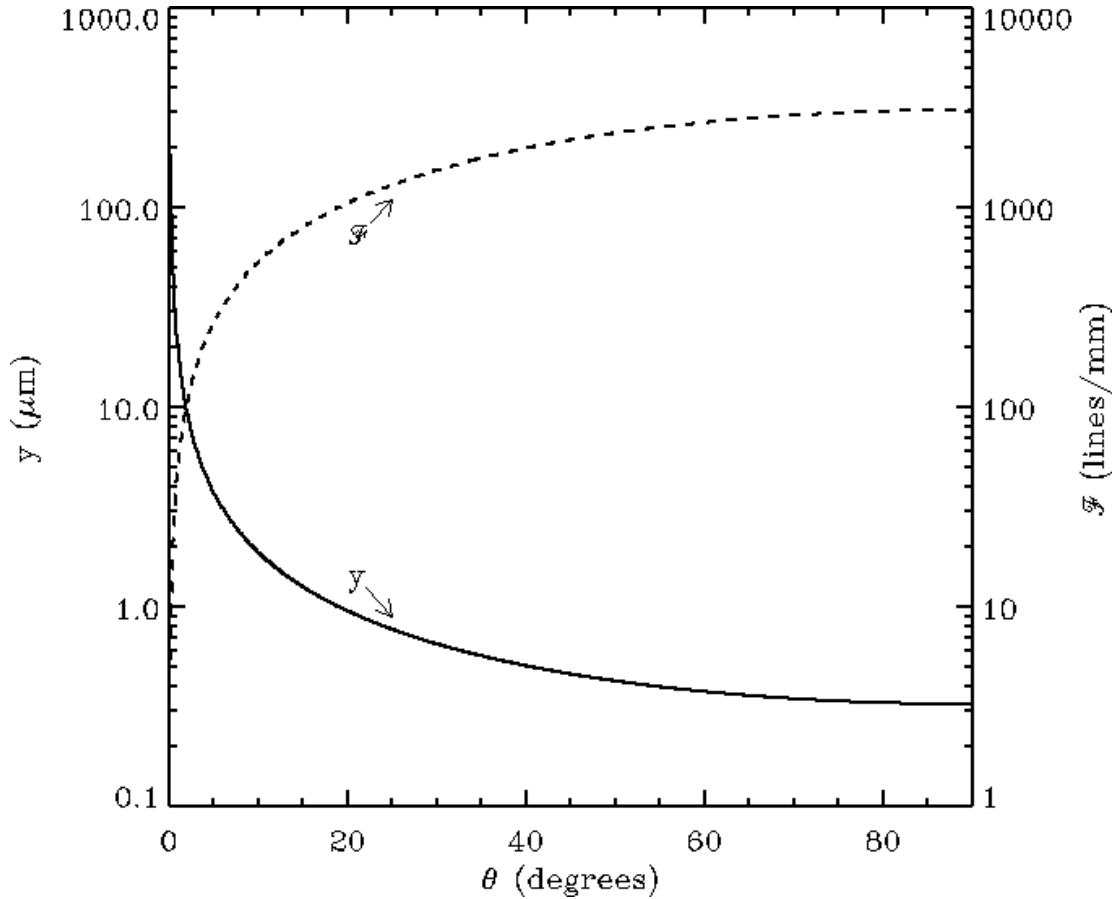
Figure 3.5: A plot of the distance between the fringes, y (solid line), and the fringe frequency, $\mathcal{F}$(dashed line), as the angle of intersection between the two plane waves changes.

Figure 3.5 shows that for a fixed wavelength of light, the distance between each consecutive fringe decreases as the angle between the two overlapped plane waves is increased. Inversely, the fringe frequency, or number of fringes in a given length, increases with an increasing angle of intersection. At $\theta = 0°$ there is no interference between the two beams and what is observed is simply the addition of the intensity contribution of each individual beam. At $\theta = 90°$ the minimum possible distance between consecutive fringes is reached as well as the maximum fringe frequency. Both curves are symmetric about $\theta = 90°$ where y approaches infinity and $\mathcal{F}$ approaches zero at $\theta = 180°$

In the LIFT instrument, if the laser light is scattered off of the surface of a sample (specular scattering) at the focal plane of the lens in the instrument, the light emerging from the two pupils is parallel and separated by the distance between the two pupils, d.

The two planar wavefronts intersect each other at the observation plane of the detector while one beam is subtended to the other at angle θ.
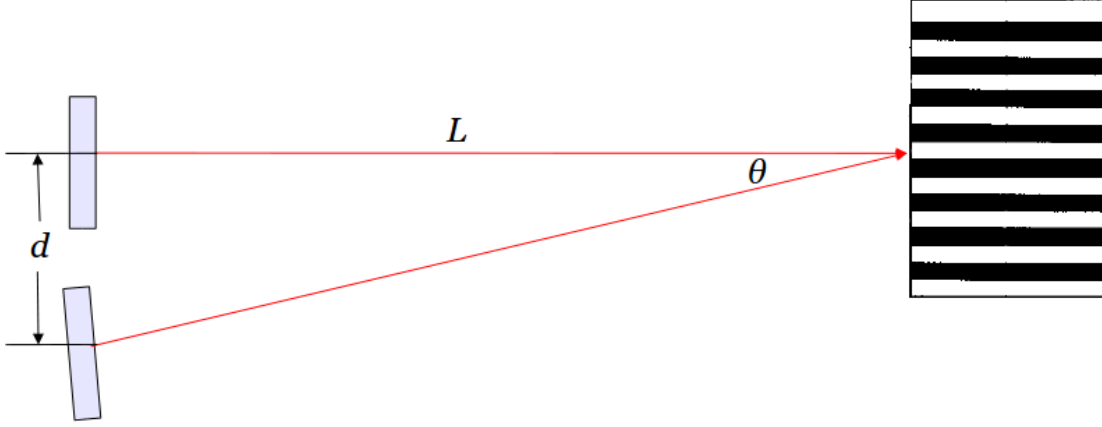
Figure 3.6: A plot of the distance between the fringes (solid line) and $\mathcal{F}$ as the angle of intersection between the two plane waves changes.

According to Figure 3.6, $tan\,\theta = \frac{d}{L}$. As per the Paraxial approximation $tan\,\theta \simeq sin\,\theta \simeq \theta$ and Equation 3.1 becomes $y = \frac{\lambda_\circ}{\theta}$. Finally, as a result of placing a point source at the focal plane of the instrument the fringe frequency of the interference pattern of LIFT is

$$\mathcal{F} = \frac{d}{\lambda_\circ\,L}, \tag{3.2}$$

where L is the distance between the relay mirror and the detector. The distance between the manipulating mirrors and the detector is slightly larger.

The fringe frequency shown in Equation 3.2 is observed on a detector chip of some width. The width of the detector is determined by the number of pixels on the chip, N_x, and the width of each pixel, δx. Using this information the number of fringes observed across a detector can be represented by

$$N_{\mathcal{F}} = \frac{N_x\,\delta x\,d}{\lambda_\circ\,L}. \tag{3.3}$$

So far mathematical model of LIFT describes imaging an aluminum phantom placed at the focal plane of the instrument. Now consider what happens when the aluminum phantom is placed in front or behind the focal plane of the lens. In front of and behind the focal plane means the surface of the aluminum phantom is closer and farther away from the lens, respectively.

26
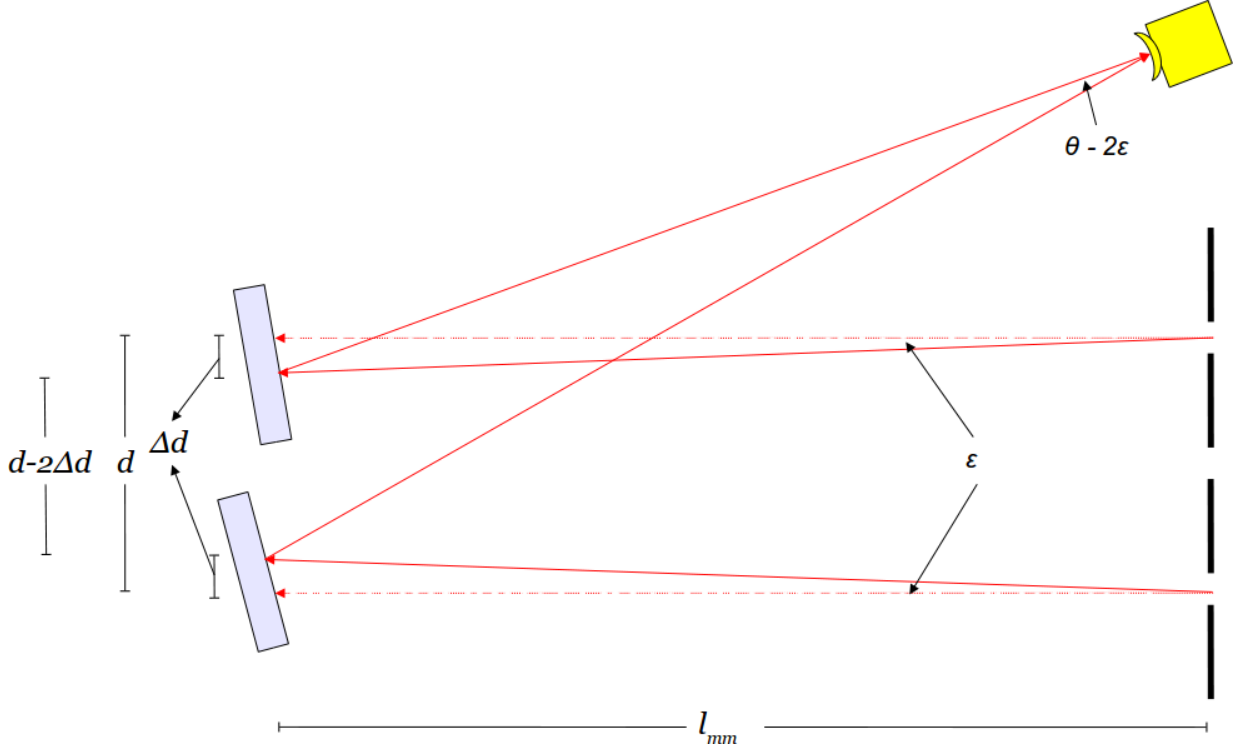
Figure 3.7: A schematic of converging beams emerging from the pupils (solid lines) subtended at an angle of ϵ to the collimated beams (dashed line). Along with the resulting angle at the location of overlap of the two beams.

Considering the case in which the surface of the aluminum phantom is behind the focal plane at a distance of $f + x$, as shown in Figure 3.2, the lens will over-collimate the light and the emerging beams will tend to converge as they travel from the mask toward the two mirrors. In Figure 3.7 the angle at which the two beams intersect each other at the observation plane is $\theta - 2\epsilon$ and the distance between neighboring fringes is approximated form of Equation 3.1 to be

$$y = \frac{\lambda_\circ}{\theta - 2\epsilon}, \tag{3.4}$$

with $\theta - 2\epsilon = \frac{d - 2\Delta d}{L}$ and $\Delta d = l_{mm}\ tan(\epsilon)$, where l_{mm} is the distance between the mask and the mirrors. It is clear that the distance between each mirror and the mask is not l_{mm} exactly, this issue is addressed in § 3.3.1. By symmetry, if the aluminum phantom is placed in front of the focal plane at $f - x$, the beams out of the pupils will be diverging at an angle of ϵ which results in an angle of $\theta + 2\epsilon$ at the observation plane. Therefore, depending on

where the sample is with respect to the focal plane, the resulting fringe frequency is

$$\mathcal{F} = \frac{d \pm 2l_{mm} \ tan(\epsilon)}{\lambda_\circ \ L}. \tag{3.5}$$

The value of ϵ is dependent on the offset $\pm x$ from the focal plane and it can be determined geometrically by considering the following.
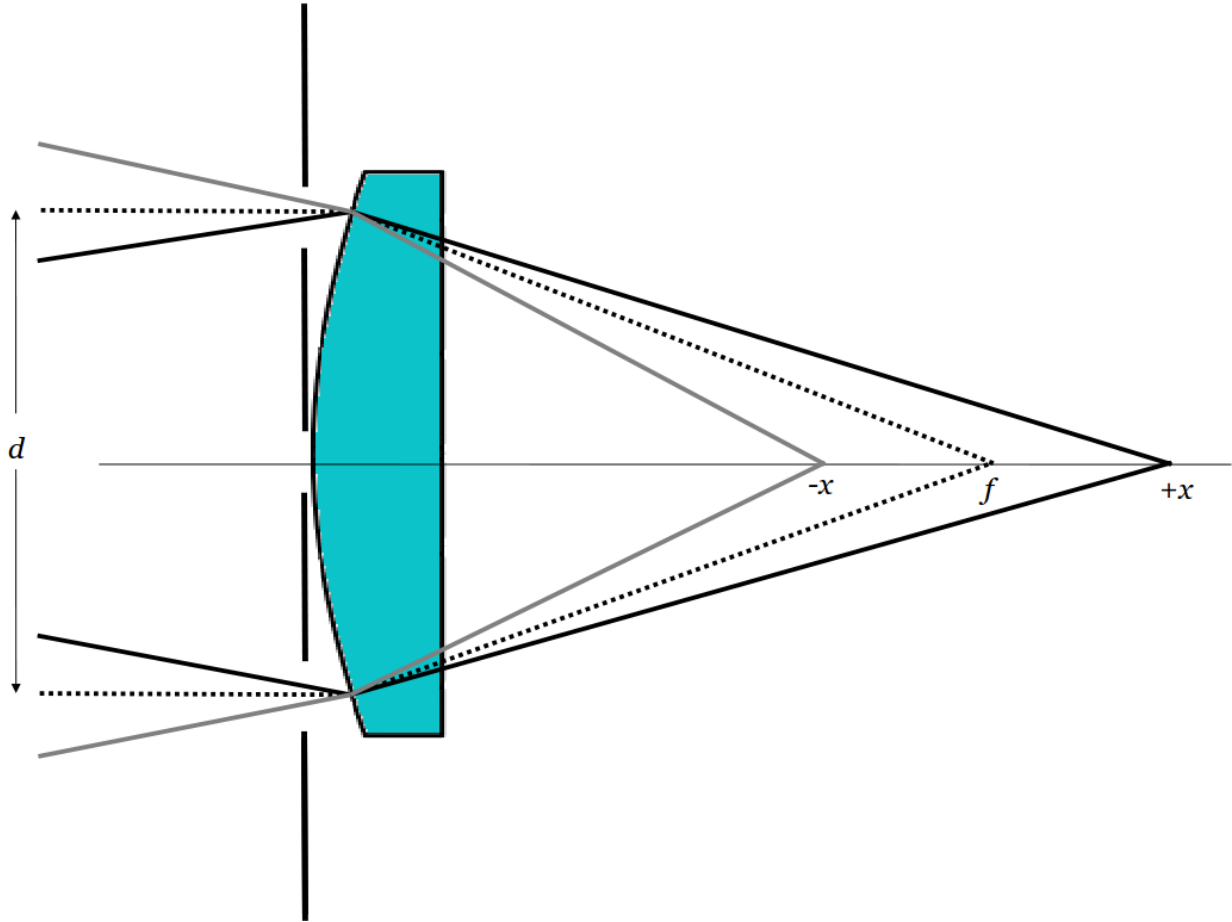
Figure 3.8: Light propagation, originating from a sample placed at f - x (gray), f (dashed), and $f + x$ (black) on the optical axis, as it travels through the lens and emerges from the pupils.

Figure 3.8 shows the light path originating on, in front of, and behind the optical axis of the instrument from the focal plane. The light interacts with the lens symmetric about the optical axis and then carries through the pupils. It is safe to assume that the only

light that is allowed to pass through the pupils is the light that interacts with the lens at distance of $\frac{d}{2}$ about the optical axis.
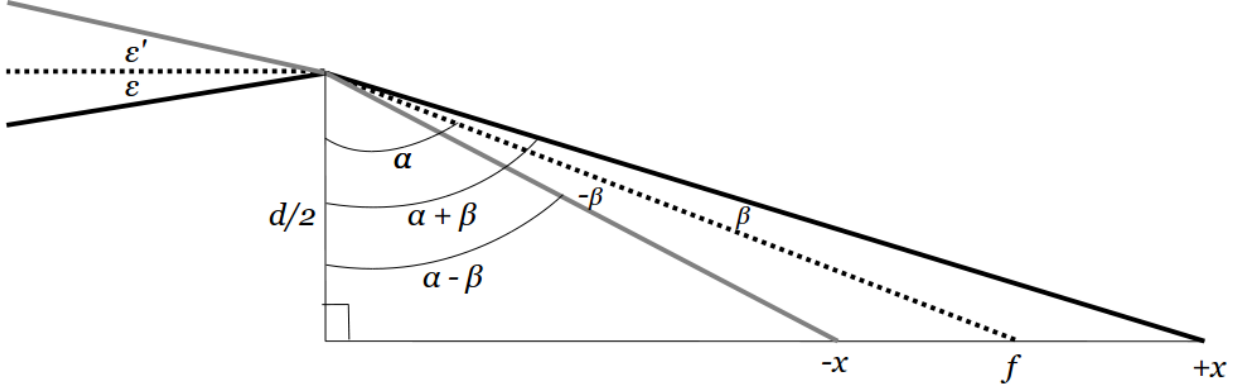
Figure 3.9: Light propagation, originating from a sample placed at $f - x$ (gray), f (dashed), and $f + x$ (black) on the optical axis, emerging from the pupils. Along with the similar triangles formed.

The dependence of the angle at which the light beams emerge from the pupils on the amount of offset from the focal plane will be determined using the method of similar triangles. A crucial assumption in this derivation is that $|\epsilon| = |\epsilon'| = |\beta|$. Also that $\beta = -\epsilon$ and $-\beta = \epsilon'$ which can be attributed to the interaction between light and lens. The angle $|\epsilon|$ on the image side of the lens is the negative of its corresponding angle $|\beta|$ on the object side of the lens.

So, from Figure 3.9 the following relationships are observed

$$tan(\alpha) = \frac{2f}{d}, \tag{3.6}$$

and

$$tan(\alpha \pm \beta) = \frac{2f \pm 2x}{d}. \tag{3.7}$$

By rearranging Equations 3.6 and 3.7, ϵ can be written as

$$\epsilon = tan^{-1}(\frac{2f \pm 2x}{d}) - tan^{-1}(\frac{2f}{d}). \tag{3.8}$$

Now the expression for the fringe frequency at the observation plane (Equation 3.8) can be written as

$$\mathcal{F} = \frac{d + 2l_{mm}\ tan[tan^{-1}(\frac{2f+2x}{d}) - tan^{-1}(\frac{2f}{d})])}{L\ \lambda_\circ}, \tag{3.9}$$

29

where the applied convention is that if the sample is in front of the focal plane it has been displaced by -x and vice versa.

Equation 3.9 can be further simplified using the trigonometric identity [6]

$$tan(a \pm b) = \frac{tan\ a \pm tan\ b}{1 \mp tan(a)\ tan(b)}, \tag{3.10}$$

to be

$$\mathcal{F} = \frac{d}{L\ \lambda_\circ} + [(\frac{2d\ l_{mm}}{L\ \lambda_\circ})\ (\frac{2x}{d^2 + 4f^2 + 4fx})]. \tag{3.11}$$

Since x is on the order of tens of microns, then $4fx \ll (d^2 + 4f^2)$ and it can be ignored. Therefore, the fringe frequency equation takes its final form in

$$\mathcal{F} = \frac{d}{L\ \lambda_\circ}[1 + \frac{4x\ l_{mm}}{d^2 + 4f^2}], \tag{3.12}$$

and the number of fringes across the detector can be described by

$$N_{\mathcal{F}} = \frac{N_x\ \delta x\ d}{L\ \lambda_\circ}[1 + \frac{4x\ l_{mm}}{d^2 + 4f^2}]. \tag{3.13}$$

Equations 3.12 and 3.13 show the dependence of the fringe frequency and the number of observed fringes on the amount of departure from the focal plane, x. Both of these equation are dependent on several other variables which will be determined in the following sections.

Figure 3.10 shows the graphical representation of the fringe frequency and the number of fringes as x is varied. Note that the other variables in the above two equations were assigned arbitrary values for the purposes of examining the behavior of the above mentioned. If the aluminum phantom is placed in front or behind the focal plane, the fringe frequency is lower or higher, respectively, than when the sample is at the focal plane. Alternatively, if the surface of a sample is placed at the focal plane of LIFT, higher fringe frequencies would signify that there is light returning from scattering locations inside the sample. So the depth of the sample is probed and a 'depth profile' can be produced.

Clearly, both curves in Figure 3.10 can be extrapolated to any value of x. However, there are other physical limitations that bound the curves such as the size of the relay and manipulating mirrors, the size of the detector, the length of overlap, the distance between the mask and mirrors, and the focal length of the lens. These will all be discussed in the following sections.

30
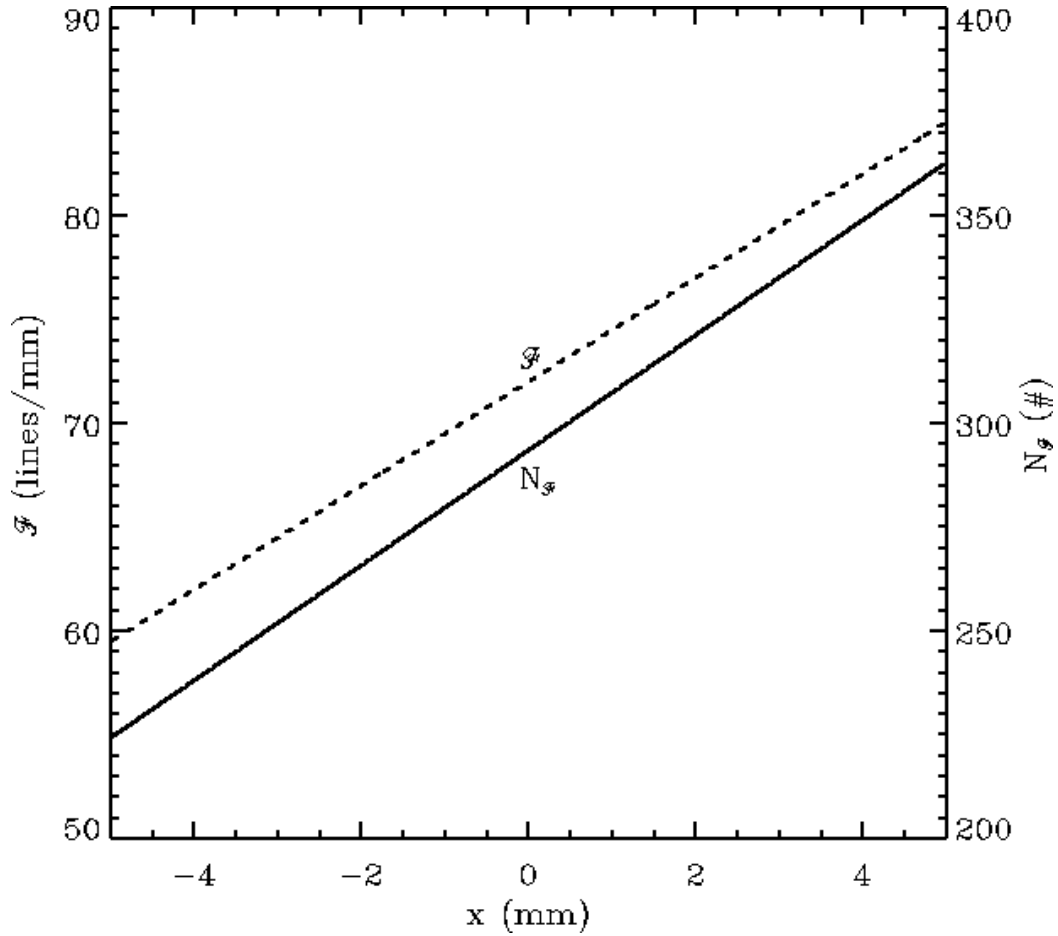
Figure 3.10: Plot of $\mathcal{F}$ and $N_{\mathcal{F}}$ as x is varied from -5 to +5 millimeters.

3.3   Design Considerations

In designing an instrument, a cost-benefit analysis needs to be carried out concerning many issues such as: cost, size, power consumption, weight, ease of use, complexity, reliability, etc. In this section, a discussion on some of the design choices for LIFT will be held and justifications will be presented. LIFT is proposed as a simpler, more accessible, land less expensive three-dimensional interferometric microscopic imager. Some of the conventional design aspects and their alternatives are presented here.

3.3.1   Mirror Placement - l_{mm} Discrepancy

The fringe frequency equation and number of fringes equation (3.12 and 3.13) were derived assuming that the reflecting surface of both mirrors (relay and manipulating) is situated at the same exact distance from the mask where l_{mm} is the same for both mirrors. In reality however, this is a difficult task to achieve especially if LIFT is not assembled in a carefully constructed housing. Usually a CNC machined structure to house precision optical equipment will have a distance tolerance of 100 - 500 μm and the quantity l_{mm} can be carefully controlled.

Since the LIFT prototype will be assembled on an optical breadboard, l_{mm} for each of the mirrors can not be controlled to better than $\sim$ a millimeter. The purpose here is to find out how much the reflecting surface of one mirror can differ from the other before any noticeable discrepancy in the data is observed. The assumption made here is that one of the mirrors is situated at l_{mm} from the mask and the other is at a distance of $l_{mm} \pm \xi$. It is worth mentioning that the path difference of ξ will introduce a phase difference of $\Delta\phi = \frac{2\pi}{\lambda_\circ} \xi$ between the two beams.

Assuming that the aluminum phantom is placed at the focal plane of the lens so the beams out of the pupils run parallel; Figure 3.11 suggests that the displacement can only be in a direction parallel to the optical axis and can never be in the other two spatial directions. If the light was returning from the sample in front or behind the focal plane, then the displacement can be in directions parallel and perpendicular to the optical axis.

In the specific case of the parallel pupil beams and a separation between the reflecting surface of the mirrors, the distance between the two reflecting spots on the mirrors is not simply d, but it is $\sqrt{d^2 + \xi^2}$, assuming $\xi \ll d$. The quantity ξ is typically on the order of one or a fraction of a millimeter, so it is very small in comparison to all other lengths in LIFT. Therefore, the fringe frequency equation, Equation 3.2, is now

$$\mathcal{F} = \frac{\sqrt{d^2 + \xi^2}}{\lambda_\circ\, L}, \tag{3.14}$$

assuming $\sqrt{d^2 + \xi^2} \ll L$ and can further be simplified to be

$$\mathcal{F} = \frac{d}{\lambda_\circ\, L}\, \sqrt{1 + \frac{\xi^2}{d^2}}. \tag{3.15}$$
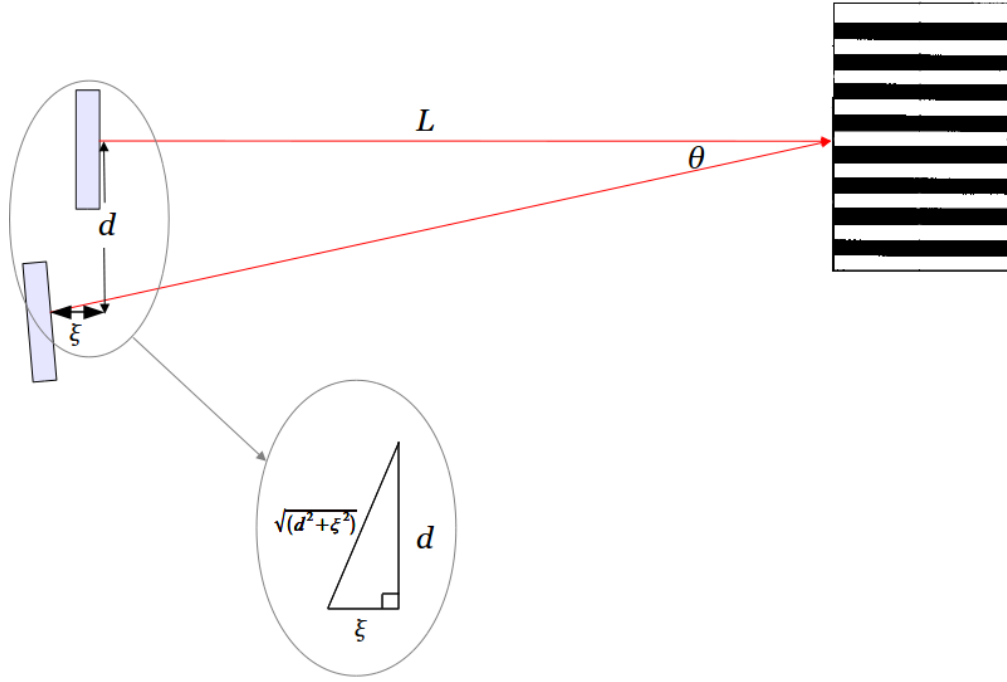
Figure 3.11: Pupil beams being reflected off of the relay and manipulating mirrors while the manipulating mirror is displaced along the optical axis by ξ with respect to the relay mirror.

Observing that $\frac{\xi^2}{d^2} \ll 1$, then let $p = \frac{\xi^2}{d^2}$. By performing a Taylor series expansion of form [6]

$$(1+p)^q = 1 + qp + q(q-1)\frac{p^2}{2!} + \mathcal{O}(p^3) + ... ,\tag{3.16}$$

about 1, the number of fringes observed on the detector can be described to second order by

$$N_\mathcal{F} = \frac{N_x\ \delta x\ d}{\lambda_\circ\ L}\ (1 + \frac{1}{2}\frac{\xi^2}{d^2}).\tag{3.17}$$

Through a simulation the effect that ξ will have on the number of fringes observed on the detector is examined. According to Equation 3.17, first the prescribed number of fringes that are observed on the detector when $\xi = 0$ is calculated. Then the value of ξ is systematically increased and the number of fringes on the detector is calculated. The difference in the two quantities of fringes, $\Delta N_\mathcal{F}$, is plotted as a function of ξ in Figure 3.12.

At $\xi = 3$ mm a difference of one fringe is observed on the detector. The difference of one fringe can be misinterpreted as signal returning from some depth in the sample where
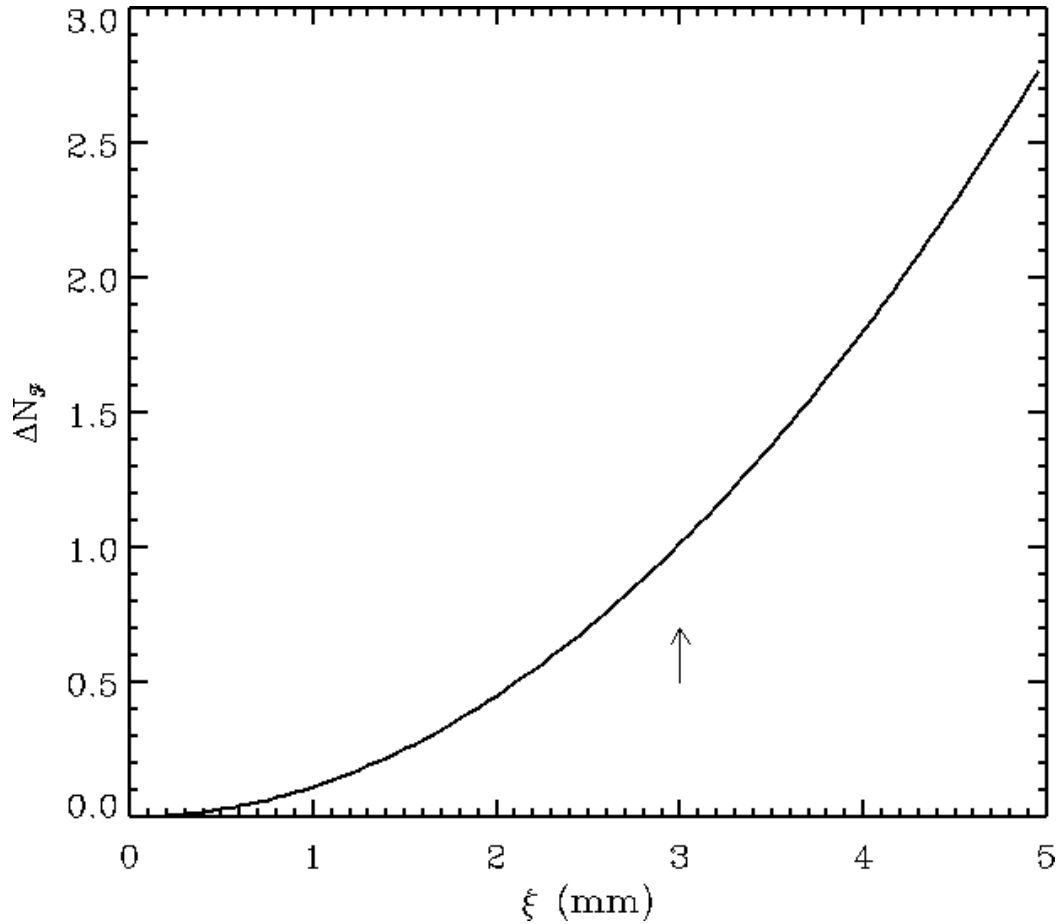
Figure 3.12: Additional fringes observed as the result of the difference in distance between the mask and the mirrors.

in reality only the surface is being probed. An alternate way of interpreting this result is that the two reflecting surfaces of the relay and manipulating mirrors can be misaligned by up to 3 mm before any significant change in the fringe frequency is observed.

3.3.2 The Focusing/Collimating Lens

There is only one lens used in LIFT and it is the most critical and important optical element used in the system. This lens is used with a monochromatic light source so it is sufficient to use a laser plano-convex singlet lens with a broadband optical coating. These lenses are very inexpensive and are readily available off-the-shelf.

It is ideal to minimize the f-number of the lens in the LIFT instrument. The f-number is the ratio of the focal length of the lens to its complete aperture or its diameter $f/\# = \frac{f}{D}$. A small f-number lens, $f/\# < 2$, is referred to as a 'fast' lens and large-number lens is a 'slow' lens. LIFT requires a 'fast' lens for the following reasons:

- The focused spot size of the laser has to be as small as possible in order to increase the lateral resolution of the instrument. The lateral resolution shown in Equation 2.4 is the diffraction limited spot size of the focused beam. In reality the focused spot size is larger than the diffraction limited value derived by the lateral resolution equation. The theoretical lateral resolution of LIFT will be determined in § 3.5.1. A 'fast' lens will enable higher lateral resolution.

- In LIFT the working principle for differentiating signal returning from various depths is that it depends on quantifying an angular tilt, in the pupil beams, with respect to the beams that are parallel. It is in this way that LIFT is able to distinguish between signal that has originated from different depths or an off-set from the focal plane in a sample.

- A 'fast' lens will also act to decrease the depth of field of LIFT. The depth of field is required to be as small as possible in order for a smaller angular tilt in the pupil beams to be more easily observed. Based on this, a 'fast' lens is one that has a smaller f-ratio. Lenses have a *clear aperture* which is 90 % of the total aperture of the lens. Within this aperture the lens is said to be functioning without any optical aberration and/or vignetting [20].

Simulation and experimental results have show that angular distribution of backscatter light after interacting with a sample is anisotropic in a 2π steradian above its surface [21]. The light backscatter distribution tends to be Gaussian about the optical axis with the $\frac{1}{e^2}$ (13% of the peak) waist at $\sim 13°$ [21, 39]. Therefore, the majority of the backscattered light is contained in a cone with an apex angle of $\sim 26°$. Considering one half of the clear aperture of a lens subtends $\sim 13°$, the ratio of the full aperture to the focal length of the lens is two. This means that an f/2 lens will be sufficient for the purposes of this instrument.

The final aspect considered in the selection of the lens is its diameter. The clear

aperture of the lens has to be large enough to allow for two pupils about the optical axis. The beams emerging from the pupils have to be separated enough to allow for two mirrors (relay and manipulating) and their mounting hardware to fit in the beam path. The mirrors themselves have to be sufficiently large to accept the converging beams for as large of an angle as possible, limited by the mounting hardware of the two mirrors.

3.3.3 The Light Source

The principle of operation of LIFT requires a quasi-monochromatic light source for the instrument. There are several solutions that would produce a very narrow band emission. The most obvious choice is a laser source. Laser light sources have very narrow bandwidth and are available in various emission wavelengths and powers. Alternatively, various spectrometer wavelength calibration light sources (e.g., Mercury, Argon, Neon, etc. lamps) can be used with a complementing narrow bandpass filter. This will allow only one particular emission line to be used as the light source in LIFT.

Using a calibration light source along with a bandpass filter increases the system's complexity as more mounting hardware and light delivery equipment (mirror fold flats, lenses, etc.) will need to be used. Additionally, these light sources are available at fixed and low output powers. At a cost of roughly $1000, it is a relatively expensive option. Many laser options are available and vary from a frequency-stabilized Helium-Neon laser at $\sim$ \$4000, to simple diode lasers $\sim$ \$10.

The wavelength of the light source is dependent on the desired application of LIFT. For optical microscopy of biological tissue, extreme red wavelengths of the electromagnetic spectrum (600 - 700 nm) can be used. For inspection of Silicon wafers the wavelength of the light source has to be in the infrared since Silicon is translucent at these wavelengths.

The power of the light source, the number of photons per unit time it generates, is an application-specific option. It is however, important for the LIFT prototype that the light source be powerful enough so the pupil beams can be seen with unaided eyes for proper alignment of the system. Constraints can be put on the output power considering Beer's law,

$$P_S = P_L \ exp(-2 \ \mu_t \ x), \tag{3.18}$$

which describes the attenuation of the light intensity as it travels through a turbid medium

[38]. In Equation 3.18 P_S is the optical power of the light returning from a depth of x from the sample, P_L is the optical power of the light source, and μ_t is the sum of the absorption and scattering coefficients of the sample (for example, 0.5 mm^{-1} for human tissue). The distance traveled by the light beam is twice the depth from where the light is returning from. The focused light penetrates into the sample and after encountering a scattering event at a given depth, it emerges from the sample.

The energy of a photon is $\frac{h\,c}{\lambda_\circ}$, where h is Planck's constant and c is the speed of light in a vacuum. The number of photons returning from any depth into the sample can be stated as

$$\widehat{\mathcal{N}_{e^-}} = \frac{P_L\ \lambda_\circ\ t\ exp(-2\ \mu_t\ x)}{h\ c}. \tag{3.19}$$

A simple simulation was carried out that shows that there is a fundamental limit to the imaging depth of any sample chiefly as a result of attenuation of photons. This simulation was done using optical characteristics of human tissue at a one second integration time and with $\lambda_\circ = 653$ nm. Figure 3.13 shows the result of this study. There is on the order of one photon returning from a depth of ~ 30 mm. Note that this threshold depth will change if the wavelength of the light source changes or the integration time is changed, though not by much. The higher-powered light source, 5 mW in this case, did show the deepest penetration but depending on the application there is a limit to the power of the light source. There is the risk of destroying the sample if the photon flux is too high. In all cases shown in Figure 3.13, 50% of the light is diminished at a 1 mm depth.

As shown previously, $\sim 87\%$ will return within a cone, about the optical axis, with an apex angle of 26°. Assuming that the cone of light is uniformly illuminating the clear aperture of the lens, the photon density of the collimated light out of the lens is

$$\widehat{\mathcal{N}_{e^-,\,l}} = \frac{0.87}{0.9\ \pi\ R_l^2}\ \frac{P_L\ \lambda_\circ\ t\ exp(-2\ \mu_t\ x)}{h\ c}. \tag{3.20}$$

where R$_l$ is the radius of the lens.

The photon density in the collimated beam is then incident on the mask which contains two pupils of radius R$_p$. The photons out of each pupil are then relayed onto a detector. The number of photons that illuminate the detector in each beam at a given R_p as the function of depth x is

$$\mathcal{N}_{e^-,\,p} = 0.97(\frac{R_p}{R_l})^2\ \frac{P_L\ \lambda_\circ\ t\ exp(-2\ \mu_t\ x)}{h\ c}. \tag{3.21}$$

37
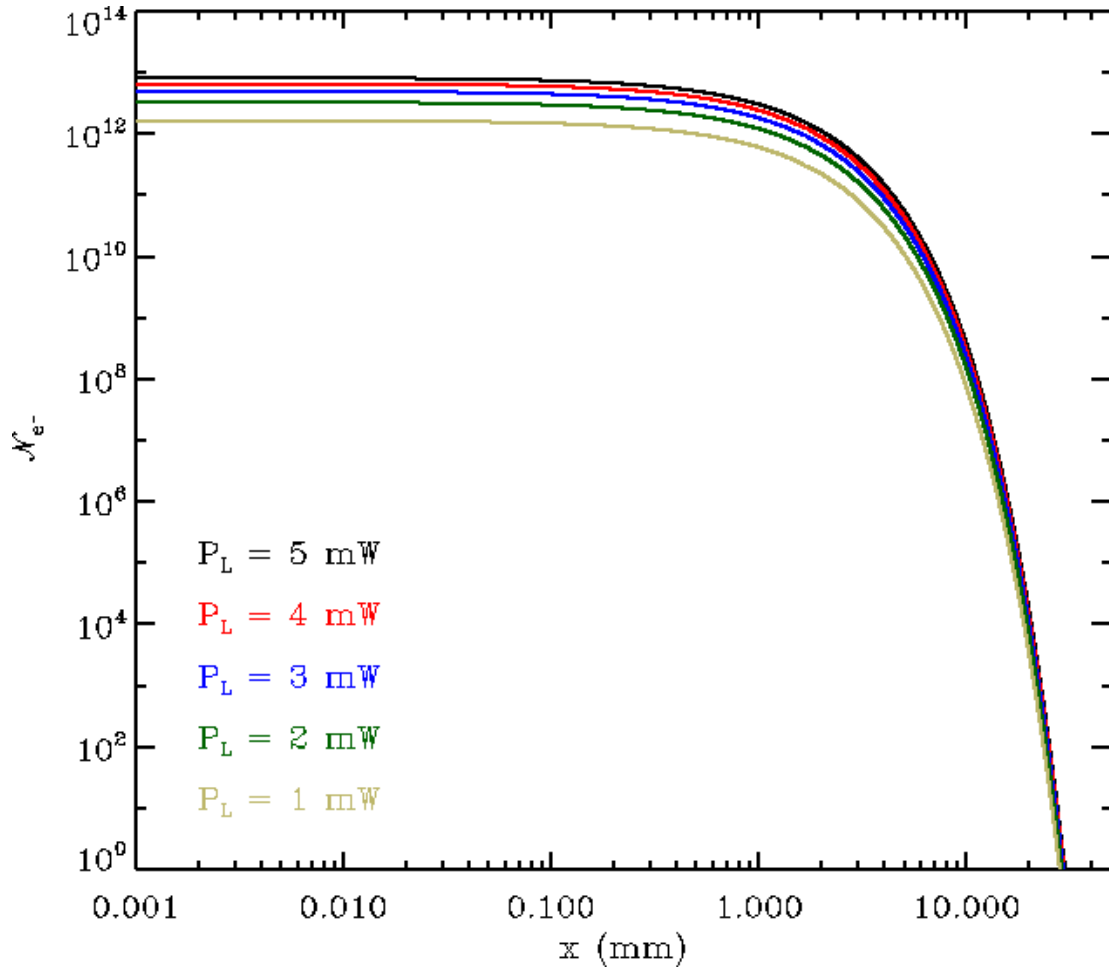
Figure 3.13: The number of photons emerging from a sample originating from various depths. The color of the curves signifies the different light source power.

The interferogram can be seen on a one-dimensional horizontal array detector as a series of bright and dark pixels. The number of bright pixels is always equal to the number of dark pixels which means that regardless of the fringe frequency, one half of the pixels on the detector are illuminated. In a two-dimensional array detector, the horizontal interferogram is repeated as many times as the vertical amount of pixels on the detector. Therefore, the number of pixels that will be collecting photons in the interferogram is $\frac{N_x}{2} \times N_y$.

The conversion factor, gain (g), determines how many photons collected by each pixel will be converted to a digital signal. The digital signal per pixel also depends on the

visibility of the interference pattern and can therefore be represented as

$$S = \mathcal{V} \ g \ t \ 2\mathcal{N}_{e^-, \ p},\tag{3.22}$$

where t is the integration time of the observation.

To explore the photon contribution of each pupil with respect to the size of the pupil and in order to optimize the size of the pupils a simulation was carried out. In this simulation the ideal conditions were considered in which the visibility of the interference is one (the entire dynamic range of the detector is being utilized, $I_{max} = 255$ and $I_{min} = 0$) and all the photons from the pupils are incident on the detector chip.
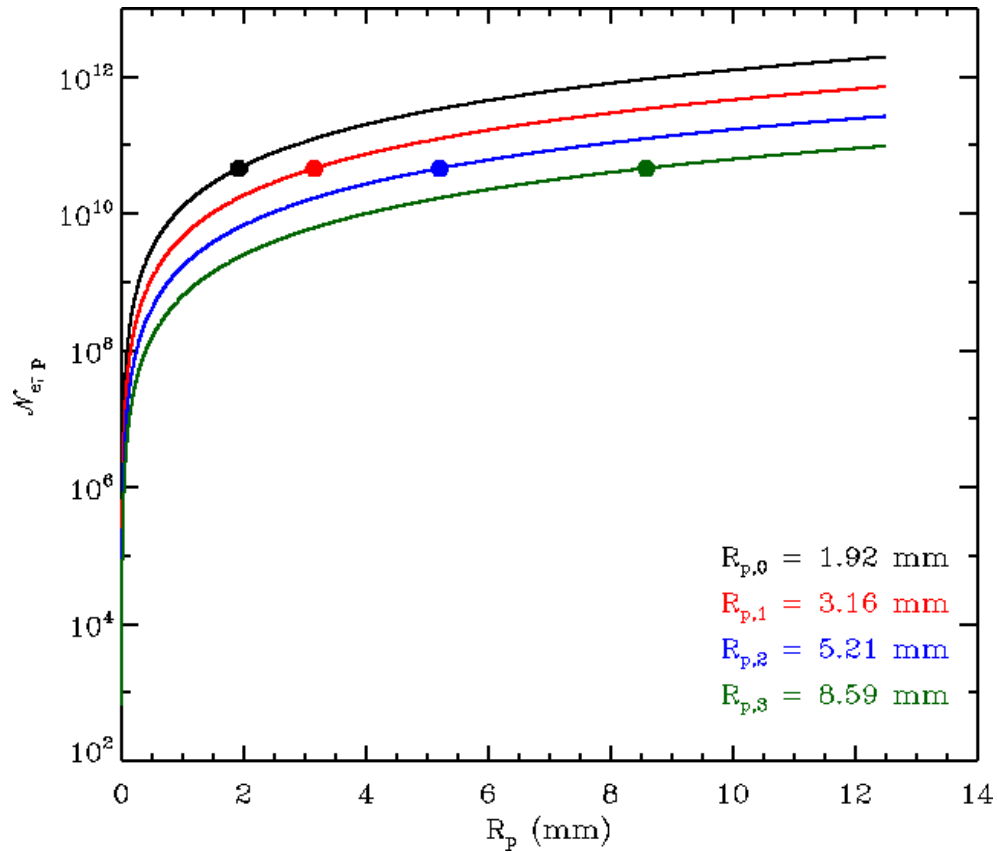
Figure 3.14: The number of photons emerging from each pupil as the radius of the pupil is varied as the light is being scattered from various depths ($x = 0$ mm (black), $x = 1$ mm (red), $x = 2$ mm (blue), $x = 3$ mm (green)) into the sample. The bullets signify the number of photons necessary for the ideal interference pattern to be observed on the detector and its corresponding pupil radius.

Figure 3.14 shows the result of this simulation which confirms the number of photons contained in the pupils of difference sizes while the light is returning from four different depths. The radius of the pupil can have a maximum value of 12.5 mm since the radius of the clear aperture of the lens is 22.5 mm. The optical properties of the simulated sample are akin to human tissue. The integration time was set to 0.5 ms, an 8-bit detector of gain equal to 1 photon per digital count was used, and all other variables were set as per previous simulations.

It is clear that if deeper structure into a sample is to be imaged, more photons are necessary. This can be achieved in one of two ways: the size of the pupils can be increased or the integration time can be increased. It becomes a balancing act between these two parameters in order to observe an interference pattern with high visibility. Nonetheless, the trade-off between these two parameters is clear in that if the pupils size has to be small because of size constraints, the integration times of the observation can be altered to achieve an interference pattern with good visibility.

Stability of the Light Source

The molecular emission line sources and frequency-stabilized lasers offer not only a very narrow band light source but their emission is at a constant wavelength and are impervious to thermal fluctuations of the surrounding medium. Diode lasers are prone to thermal fluctuations which result in the instability of the emission wavelength. There are thermally stabilized diode laser sources available but their cost is upwards of a few hundred dollars.

By simulating the effects of thermally unstable light sources on the number of fringes observed in LIFT, some constraints can be placed on the amount of the instability. Considering Equation 3.3 which described the number of fringes observed at a particular wavelength, a simulation can be done to investigate the necessary amount of departure from a stable wavelength $(\lambda_\circ \pm \Delta\lambda)$ that would result in a measurable difference in the number of fringes observed.

As shown in Figure 3.15, the wavelength of the light source has to differ from its central wavelength by more than 2 nm before a detectable change in the number of fringes can be observed. So, if the thermal instability of an unstabilized diode laser source is less than this limit, the performance capabilities of LIFT will not be compromised.
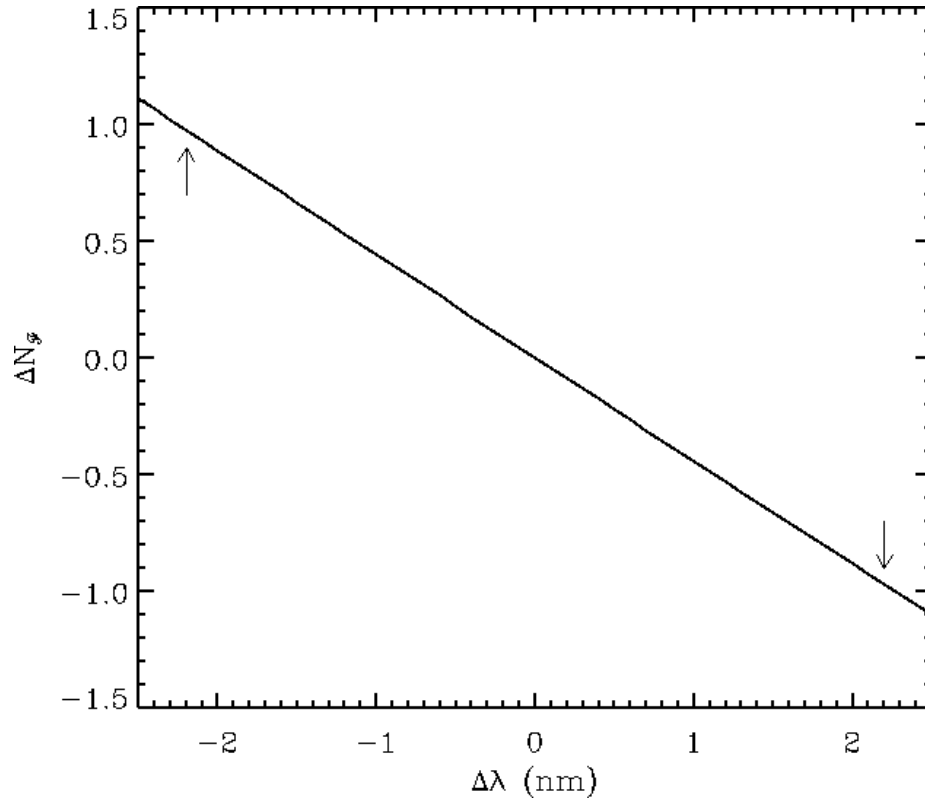
Figure 3.15: The deviation in the number of fringes observed from the norm as the result of the thermal instability of the diode laser which results in a variance of the wavelength of light emitted. The arrows show where the observed number of fringes has changed by one fringe.

3.3.4 The Detector

The most important aspect of instruments like LIFT are the capabilities of their imaging device. In almost all cases, the camera places limitations on the majority of other design aspects of the instrument as well as the overall performance capabilities. The detector is possibly the single most important element in LIFT and one of the most costly aspects of the instrument. The observable in the LIFT imaging technique is a fringe pattern of varying frequencies. Having the ability to observe a wide range of frequencies is essential for this instrument.

The interference pattern is produced on the detector chip. A given pixel on the detector would either belong to a dark or a bright fringe. The lowest fringe frequency possible

41

occurs when one fringe (bright-dark) is observed across the entire detector. Conversely, the highest detectable fringe frequency occurs when one fringe (bright-dark) is observed across two pixels.

The number of pixels on the detector, N_x, and the size of each pixel, δx, play an important role in the size and axial resolution of LIFT. If the size of the pixels is smaller, a higher fringe frequency can be observed on the detector. The overall size of LIFT can be reduced if a higher spatial frequency of the interference pattern can be measured by the detector.

The choice of detector chips is limited to CCD (charged coupled devices) or CMOS (Complementary metal-oxide-semiconductor) detectors. The detector has to be highly responsive in and around the wavelength region of the light source used in LIFT, and both solutions can cater to that. A CMOS detector offers the possibility of higher performance as well as being highly integrable and inexpensive for various applications [31]. Also, CMOS detectors offer a very high spatial resolution [30, 31]. Spatial resolution simply refers to the size of the pixels in the detector so a high spatial resolution is achieved with smaller pixels.

The detector will need to be a monochrome detector as it will only have to acquire images in grayscale. It will also need to be at least 8-bit grayscale or higher. This will allow for 256 grayscale values so the detector will have a higher dynamic range. Higher dynamic range provides larger photon collection capability which is advantageous in low contrast detections.

Historically, a detector with < 10 μm pixel size has lower inherent quantum efficiency. Quantum efficiency is the probability of getting a digital signal given that a photon of the appropriate wavelength is incident on the detector [35], and is typically > 90 % quantum efficiency [4]. In addition, CMOS detectors tend to be much more cost-effective than their counterparts and more readily accessible. Additionally, CMOS detectors are available in compact webcam versions that are easily interfaced with a computer and are ready to use with minimal preparation time.

Distance to the Detector

The distance from the two manipulating mirrors to the detector (L), is important. This distance, which is the length over which the light from the two pupils will be overlapped, has an optimal range based on the wavelength of the light source, the separation of the pupils, and the range of fringe frequencies that can be observed on the detector.

The fringe frequency equation for the aluminum phantom placed at the focal plane (Equation 3.2) will be used here. The detector can accept a minimum fringe frequency of $\mathcal{F}_{min} = \frac{1}{N_x \, \delta x}$. This means there is one light and one dark fringe observable on the detector which would correspond to

$$L_{max} = \frac{d \, N_x \, \delta x}{\lambda_\circ}. \tag{3.23}$$

The maximum accepted fringe frequency is $\mathcal{F}_{max} = \frac{1}{2\delta x}$, meaning that every other pixel across the detector represents a light fringe which corresponds to

$$L_{min} = \frac{2d \, \delta x}{\lambda_\circ}. \tag{3.24}$$

This minimum distance can be reduced if d is decreased and $\lambda_\circ$ is increased. However, if the wavelength is increased, the lateral imaging resolution of the system decreases. The axial resolution of the system would also suffer if the wavelength increases and the distance between the pupils decreases. This will be shown in § 3.5.2.

For the prototype, $\lambda = 653$ nm, $d = 37$ mm, $N_x = 752$, and $\delta x = 6$ μm. There is a window in $\mathcal{F}$-L space from which the length L can be determined, shown in Figure 3.16. This allows for $L_{min,max} = 0.662 - 248.7$ m. Clearly, this is a very wide range in distance and it is obvious that L should not be close to either extreme. The next section describes the process of choosing a suitable separation between the detector and the relay mirror and hence the overall size of the instrument by examining the relationship between the axial resolution and L.

3.3.5 The Size of LIFT

Being an instrument chiefly designed for coarse microscopy, LIFT aims to be very compact and self-contained. Aside from the sheer size of all the components used in LIFT, the overall size of the instrument is dictated by some of the design choices.
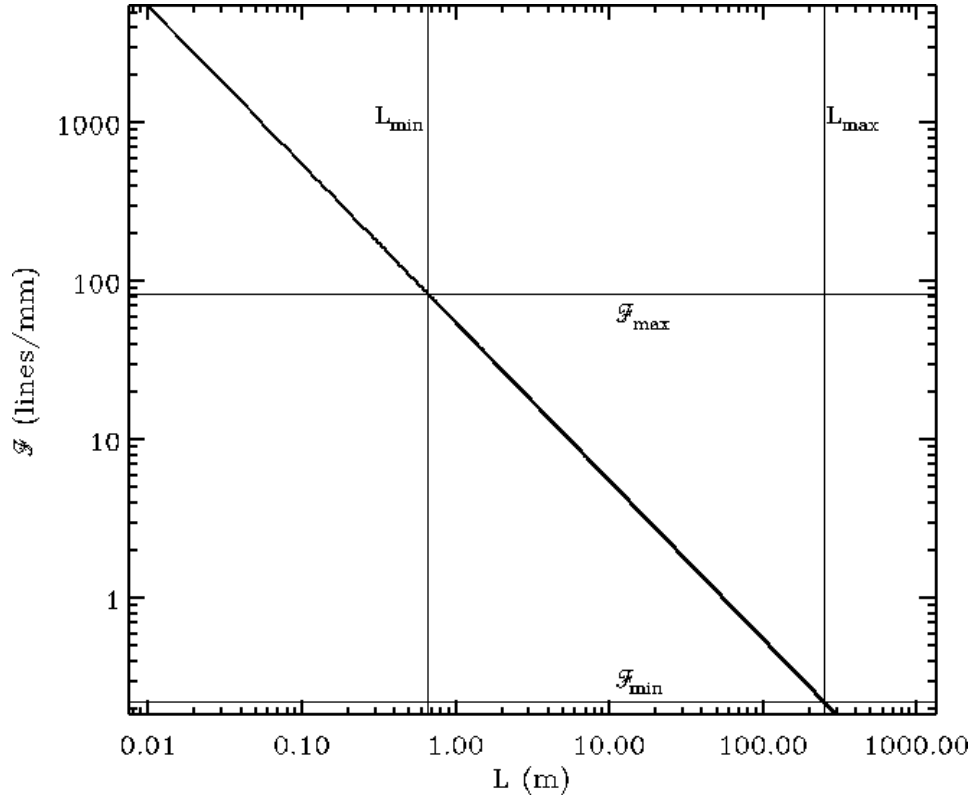
Figure 3.16: The fringe frequency in lines per millimeter as the distance L, is varied from 0-300 m. The two Horizontal lines denote the minimum and maximum $\mathcal{F}$ for the detector chosen in this version of LIFT and the two vertical lines are the corresponding minimum and maximum L.

The lens in LIFT is an f/2 lens. The reasons for this choice were to only collect the light within a cone angle of $\sim 26°$ and to decrease the depth of field of the instrument.

The two remaining parameters that contribute to the overall size of the instrument are the distance between the mask and the two mirrors (l_{mm}), and the distance from the relay mirror to the detector. In order to determine these two quantities, their impact on the axial resolution of LIFT was considered. A simple simulation was carried out that examined how the axial resolution is effected by varying l_{mm} at constant Ls, based on the derived axial resolution equation of LIFT (Equation 3.26). Figure 3.17 shows the result of the simulation. Since the distance between the mirrors and the detector has a prescribed range, six values for L were used to investigate the behavior of the axial resolution as a function of l_{mm}.

The magnified region in Figure 3.17 is where the l_{mm} and L values are chosen by considering the axial resolution of interest. Since the theoretical lateral resolution of LIFT is 53 μm, calculated in § 3.5.1, the theoretical axial resolution of the instrument is chosen to be one and a half times larger than the lateral resolution at 80 μm. The resulting l_{mm} and L are 0.448 m and 0.892 m, respectively.
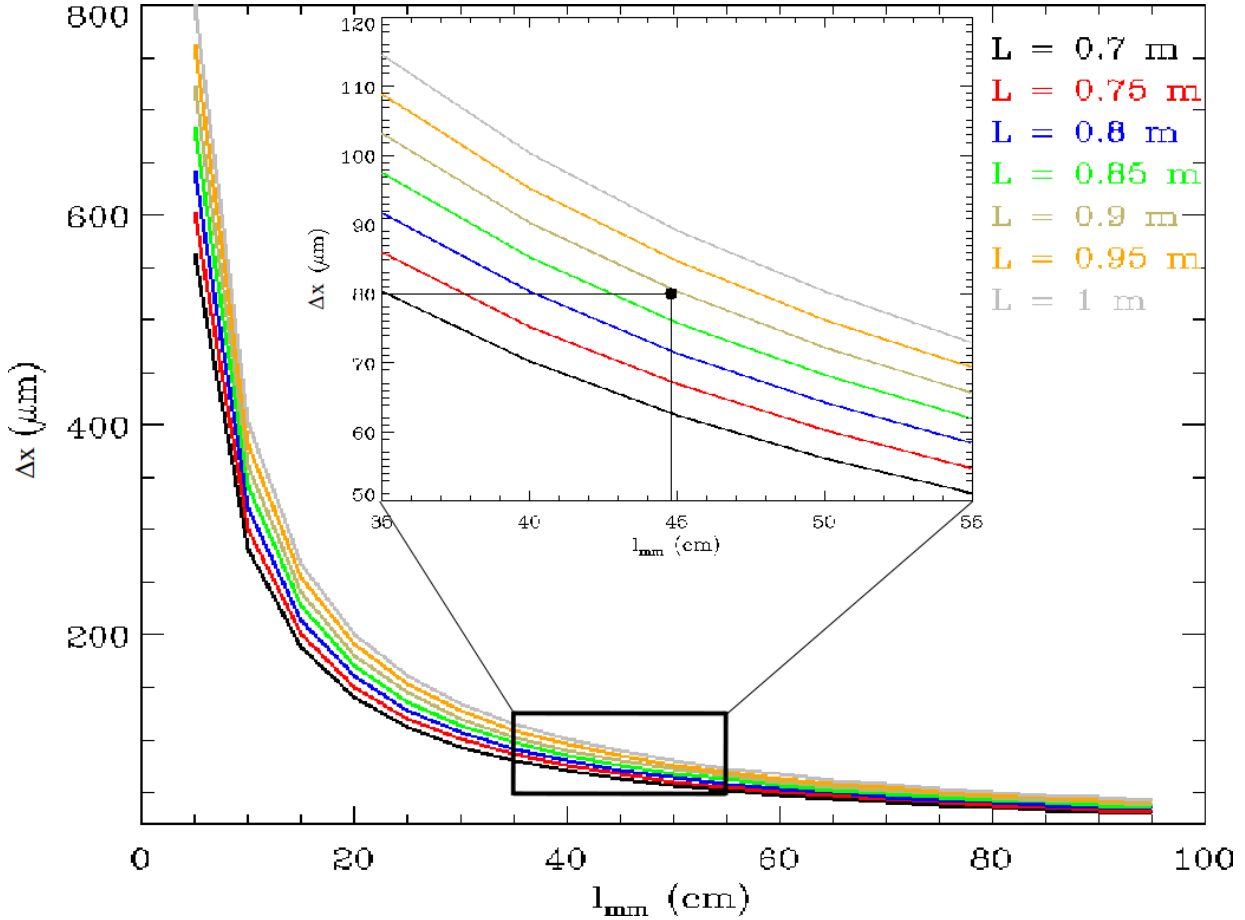
Figure 3.17: The plot shows the impact of varying l_{mm} on the axial resolution of LIFT at constant a L. The region from which the values of l_{mm} and L were selected is expanded and the chosen l_{mm} at the corresponding axial resolution is shown by a bullet.

3.4 The Prototype

A prototype of the 1st generation of LIFT was built in the laboratory (see Figure 3.18) to serve as a testbed for proof-of-principle of this imaging modality. The optical beam paths

have been shown by arrows and have been color-coded for ease of recognition. This is the most simplistic view of this instrument.
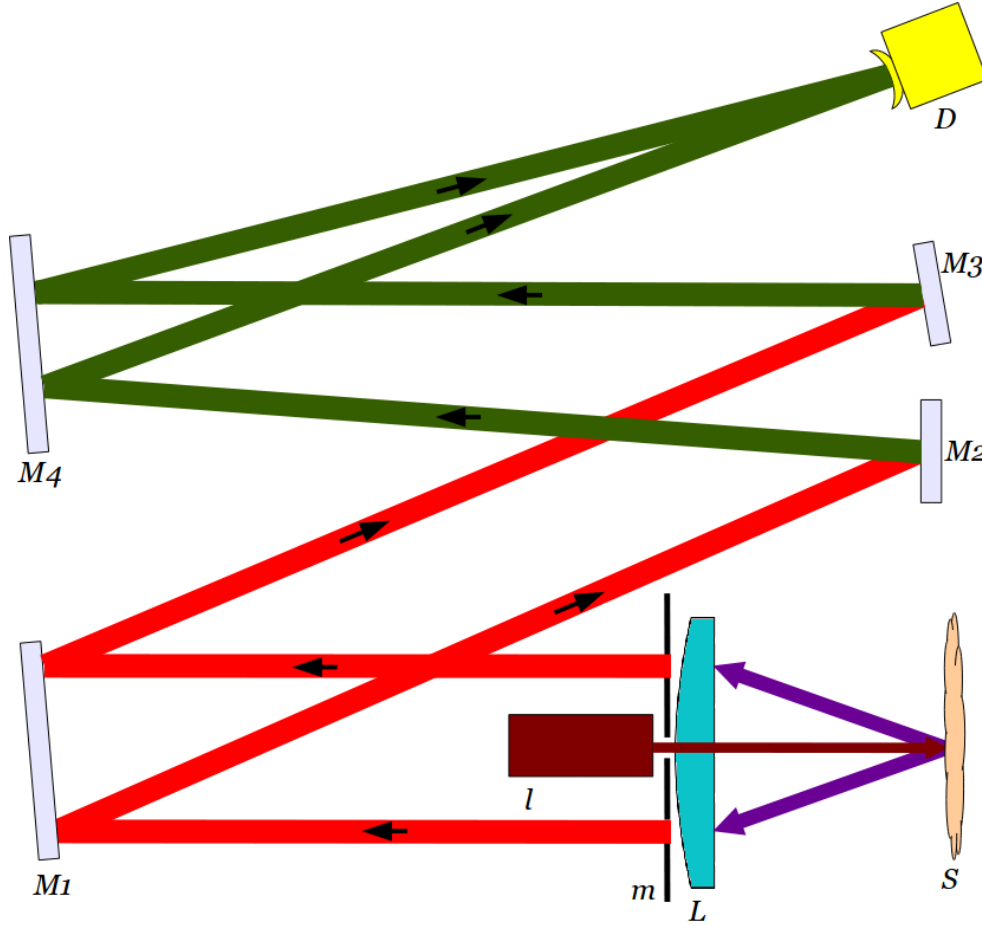
Figure 3.18: The cartoon schematic of LIFT prototype.

Each of the optical elements has beeb labeled. Going through the instrument following the light propagation, the laser light originates from the source (l), passes through the mask (m) and is then focused by the lens (L) onto the sample (S). The sample produces reflections and backscatter of the light which is collected by the lens and collimated. The collimated aperture of light is sampled by two pupils in the mask. The two pupil beams are reflected off of a fold-flat mirror (M1) and are incident on the relay (M3) and the manipulating (M2) mirrors. The light from the mask to the relay and manipulating mirrors is colored red to signify the distance of l_{mm}. The light beams reflected by mirrors M2 and M3 encounter another optical fold-flat mirror (M4) on their way to the detector (D). This light path

is colored in green to signify the process of overlapping the two beams and the distance L. Note that the two light beams out of the pupils are parallel (separated by d), which signifies that the sample has to be located at the focal plane of the instrument.

The laser diode is a 2 cm long and 5 mm wide compartment that is very light so it can be attached directly to the mask. This is done to ensure that the beam emerging is collimated since the beam tends to expand as it travels farther from its source. In addition, it avoids the need for various mounting apparatus and fold-flat mirrors to direct the light to its destination. The laser is powered by a 3 V DC power supply.

The light is focused down onto the sample by the focusing/collimating lens. It is very important to illuminate the lens on its principle axis so the beam of light comes to focus on the focal plane at the principle axis, and is not deflected off of it. This is not a simple task while not having a carefully machined housing for the optical elements. In the LIFT prototype the laser is placed as close to the principal axis as possible. The same lens works to collimate the scattered light returning from the sample. A simple plano-convex singlet lens with good throughput at the desired wavelengths is sufficient for this application. As mentioned previously, an f/2 lens is needed as only the light within a cone angle of 26° emerging from the sample is deemed to be useful for measurement. To accommodate the size of the relay and manipulating mirrors along with their mounting hardware, a 50 mm diameter lens with a focal length of 100 mm is chosen.

The collimated light then encounters the mask (Figure 3.19) which is a screen of anodized aluminum containing three holes. One hole is located on the principal optical axis, which is where the laser beam passes through to the lens. The size of this hole is sufficient to allow for the laser beam to go through without any clipping. The other two holes are symmetric about the optical axis. The light in the collimated aperture is absorbed except for the light that passes through the two pupils. It is very important to reduce any back reflections and scattering from the mask to prevent any light returning through the lens.

The size of the mask is chosen to be slightly larger than the diameter of the lens used in the system. A 3 mm diameter hole in the center is used to guide the laser beam through the optical axis of the lens in order to illuminate the sample. The pupils, symmetric about the optical axis, are 5 mm in diameter and are separated by the largest distance possible of $d = 37$ mm. For 5 mm diameter pupils, the separation distance has a maximum limit of 37
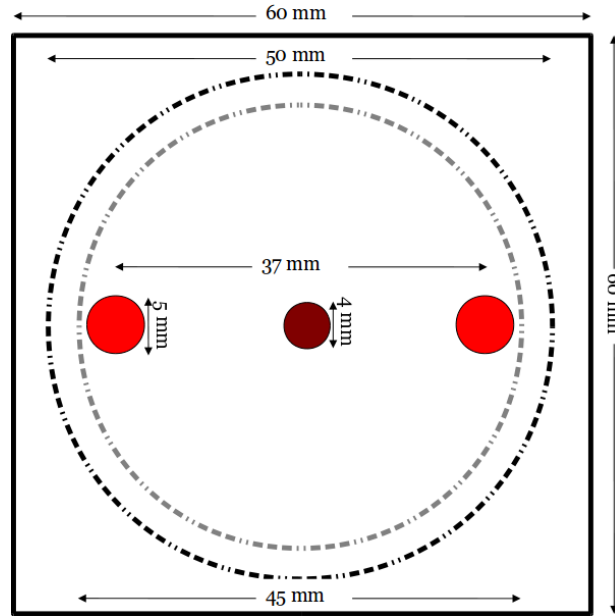
Figure 3.19: The mask in the LIFT prototype. The pupils surround the center hole where the laser light passes through. The silhouette of the lens behind the mask (black dashed-dot line) and the clear aperture (gray dash-dot line) are shown for reference.

mm and a minimum limit of 10 mm. For testing purposes of the prototype, the maximum separation between the two pupils was chosen. The impact that the separation has on the system will be shown in § 3.5.2.

The optical fold flats in the prototype are 50 mm mirrors and the relay and manipulating mirrors are both 25 mm in diameter. These are broadband dielectric mirrors which offer > 99 % reflectivity over the spectral wavelengths range 350 - 900 nm. The manipulating mirror is mounted on a kinematic mount for ease of changing the tip and tilt of the pupil beam reflecting off of it.

Next, the interference pattern is imaged with a camera which is a simple webcam (focusing lens removed). The image is then stored for processing. The camera is an 8-bit monochrome CMOS detector comprised of a 4.5×2.9 mm chip of 6 μm square pixel pitch.

The sample being imaged by LIFT is to be placed on a platform which allows for X-Y-Z displacement. This allows for focusing the imager by moving the sample toward or away from the lens, and enabling two- and three-dimensional imaging of the sample in order to acquire depth profiles necessary for the reconstruction of such images.

For the LIFT prototype two linear stages are used (X- and Z- directions) which are operated manually. These stages allow for focusing the instrument and acquiring B-scans. In future iterations of LIFT. At ∼ \$4,000, the fully automated sample handling sub-system of LIFT will be by far the most costly aspect of this instrument. This element will consist of three linear translation stages with 3 μm straight line accuracy and two automated linear actuators. The linear actuators will be used to automate the two- and three-dimensional image acquisition.

The mounting hardware used for the LIFT prototype is standard issue, commercial-off-the-shelf equipment. For future iterations of LIFT, especially when it is in the commercialization phase, a custom housing will have to be built which would potentially contain the entire instrument.

Figures 3.20 and 3.21 show the LIFT prototype used for testing in the laboratory. All components used in the prototype are commercial-off-the-shelf and total to ∼ \$1,000 in cost.
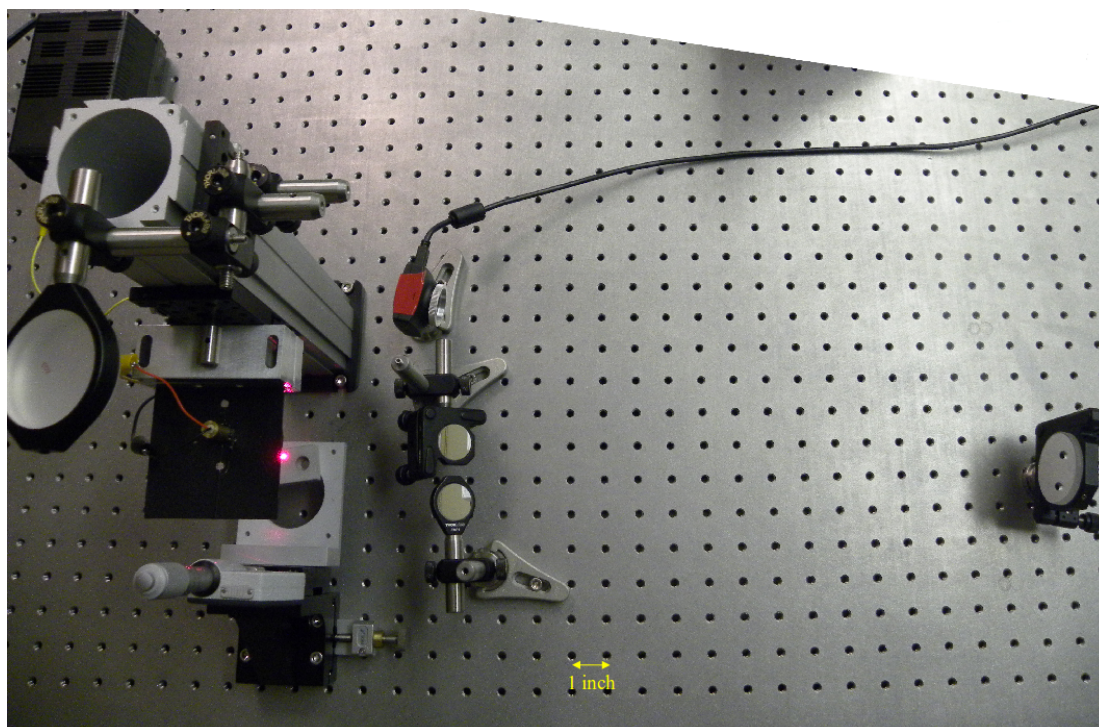
Figure 3.20: Photograph of the LIFT prototype.
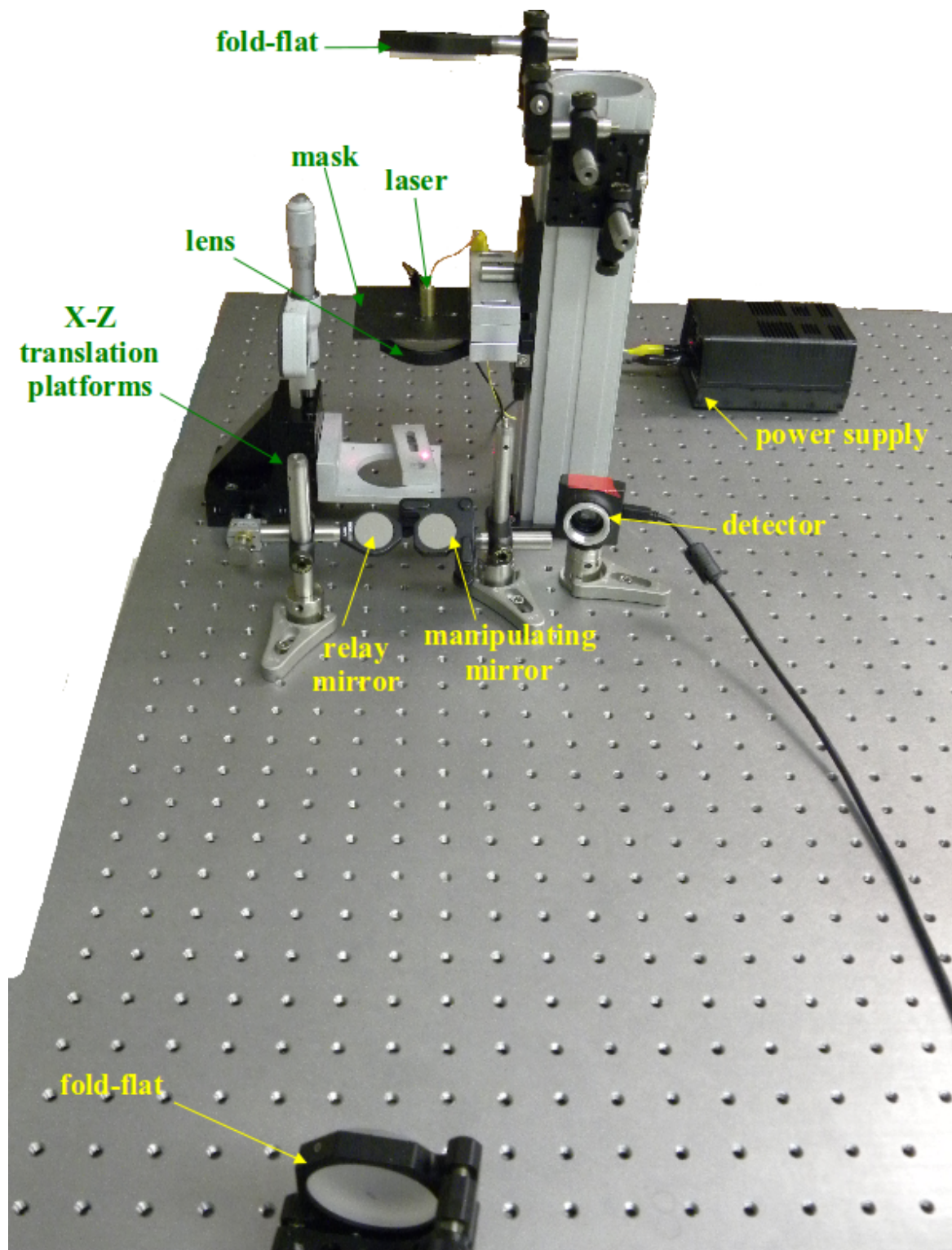
Figure 3.21: Photograph of the LIFT prototype with various parts labeled.

3.4.1 Determining the Wavelength and Stability of the Laser Source

The laser diode used in the LIFT prototype was purchased from an internet vendor and the operational and performance specifications of it were not clear.

In order to measure the central wavelength of the light source, a spectrograph was built in the laboratory and its dispersion relation is well-fit by a third-order polynomial of form

$$\lambda = -7.8 \times 10^{-10} px^3 - 4.7 \times 10^{-7} px^2 + 0.067 px + 492.04, \tag{3.25}$$

in units of nm and where the quantity px is the horizontal pixel of the detector. A dispersion relation of a spectrograph describes how the input light is dispersed into its wavelength constituents on the detector of the spectrograph. It differs from one spectrograph to the next and has to be experimentally derived for each device.

The light source of LIFT was examined with the spectrograph and its emission line was measured seven times. The measured spectra were averaged and plotted in Figure 3.22 top (empty circles). Using a curve fit algorithm a Gaussian profile was fitted to the data and is shown in the same figure with a solid red line. The residual between the fit and the actual data is shown in the bottom section of the same figure (filled circles). The standard error between the actual data and the Gaussian fit is 0.008. The fitted parameters are shown on the figure. The central wavelength of the laser diode source used in the LIFT prototype was determined to be $\lambda_\circ = 653.29 \pm 0.18$ nm.

Next, the thermal stability of the light source was studied. The spectrum of the laser was measured after the diode was handled in order to couple it to the spectrograph. The temperature of the diode casing was increased by a few degrees Celsius. Figure 3.23 shows the spectra of the laser starting from an elapsed time of zero minutes, immediately after being handled, to 90 minutes. As postulated, the diode laser is prone to thermal fluctuations however after about 45 minutes of a major thermal event it settles down to a stable emission spectrum.

The central wavelength of the laser only changed by ~ 0.6 nm after being exposed to a temperature a few degrees higher than the ambient. As shown before, a fluctuation of sub-nanometer scale will not have any measurable consequences on the LIFT prototype.
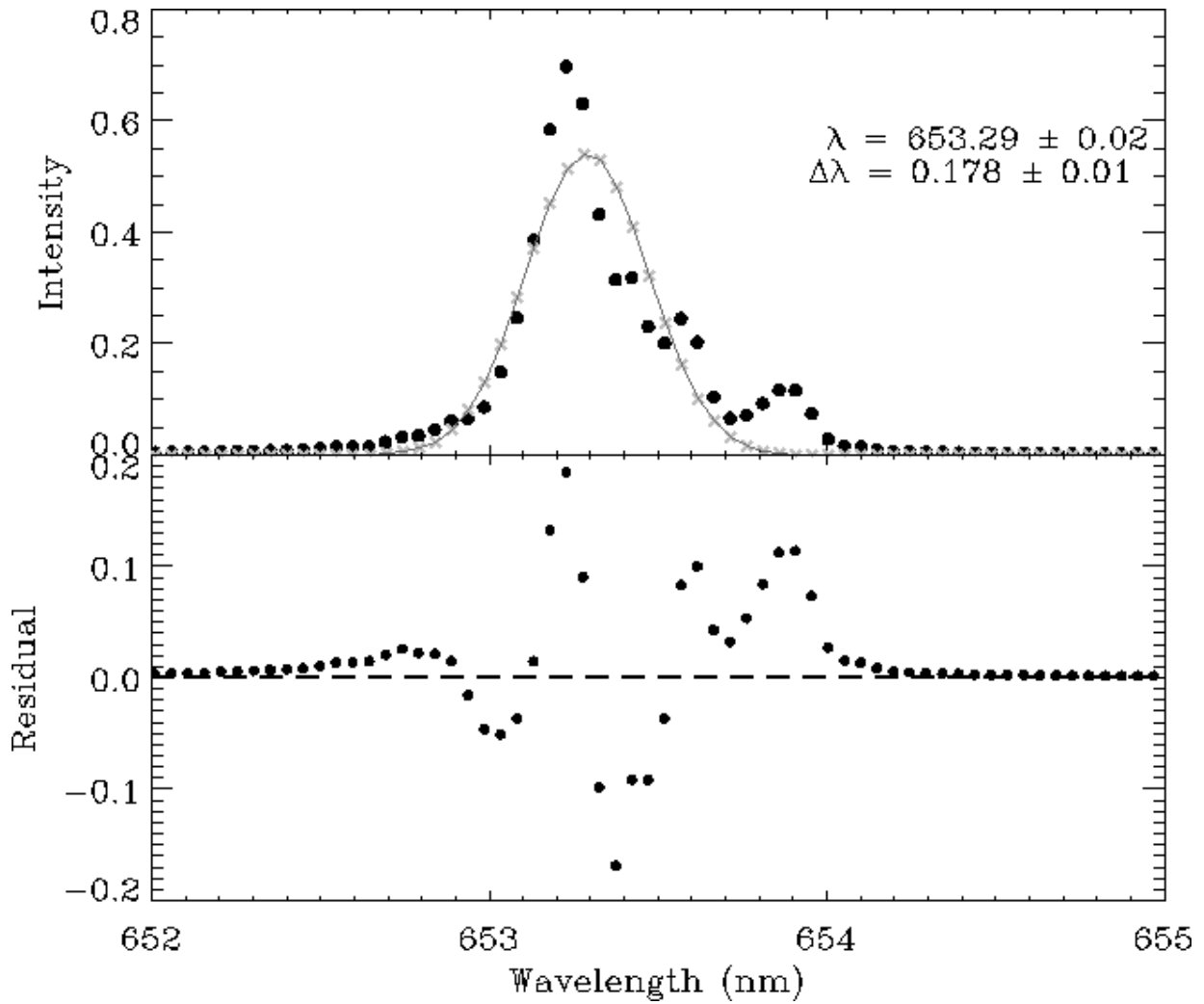
Figure 3.22: The top panel of the figure shows the time-lapse average of the measured wavelength of the diode laser (black filled circles) and the model Gaussian fit to the data (gray). The bottom panel shows the difference between the measured data and the model.
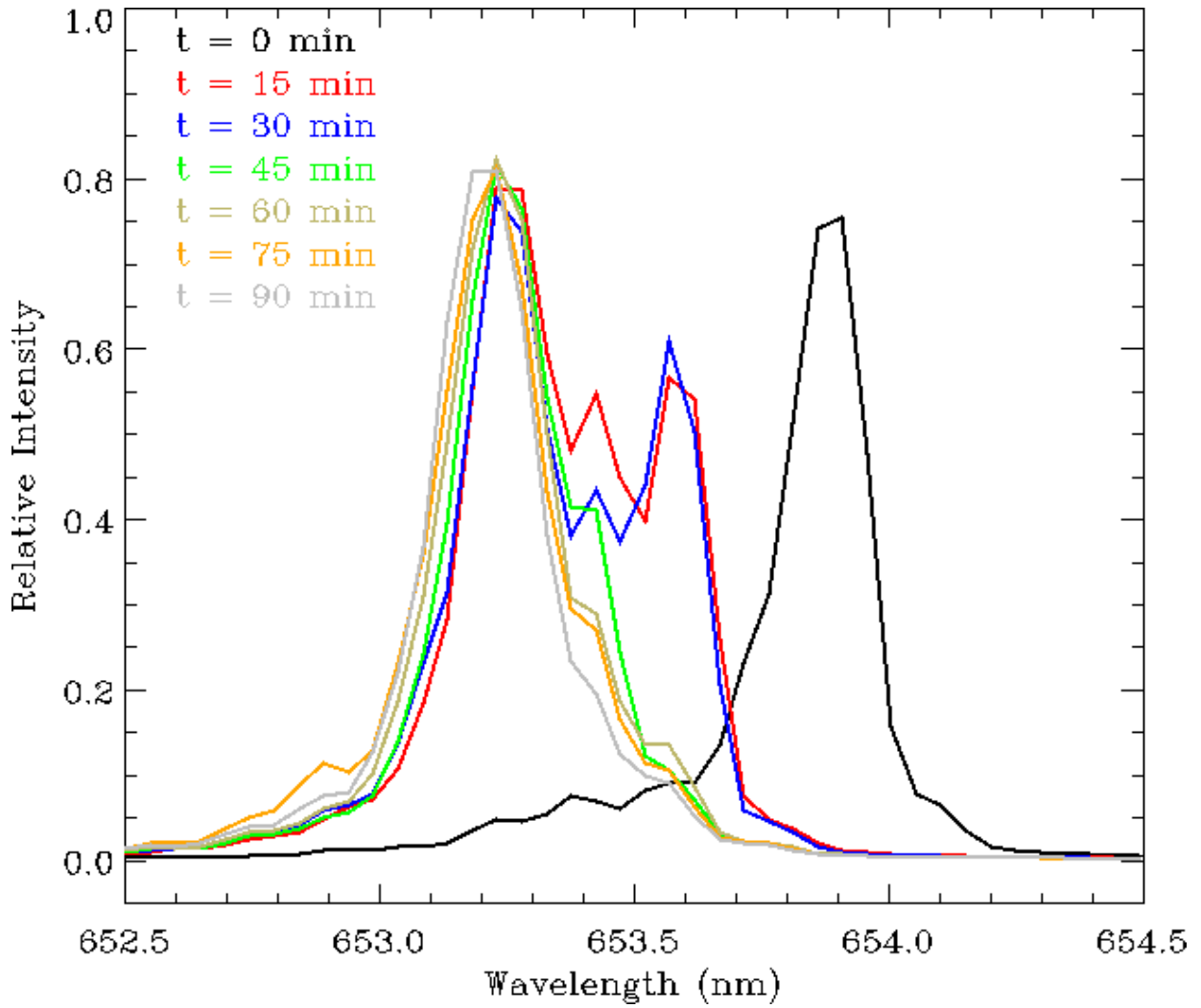
Figure 3.23: The time lapse spectrum of the laser after coupling to the spectrograph. The spectra are color-coded based on elapsed time after a thermal event.

3.5 Theoretical Imaging Properties

Having theorized all physical aspects of LIFT either through design or optimization, this section will summarize the theoretical performance properties of LIFT. The higher the frequency interference pattern, the farther away from the focal plane the signal has originated from (larger x). The maximum theoretical imaging depth refers to the x at which the highest fringe frequency can be measured on the detector.

3.5.1 Lateral Resolution

The lateral resolution of this instrument is described by the size of the focused spot at the focal plane of the instrument. It can be theoretically computed using Equation 2.4 with the now fixed values for the variables in the equation.

The wavelength of the light source has been determined to be 653 nm, the focal length of the lens is 100 mm and the diameter of the laser beam before it is focused by the lens is 3 mm. Assuming that the index of refraction is one for air, the smallest size of the focused spot of LIFT (R_l) is computed to be 53 μm. The smallest discernible feature that could be imaged is half of the focused spot size $\frac{1.22}{n} \frac{\lambda_\circ}{D} f$.

3.5.2 Axial Resolution

In LIFT, it is the fringe frequency which will determine the depth. In other words, the number of fringes observed on the detector of N_x pixels at a certain size δx due to the signal returning from the focal plane of the instrument is given by Equation 3.3.

Observing more or less fringes infers that the sample has moved farther away or closer to the lens. The smallest distance that the sample can move from the focal plane and result in one more or one less fringe is determined to be the axial resolution of LIFT. Equation 3.13 describes the number of fringes observed as the result of the sample not being at the focal plane, with x being the distance that the surface has moved from the focal plane.

Thus, if one more fringe is observed on the detector than when the sample is at the focal plane, it can be attributed to light that is returning from $f + \Delta x$. The quantity Δx

is the axial resolution of LIFT and can be written as

$$\Delta x = \frac{\lambda_\circ \; L \; (d^2 + 4f^2)}{4d \; l_{mn} \; N_x \; \delta x}.$$ (3.26)

At $\lambda_\circ = 653$ nm, $L = 89.2$ cm, $d = 37.32$ mm, $f = 100$ mm, $l_{mm} = 44.8$ cm, and a chip width of 4.5 mm, the axial resolution of LIFT is 80 μm which is $1.5R_l$. The axial resolution can be increased by decreasing the wavelength, the distance between the relay mirror and the detector, the distance between the pupils and the focal length of the lens, and by increasing the distance between the mask and mirrors and the width of the detector chip.

3.5.3   Maximum Imaging Depth

The maximum imaging depth of LIFT can theoretically be determined by considering the maximum amount of fringes that can be observed on the detector. Using Equation 3.27 and considering the maximum fringe frequency $\mathcal{F}_{max} = \frac{1}{2\delta x}$, the distance x_{max} behind the focal plane at which the light has to be backscattered from is determined to be

$$x_{max} = (\frac{L \; \lambda_\circ}{2d \; \delta x} - 1) \; (\frac{d^2 + 4f^2}{4l_{mm}}).$$ (3.27)

The value of the x_{max} is determined to be 6.9 mm.

Note that this is the theoretical potential of LIFT and there are limiting factors which would prevent this amount of imaging depth one such example is the depletion (absorption and transmission) of the light as it penetrates into a sample. The size of the relay and the manipulating mirrors can effect the maximum depth also since after considerable deflection out of the pupils, ϵ, the beams will not be incident on the surface of the mirrors. These mirrors have to be a size that would allow them to be situated close to each other while both accepts and reflect either one of the pupil beams. The size of the pupils is another limiting factor to the imaging depth, since the two beams have to be superimposed for interference to occur. Larger pupil sizes will enable larger imaging depth because the area of superimposition would be larger. There is, however, a physical limitation to how large the pupils can be. They must be smaller than half of the clear aperture of the lens while maintaining the structural integrity of the mask.

The maximum imaging depth derived here assumes ideal conditions, meaning that none of the above-mentioned limitations are at work. The maximum experimental imaging depth of LIFT will be determined in the next chapter.

Chapter 4

Imaging with the Laser Interference Fringe Tomography Instrument

Thus far LIFT has been designed, mathematically described, prototyped, and its performance capabilities have been theorized and presented. This section describes how imaging is done using LIFT. The data acquisition procedures are laid out and a processing pipeline is established and discussed. The practical imaging capabilities of LIFT are then assessed and compared with the theoretical predictions previously set out. Following that is a section reporting on the imaging tests of various samples done with LIFT. Some general comments about LIFT's imaging capabilities complete this section.

4.1 Data Acquisition

Imaging with LIFT is done by placing a sample at or near the focal plane of the instrument. Ideally, the surface of the sample would be placed near the focal plane. This will ensure that the light returning from the sample will be from behind the focal plane and the interference pattern will therefore have a higher fringe frequency than the interference pattern at the focal plane.

Doing this will also allow for the alignment of the instrument. The alignment of LIFT is done by ensuring that the surface of the sample is placed at the focal plane. If this has been accomplished, the light emerging from the lens will appear to be collimated planoparallel light. When the collimated aperture of light encounters the mask, the emerging

light from the pupils will be parallel or separated by the same distance over a few meters. Therefore, before any imaging session, the collimation of the beam has to be verified by controlling the vertical position of the sample using the X-axis movement of the sample handling system. This should be the only alignment process that has to be done before using LIFT, assuming care has been taken to mount the lens without any tilt and also that the laser is mounted to illuminate the lens at its principal axis. A discussion of the misalignment and tolerancing of the lens and the laser of LIFT is beyond the scope of this document.

To simplify the image acquisition process, a custom Windows-based graphical interface was developed using the *.net* framework. This graphic user interface harmonizes the camera acquisition software, includes some image processing tools, allows for automated image capture, and provides an easy file-naming protocol, see Figure 4.1.
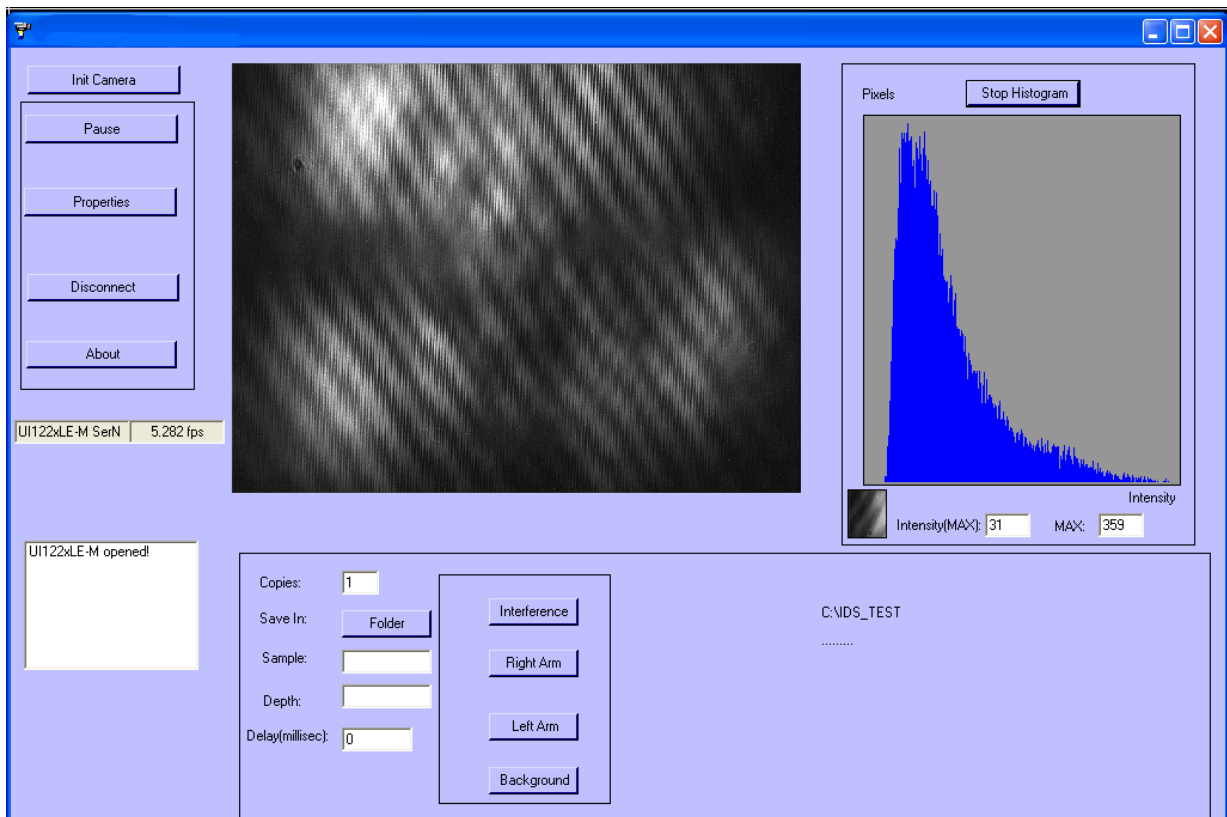

Figure 4.1: A Windows-based graphical user interface developed for LIFT batch image capture.

With proper alignment of the system an interference pattern is observed on the detector, an example of which is shown in Figure 4.1. The exposure time of the detector is chosen to ensure that there are no saturated pixels and to stretch the dynamic range as much as possible between the minimum and maximum gray-levels available. The exposure time for data acquisition differs depending on the sample being probed.

Theoretically, the albedo of the sample will dictate the limit on the exposure time. The exposure time also depends on μ_t of the sample which is the sum of the absorption and scattering coefficients of the material and the size of the pupils. For a more in-depth radiometric study refer to § 3.3.3. A typical exposure time for the aluminum phantom (a sandblasted aluminum block with $\mu_t = 1$ mm^{-1} at optical wavelengths) is ~ 0.4 ms if it is illuminated with a 5 mW laser. The exposure time must be determined before imaging is to be done.

When LIFT has optimal operating conditions, data acquisition can begin. First a snapshot of the interferogram is captured. Then, a snapshot of each individual pupil beam is taken while the other is blocked. Lastly a snapshot of the background light levels (dark noise) is taken by blocking both arms. The combination of these four images are necessary to properly process the data to produce a 'depth profile' or A-scan.

To probe a sample in two dimensions (a B-scan) a linear stage is used to translate the sample under the beam in interval steps-size of the lateral resolution of the system. A three-dimensional image can be acquired by aligning a series of B-scans if the sample is translated in the third dimension, again by the lateral resolution step-size. It is important to note that multiple snapshots of the interference pattern, the left and right arms, and the background noise are captured for each A-scan. This allows for statistical averaging of the images in the processing step which tends to decrease the random photon noise present in any optical imaging system. The optimal number of snapshots is determined later.

The LIFT prototype is capable of manually producing B-scans of various samples. However, the image acquisition of this system will have to be automated for ease of use and to reduce the imaging time. For a fully automated system, a beam blocking system has to be devised in order to automatically block both beams for each A-scan. The beam blocking system, the camera, and the two linear stages (used for three-dimensional scanning) will have to be controlled by one encompassing software with feedback control loops.

4.2 Data Processing

The goal of LIFT is to be able to determine the structure within a sample based on the reflection and scattering event. In general, a reflection within a sample only occurs when there is a change in the index of refraction. For example, in a human tissue sample the index of refraction of the muscle and the fat are different. Whenever the laser illuminates this boundary, a reflection is produced and is encoded in the interference pattern observed. A certain percent of the light is scattered at that boundary and the rest of the light will travel into the sample. The remaining light will either be absorbed by the sample, diffusely scattered, or will encounter another major scattering and will emerge from the sample. This process will continue until all the incoming photons have been consumed or scattered out of the sample.

Response from any detectable depth within the sample will produce a characteristic interference pattern corresponding to that specific depth. So, if there are multiple levels of scattering events in a sample from which light is returning, the combined interference pattern will be observed. In order to produce an A-scan from the interference pattern an IDL® [1], a routine was developed (see Appendix). The image processing pipeline is described in a step-by-step manner.

The observable interferogram has mathematically been described in Equation 2.20, providing insight about the light contribution of each of the pupils along with the coherence of the light. The data reduction is done by simply manipulating this equation in order to extract a periodic functional form of the light intensity. This periodic function is the interference pattern which ultimately infers information about the sample being probed.

After capturing multiple snapshots of the interferogram, the left and the right arm, and the background (black-noise), the first step in processing the LIFT data was to apply the Canny edge-detection algorithm [8] to the interferogram to create an 'edge map'. The 'edge map' was added to the original interferogram to accentuate the edges of the fringe patterns. This process will enhance the contrast in the transition between the bright and dark fringes.

---

[1]IDL, short for Interactive Data Language is vectorized, numerical, and interactive, and is commonly used for interactive processing of large amounts of data (including image processing). The syntax includes many constructs from Fortran and some from C. Provided by ITT Visual Information Solutions.

The background images were then negated from the interference, the left arm, and the right arm images to remove any contribution of tray light in the system and the detector readnoise. The interference equation becomes

$$I_b = I_{0,b} + I_{1,b} + 2\sqrt{I_{0,b}\ I_{1,b}}\ |\gamma(\mathbf{r}_0, \mathbf{r}_1, \tau)|_b\ cos(\omega_\circ \tau), \tag{4.1}$$

setting ϵ and μ to one for the purpose of this derivation.

Next, the left and right arm images were negated from the interference images to remove contributions of any over- and under-density of light introduced into the interferogram. As well as, deconvolving the square-root of the product of the left and right arm images from the interferogram:

$$\frac{I_b - I_{0,b} - I_{1,b}}{\sqrt{I_{0,b}\ I_{1,b}}} = A\ cos(\omega_\circ \tau), \tag{4.2}$$

where $A = 2|\gamma(\mathbf{r}_0, \mathbf{r}_1, \tau)|_b$. At this point, a two-dimensional Fast Fourier Transform (FFT) can be performed

$$FFT\left[\frac{I_b - I_{0,b} - I_{1,b}}{\sqrt{I_{0,b}\ I_{1,b}}}\right] = FFT\left[A\ cos(\omega_\circ \tau)\right], \tag{4.3}$$

on the image which will extract the frequency of the cosinusoidal function which in turn can be converted into distance from the focal plane. The result of the FFT will have to be binned in the vertical direction in order to observe a 'depth profile'. This will yield an accurate result if and only if the interference fringes are completely vertical.

A noticeable quality about the observed two-dimensional interferograms is that the fringes are in most cases, not vertical. In theory, the two-dimensional detector can be replaced by a one-dimensional one and the same interference pattern would be observed. In addition, the interference pattern is not stable which means that a given pixel on the detector will not maintain one mean level of photon counts at any given time. Figure 4.2 shows the spread in the digital count in one specific pixel on the detector while observing the same interferogram 1000 times. The distribution of the count in the pixel is Gaussian about a mean of 75 counts, however this instability is not desired for interferometric imaging applications.

Considering these two difficulties, it is clear that the interferogram has to be processed one row at the time. Each row of this two-dimensional interferogram can independently
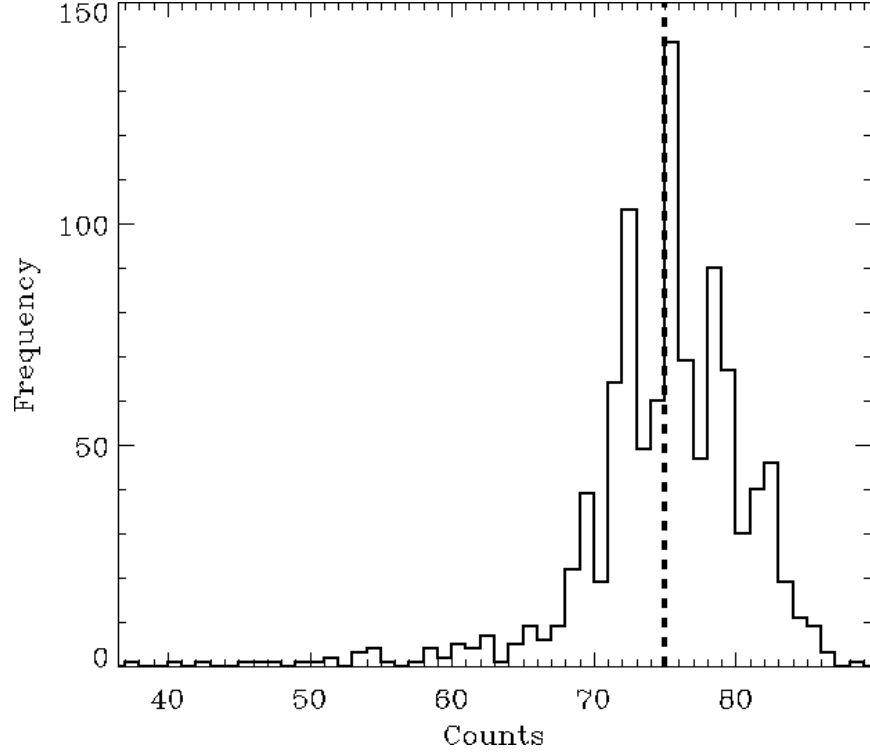
Figure 4.2: Digital count in pixel (376,240) of the LIFT detector in 1000 captures of an identical interferogram. The dashed vertical line shows the count mean level.

provide the necessary information about the internal structure of the sample. The advantage of a two-dimensional detector is that it provides N_y times the number of interference patterns which will be exploited in data processing to multiplex the 'depth profile' to reduce noise levels in the system. So, whether the fringes are completely vertical or not falls below the tolerance levels of a single row of the interferogram.

The two-dimensional interferogram, shown in Figure 4.1, was dissociated into N_y rows of one-dimensional interferograms so they can be analyzed individually. Therefore, the FFT routine was performed on each individual row and the resulting frequency spectra are averaged together. This can be described by,

$$FFT\left[\frac{I_b[*,i] - I_{0,b}[*,i] - I_{1,b}[*,i]}{\sqrt{I_{0,b}[*,i] \; I_{1,b}[*,i]}}\right] = FFT\left[A \; cos(\omega_\circ \tau)\right], \tag{4.4}$$

for the ith row. The result of the FFT is a power spectrum peaking at $\frac{A}{2}$ intensity and $(\mathcal{F} \; N_x \; \delta x)$ frequency. This power spectrum is then converted to strength of scattering

as a function of the distance from the focal plane which was previously defined to be the A-scan. The number of averaged power spectra necessary in order to maximize the signal and reduce the noise will be determined later.

It is worth mentioning that the visibility of the fringe pattern, Equation 2.11, is calculated for each row of the two-dimensional interferogram. The FFT was only performed on rows with $\mathcal{V} > 0.75$ and only these power spectra were used to produce an A-scan. All other rows were omitted from the processing pipeline. In-depth analysis of the various processing methods such as noise reductions and interferogram enhancements are beyond the scope of this work and will not be discussed here.

4.2.1   Interferogram Rotation

There is no gaurantee that the fringes in the two-dimensional interferogram will be completely vertical. A simulation was carried out to show that considering each row of the captured interferogram as an independent one-dimensional interferogram will yield more robust A-scans with improved signal-to-noise ratio.

In this simulation, a bitmap of an ideal two-dimensional interference pattern was created. Ideal in this case refers to an interferogram with no noise or distortions and completely vertical fringes. The frequency of the two-dimensional sinusoid is 290 or a fringe frequency of 64.27 lines/mm. The bitmap is then rotated about its center in steps of one degree, clock-wise, up to ten degrees. The resulting bitmap at each degree of rotation is processed in two different ways. One is to vertically sum (bin) all of the pixels in the image and perform an FFT on the resulting sinusoid to create an A-scan. The other is to perform the FFT on individual rows of the bitmap to create an A-scan and then average the resulting A-scans.
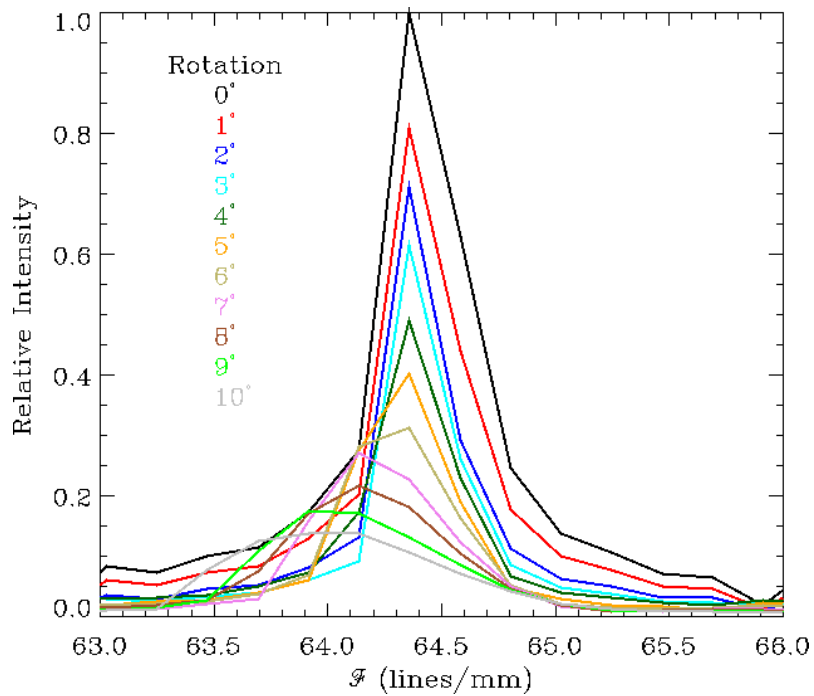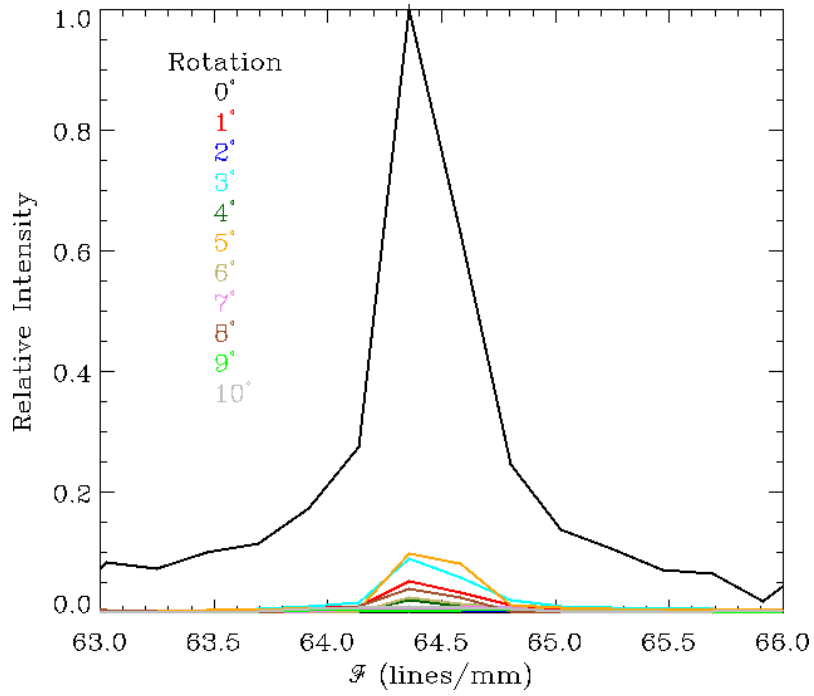
Figure 4.3: A-scan of a rotating dataset. The A-scan is created by vertically binning (top) and averaging the resulting A-scan of each row (bottom) of the two-dimensional interferogram.

Figure 4.3 shows the A-scan resulting from using each method, at a particular degree of rotation of the interferogram. The plotted intensities have been normalized to the peak intensity of the ideal dataset. Both methods show the correct fringe frequency of the interference pattern. However, the peak of the signal seems to decrease in intensity as the interferogram is rotated farther from the vertical until it is washed away in the noise. The behavior of the A-scan as a function of the rotation seems to be more predictable in the bottom plot of Figure 4.3 as it decreases with a higher angle of rotation. Conversely, the intensity of the A-scan in Figure 4.3 top diminishes abruptly to a tenth of the peak intensity. The behavior of the A-scan is not predictable as the 5° rotated interference pattern seems to yield an A-scan of higher intensity than the 1° or 3° rotated interferograms. In addition, when the two-dimensional interferogram is binned vertically, the resulting one-dimentional interference pattern seems to contain additional frequencies as the tilt in the interference pattern creates sinusoids of different phase difference. The addition of these sinusoids would result in corrupted data. The method of row-by-row processing of the interferogram remains rotationally invariant and produces an accurate, consistent, and reliable results. Both methods of processing the data seem to reach their limit when the interferogram is rotated more than 6° from the vertical.

4.3 Imaging Capability

In this section, some of the key imaging properties of LIFT such as the observed signal-to-noise ratio, imaging resolution, and the maximum imaging depth are experimentally investigated. The results of this section will help to characterize the instrument. In the process of commercializing LIFT, an in-depth analysis of the imaging capabilities of the instrument will need to be carried out. These efforts are beyond the scope of this work.

4.3.1 Signal-to-Noise Ratio

Signal-to-noise ratio (SNR) is a measure that compares the level of signal to the level of background noise. It is defined as the ratio of signal power to the noise power. A quotient of higher than one indicates more signal than noise and the desire is always to maximize this number. In an optical imaging device the noise can be manifested is various forms. In the case of LIFT, the SNR can be evaluated for different aspects of data acquisition and

processing.

The interference pattern itself has a characteristic SNR and understanding the noise distribution in it can help with the pre-processing of the dataset. A SNR can also be calculated for the A-scan of a sample. This will determine with what confidence a response from a structure within a sample is detected. By studying the SNR of the A-scan, the nominal number of datasets needed to maximize the SNR can be determined.

Interferogram - SNR

The noise source that is present in the interference pattern observed by LIFT is predominantly the noise due to random photon fluctuations. Photon noise, a.k.a. square-root noise or Shot noise, is a manifestation of noise that exists in any photon-counting imaging device. More generally, it describes the fluctuations of the number of photons detected due to their occurrence independent of each other. This noise behaves as a Poisson distribution if a small number of photons is collected. However, if the number of photons is in excess of hundreds then the distribution of the noise tends to behave like a normal (Gaussian) distribution.

LIFT was used to capture the interferogram of the aluminum phantom placed at the focal plane of the instrument. Based on the deduction of Equation 4.4, it has been assumed that the interference pattern is a sinusoidal function with a prescribed amplitude, frequency, and phase shift. Using the method of least-squares, a theoretical sine function was fitted to the sinusoid that results from one row of the two-dimensional interference pattern. The purpose is first to evaluate the cyclic functional form of the interference pattern and second to use the model to determine the frequency of the interference. The third purpose is to determine the amplitude of the model sine function and lastly to determine and evaluate the noise distribution in the observation.

Figure 4.4 shows the observed data in black filled circles and the model fit to the data is shown in gray. As well as the residual which is the difference between the model and the observation. The model was fitted to the data with high reliability, at a $\chi^2 = 0.9$. A χ^2 value of one represents a perfect fit to the data, as the data is under-fit at $\chi^2 > 1$ and over-fit at $\chi^2 < 1$. The best fit model that was fitted to the data is a sine function with an amplitude of 2.02 and a frequency of 64.09 lines/mm.

The residual between the observation and the model interference pattern, which is assumed to be the noise in the observation, is represented in a histogram plot in Figure 4.5. The distribution of the noise in the dataset can be described by a zero-mean Gaussian with an root-mean-square of 0.42. As hypothesized, the random fluctuations in photon levels (photon noise) for a large number of collected photons tend to behave like a Gaussian distribution. The fact that the mean of the noise distribution is zero conveys that the current pre-processing, discussed previously in theory, is sound.

Based on the above analysis, the observed intereference pattern signal is determined to be 2.02 and the noise level is determined to be 0.42. Therefore, the SNR of the observed interference pattern for an aluminum phantom placed at the focal plane of LIFT is 4.81. Deeming SNR > 3 to be a confident detection, the useful signal in the observed dataset is determined to be adequate.
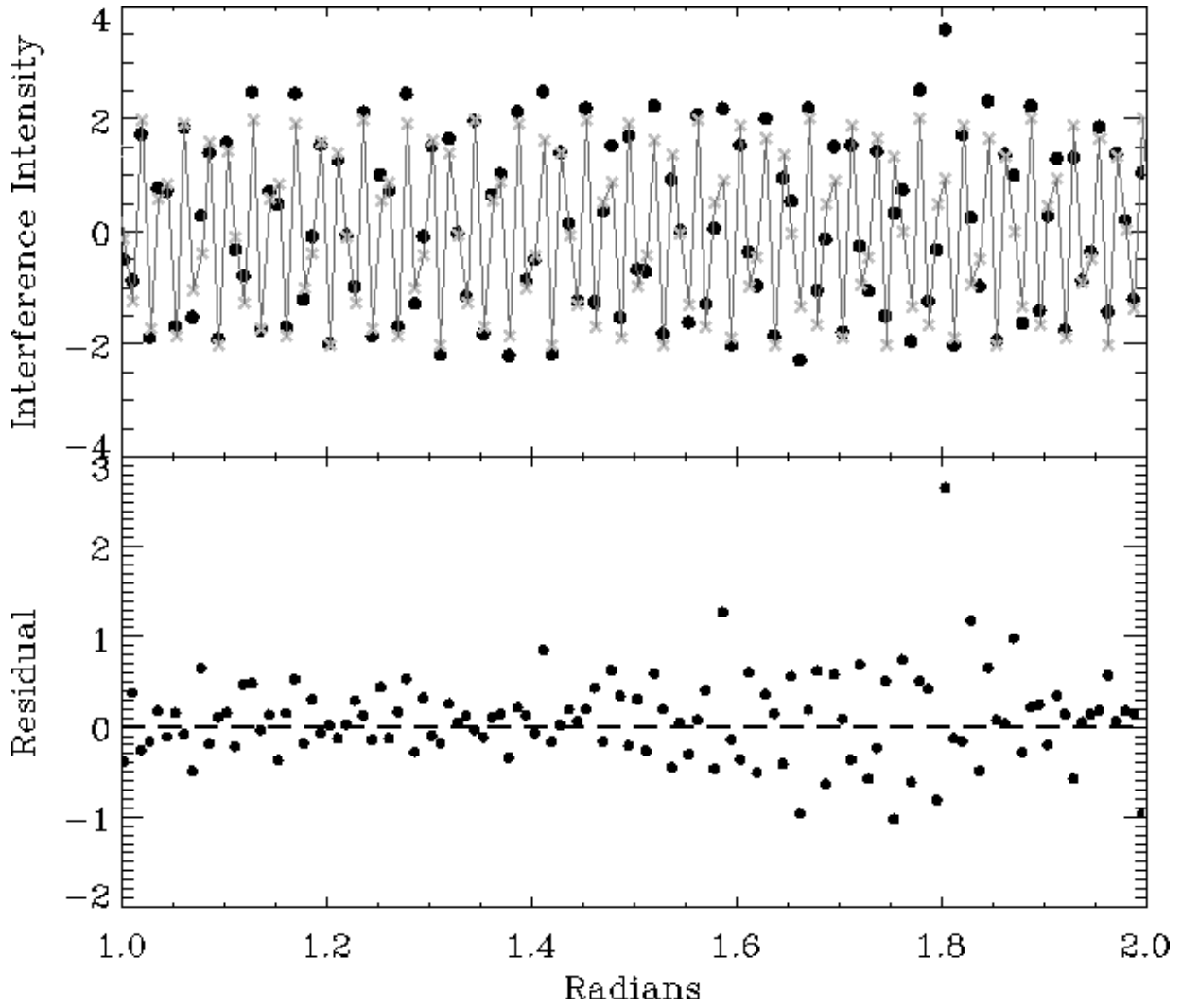
Figure 4.4: The top panel of the plot shows a zoomed in section of the measured interference pattern (black filled circles) and the least-squares fit to the data (gray). The bottom panel of the plot shows the residual when the measured and the modeled sinusoids are negated from each other.
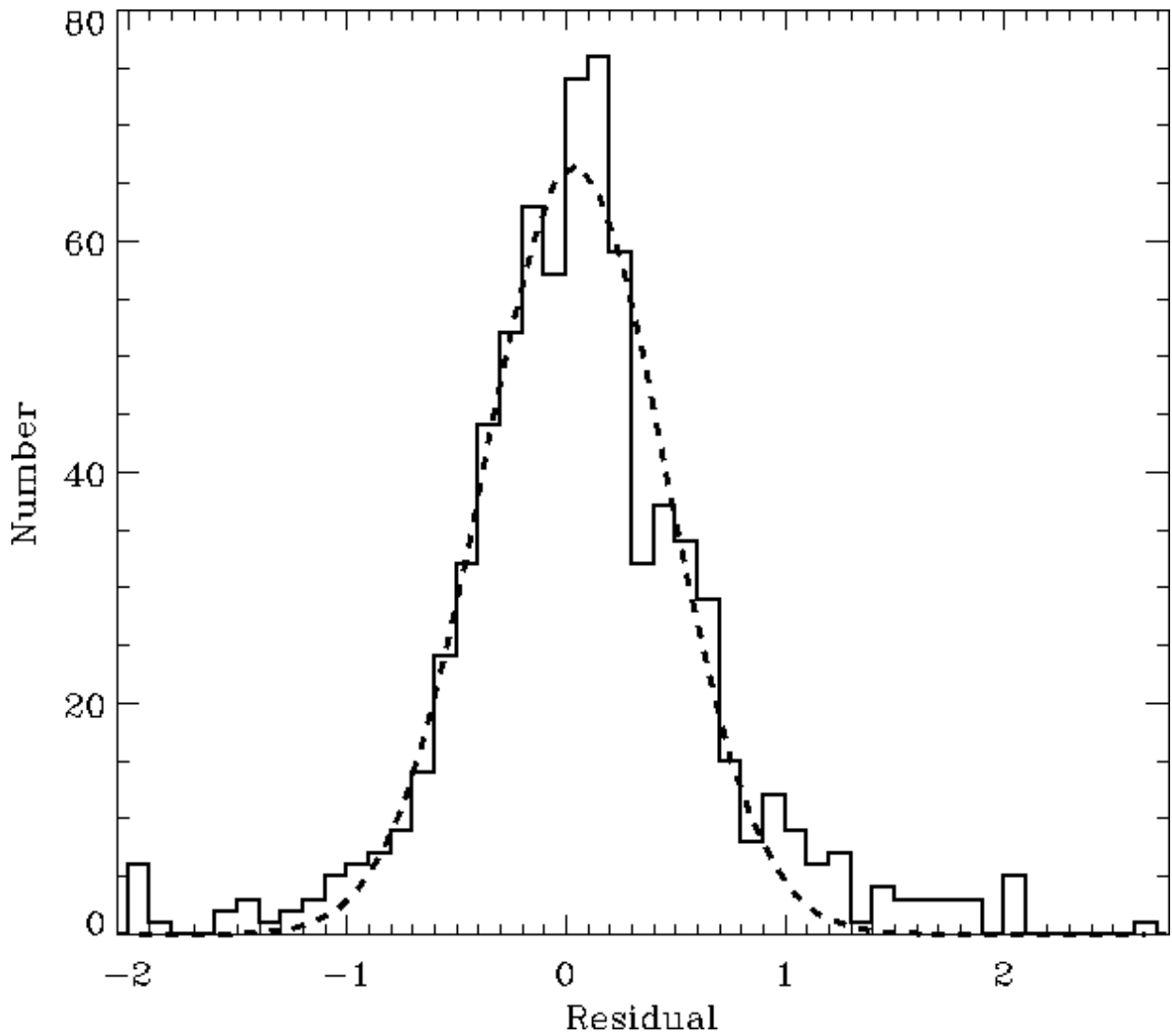
Figure 4.5: The residual from the fit shown in Figure 4.4 is plotted in this histogram. The dashed line is the Gaussian model fitted to the histogram.

A-scan - SNR

Previous sections showed that the pre-processed observations made using LIFT are solid, and also that the pre-processing pipeline is performing appropriately. The pre-processed data from the aluminum phantom placed at the focal plane of LIFT is put through the processing pipeline and the resulting A-scan is shown in Figure 4.6. To determine the SNR of the A-scan, one must evaluate the quotient of the intensity value at the peak of the detection and the mean intensity level of the A-scan floor. The peak intensity value is measured to be 6.94 and the mean noise floor is measured to be 0.43, which determined the SNR to be ~ 16. The SNR of the A-scan is about three times larger than the SNR of the interference pattern.
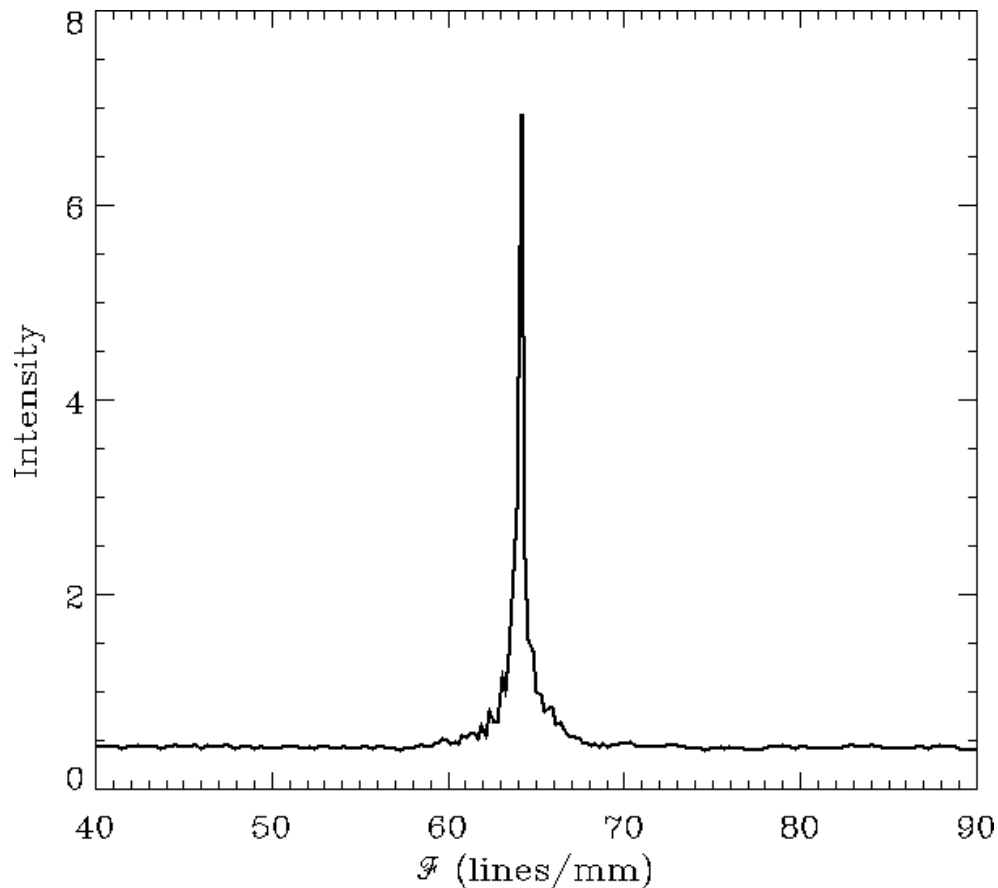
Figure 4.6: A-scan of the surface of a sandblasted aluminum block placed at the focal plane of LIFT.

Optimizing A-scan SNR

Another important step in improving the data collection and processing of LIFT is to determine the minimum number of datasets needed to improve the SNR in the A-scan of a sample. In order to achieve this goal, a series of 11000 one-dimensional interferograms were individually processed to produce A-scans. These A-scans were accumulatively averaged and the SNR of the resulting A-scan was measured for each new sample size similar to the method described in § 4.3.1. The aluminum phantom placed at the focal plane of LIFT is being probed here.
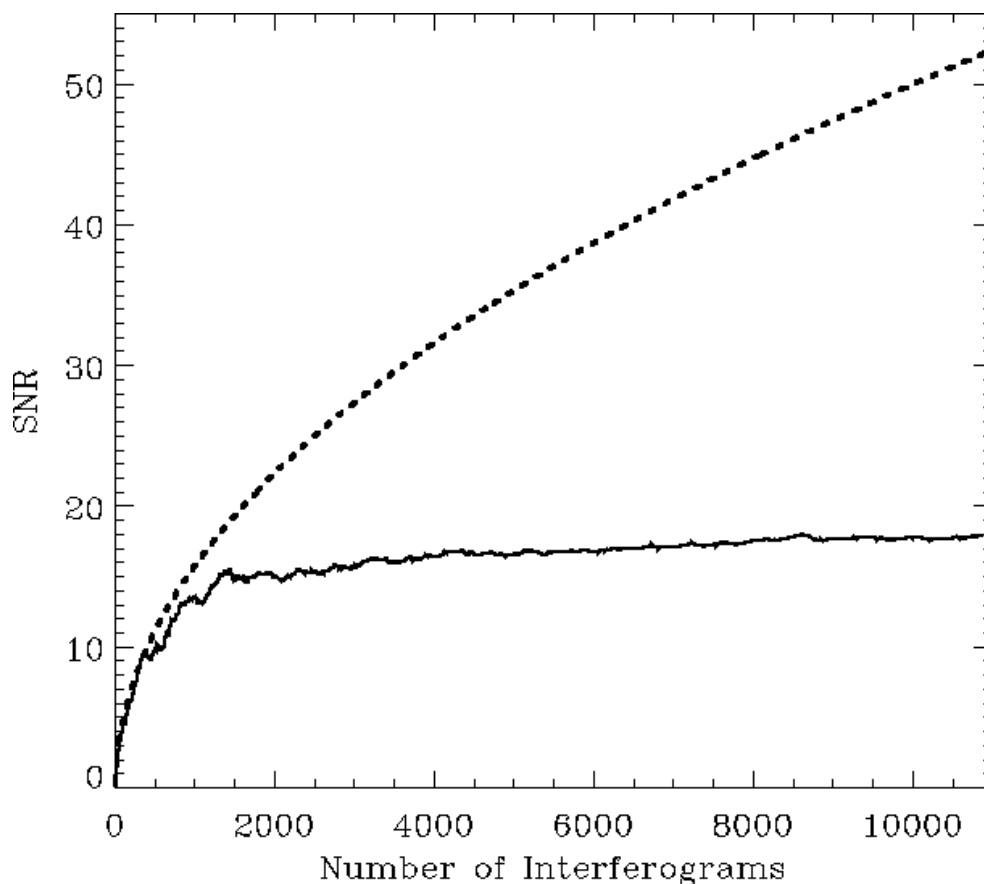
Figure 4.7: The behavior of the SNR of the average A-scan as the number of one-dimensional interferograms is accumulatively increased is shown as the solid line, and the expected (theoretical) SNR is shown as the dashed line.

Figure 4.7 shows the variation in the SNR as the number of independent interferograms processed increases. The measured value of the SNR tends to follow the structure of

the ideal, theoretical SNR curve and increase indefinitely. However, its increase tends to slow down with increasing number of interferograms averaged. At about 1500 - 2000 interferograms processed, the SNR seems to find a mean value of 16 ± 0.5. The difference in SNR between 1,500 and 11,000 interferograms is one. The collection, storage, and processing of the additional 9,500 interferograms is a process that is very time consuming, and taxing on computer storage and processing power. Therefore, increasing the number of the interferograms average to produce an A-scan beyond $\sim 2,000$ presents marginal gain.

Each two-dimensional interferogram recorded by LIFT contains 480 rows of one-dimensional sinusoidal interferograms. Assuming 90 % of these 480 interferograms has $\mathcal{V} > 0.75$, then only five captures at any given location on the sample being probed is needed. The total number of independent interferograms will allow for a 'depth profile' to be determined reliably as well as establishing time constraints on the data acquisition of LIFT.

Comments

It is worth comparing the fringe frequency peaks for an aluminum phantom that is placed at the focal plane of LIFT, determined by three independent methods. The peak of the fringe frequency can be determined using the mathematical relationshipin Equation 3.12 that was derived when theorizing the instrument. It is modeled by fitting a sinusoid to the interference pattern and is measured by performing the FFT on the pre-processed data. The fringe frequencies which correspond to the detection of the aluminum phantom for each method are shown in Table 4.1.

Table 4.1: Fringe frequencies due to the detection of a aluminum phantom at the focal plane of LIFT.

Method	$\mathcal{F}$
Theory	64.04
Model	64.09
Observation	64.05

All three methods of determining the fringe frequency are in almost perfect agreement. In addition, this exercise validates the method of aligning the system which consists of examining the separation of the two pupil beams at a large distance from the mask, as described earlier in the document.

4.3.2 Imaging Resolution

One of the most important characteristics of any imaging device is its resolution or resolving power. Imaging resolution determines the device's ability to clearly define a structure of a certain size. The limiting size that can be clearly observed is the resolution. In LIFT, two resolution limits were defined. These can be experimentally determined.

Axial Resolution

The axial resolution of LIFT was calculated using Equation 3.26 to be 80 μm. Using the LIFT prototype, the axial resolution was experimentally determined to be 40 μm. This quantity was measured by displacing the aluminum phantom in 20 μm steps, in both directions, from the focal plane of LIFT. At each step an A-scan was measured. The result of this experiment is plotted in Figure 4.8.

It is evident that the A-scans measured as a result of the displacement of 20, 60, and 100μm do not correspond to those depths. They in turn represent the 0, 40, and 80 μm depths. This is because the displacement of any distance not divisible by 40 is registered on the detector as an interference pattern of a similar frequency to the previous nearest distance divisible by 40.Note that this axial resolution corresponds to observing an additional fringe on the detector.

The actual axial resolution kernel of LIFT can be determined considering the shape of the A-scan of the aluminum phantom. The half-width of the $\frac{1}{e^2}$ waist of the Gaussian profile observed when acquiring an A-scan of the aluminum phantom is the axial resolution of LIFT. The half-width of the waist is measured to be 4.5 fringes and at 40 μm per fringe, the imaging axial resolution of LIFT is $\sim$ 180 μm.
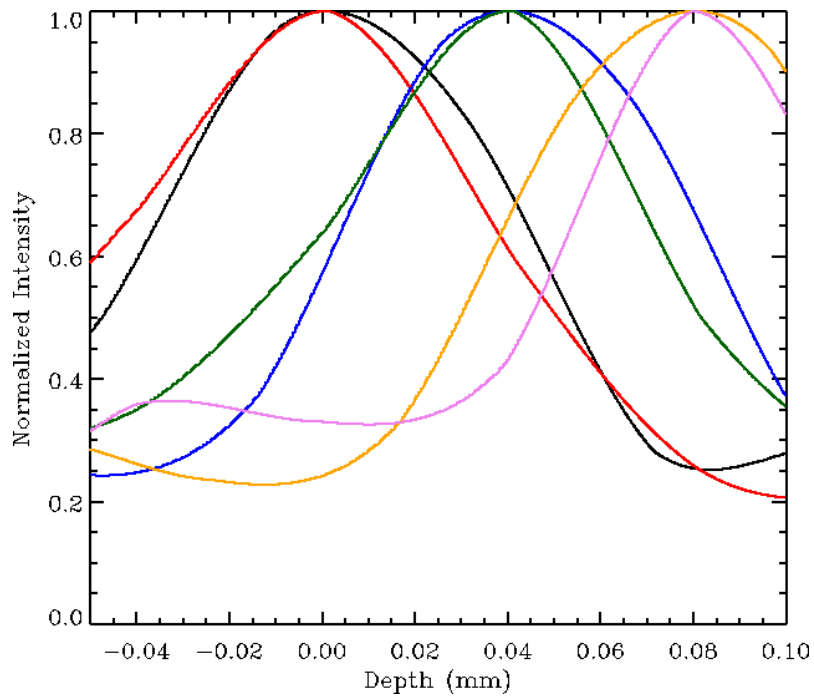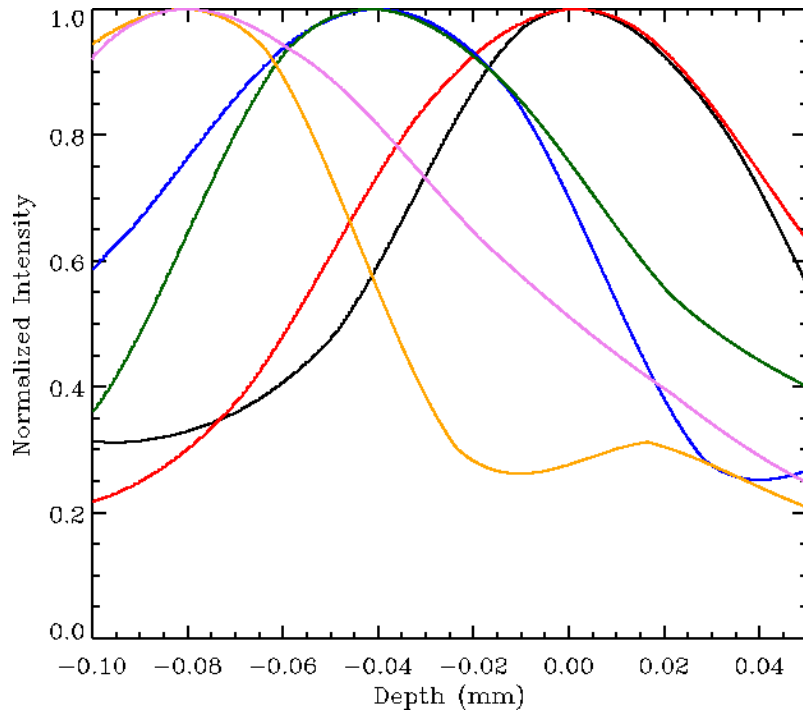
Figure 4.8: Zoomed A-scans at 20μm steps toward the lens (top), and away from the lens (bottom). In both plots the A-scan at the focal plane is in black and 20, 40, 60, 80, and 100 μm A-scans are in red, green, blue, pink, and orange, respectively.

Lateral Resolution

The lateral resolution of LIFT was defined as half of the focused spot size of the laser light source. This resolution element was calculated theoretically to be 26 μm. The actual spot size of the focused laser light was measured using the detector and is shown in Figure 4.9.

Figure 4.9: An image of the focused spot of LIFT. The gray dashed circle shows the aperture where the diameter of the spot is measured which is twice the lateral resolution of LIFT.

A circular aperture is fit to the observed spot by visual inspection. The diameter of the fitted circular aperture (spot size) is measured to be 14 pixels. At a 6 μm pixel width, the focused spot size of the laser light source in LIFT is 84 μm. Therefore, the lateral resolution of LIFT is measured to be 42 μm. The nominal uncertainty in this measurement is very small as the detector needed to be placed within the depth of field of LIFT which is 3 mm. However, an uncertainty of one pixel is assigned to the diameter of the spot measured on the detector. Permutating this uncertainty along the lateral resolution of LIFT can be determined with high confidence to be $R_l = 42 \pm 3$ μm.

4.3.3   Imaging Depth

The maximum theoretical imaging depth window was calculated to be ~ 7 mm assuming no depletion of photons returning from deeper within the sample, that the size of the relay and manipulating mirrors are large enough for highly deflected pupil beams, and that the size of the pupils are large enough for the two beams to still overlap after large deflections.

Experimentally the maximum imaging depth for LIFT is measured to be ~ 1.5 mm. The limiting factor is the size of the pupils, as the two beams will have to be overlapping

on the detector for an interference pattern to form. After a large enough deflection in front of or behind the focal plane, the two beams do not overlap and no interference pattern is observed. The two beams overlap each other and create an interferogram while the aluminum phantom is 800 μm and 600 μm in front of and behind the focal plane.

Figure 4.10 shows the A-scans recorded as the result of probing the aluminum phantom at 0, $\pm$ 200, $\pm$ 400, $\pm$ 600, and -800 μm depth. Beyond -800 and +600 μm no interference pattern was observable.
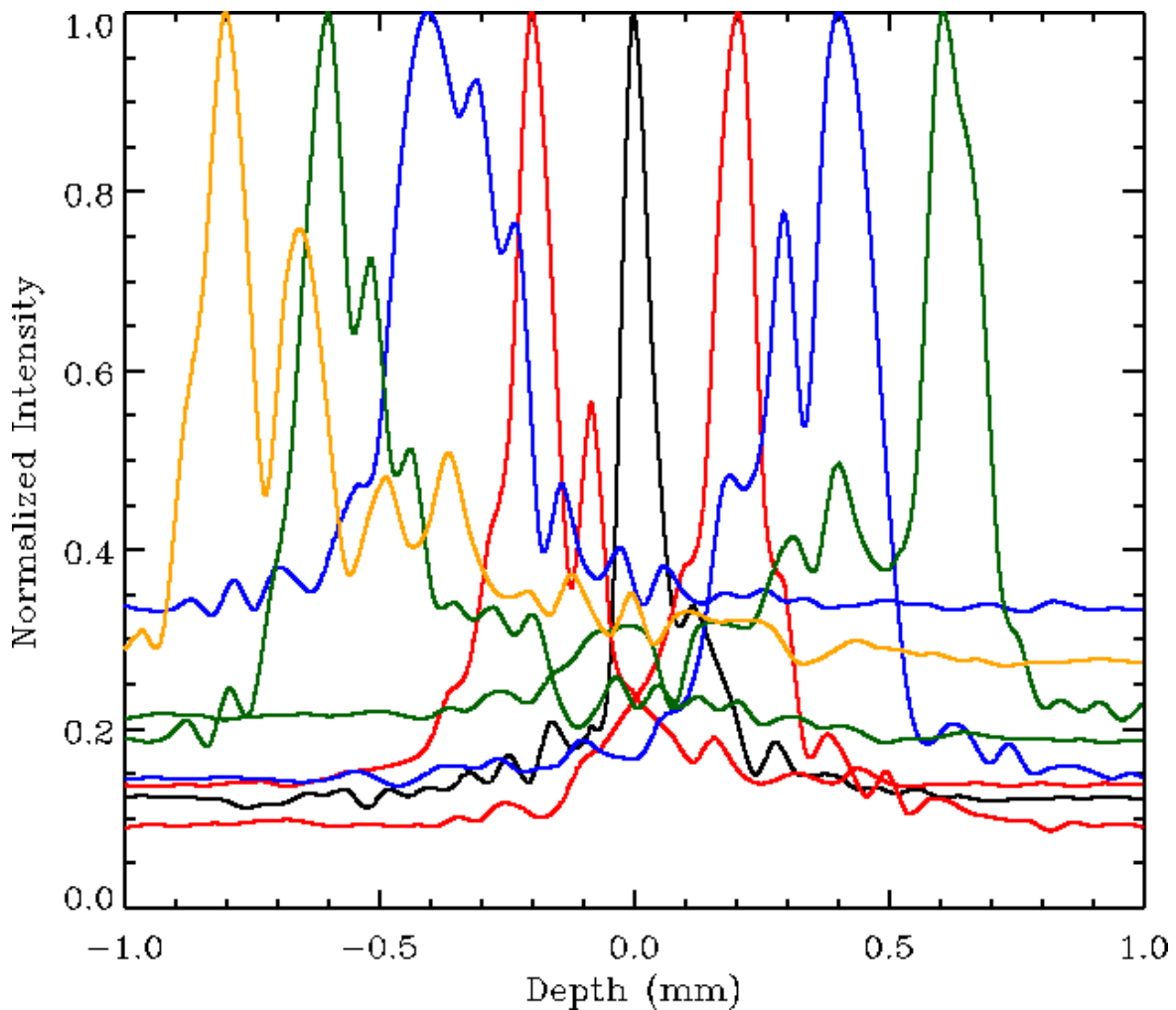

Figure 4.10: The A-scans of the aluminum phantom placed at 0 (black), $\pm$ 200 (red), $\pm$ 400 (blue), $\pm$ 600 (green), and -800 (yellow) μm.

4.4 Imaging Tests

With a working instrument, a procedure in place to image a sample, and a processing pipeline to extract meaningful information from the interferograms, some imaging tests were performed with the LIFT prototype using various materials. A sand-blasted aluminum block serves as a aluminum phantom because most of the light will be scattered off of the surface so penetration of the light is minimized. A microscope specimen slide was shaved down to 350 μm thickness and sanded on both sides. Being transparent at optical wavelengths, glass can be easily used as a spacer. Sanding both sides of the slide would create two surfaces separated by a known thickness where the light would scatter from. Lastly, to examine LIFT's imaging capabilities of tissue, a sample that had optical characteristics similar to human breast tissue was imaged. Some of the phantoms imaged with LIFT, shown in this section, are also imaged with an OCT system for verification. Optical coherence tomography (OCT) is a form of interferometric imaging often used in medical applications. OCT systems are able to provide imaging at micron-level resolution and can achieve imaging depth of $\sim$ 3 mm [13].

4.4.1 Aluminum Block

The first imaging test was done using a sand-blasted aluminum block (aluminum phantom). By moving the surface away from the focal plane, different interference patterns were observed and registered. In a way, a metal block could act as a good calibrator for LIFT. In this test, the interference pattern produced by the block at the focal plane and $\pm$ 240 μm from the focal plane was registered.

The surface of the block was first placed at the focal plane. Using a digital micrometer attached to the linear stage, the sample was moved closer and farther from the lens by 240 μm from the focal plane. At each location, a depth profile was captured. Figure 4.11 shows the resulting one-dimensional interference pattern at each depth. By inspecting these three sinusoids, it is clear that the signal returning from the focal point is strongest followed by the signal returning from behind the focal plane and then in front of the focal plane. The interference patterns seem to be stable in frequency but have fluctuations in intensity. This can be attributed to the under- and over-density of photons registered on the detector, also referred to as *speckle noise*. Speckle noise is a manifestation of the spatial coherence of the

light and is a characteristic noise associated with laser light sources.
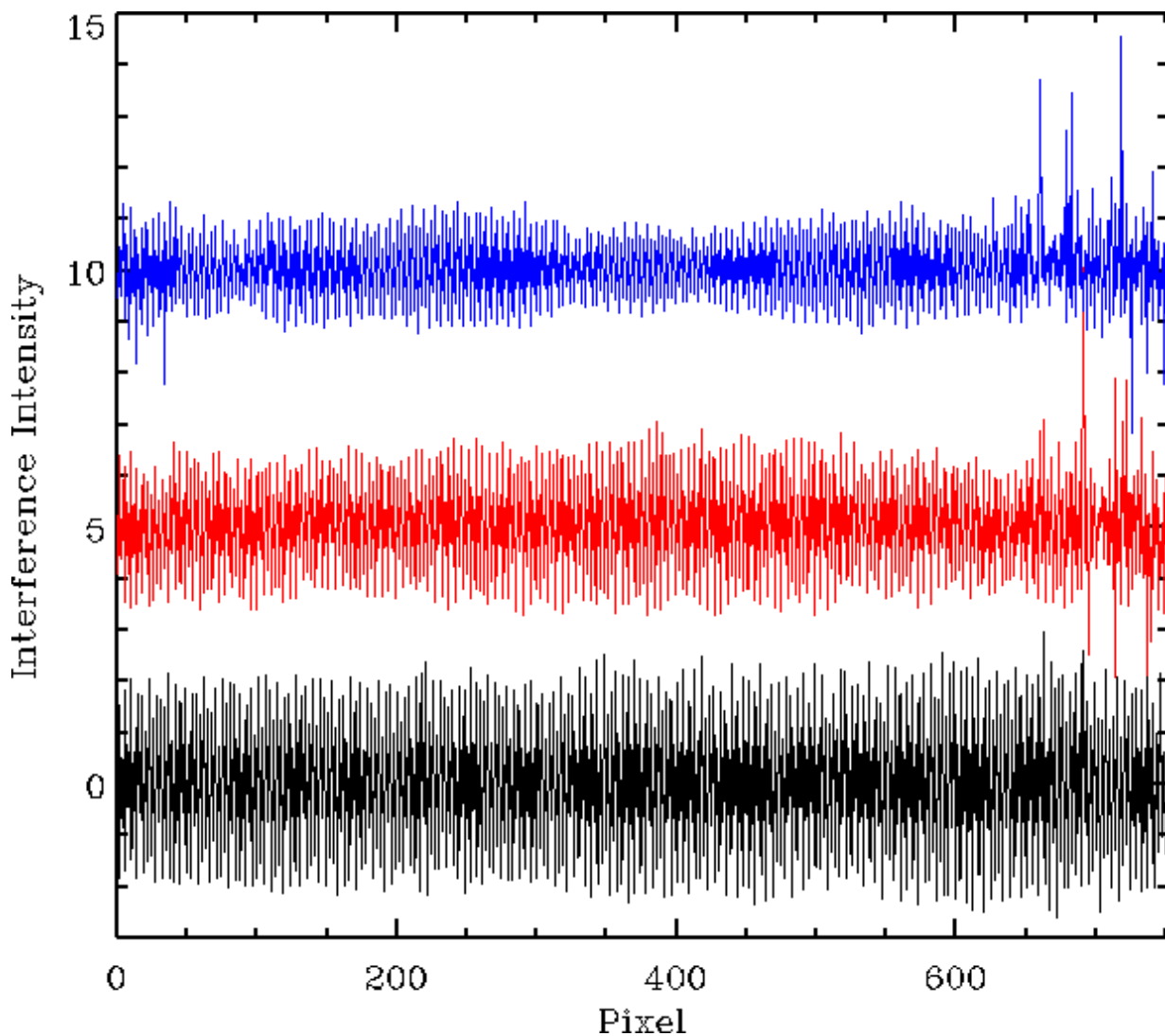
Figure 4.11: The sinusoidal interference pattern at -240 μm (blue), 0 μm (black), and +240 μm (red). All interference patterns oscillate about zero intensity but have been off-set in the vertical direction in the plot for ease of visualization.
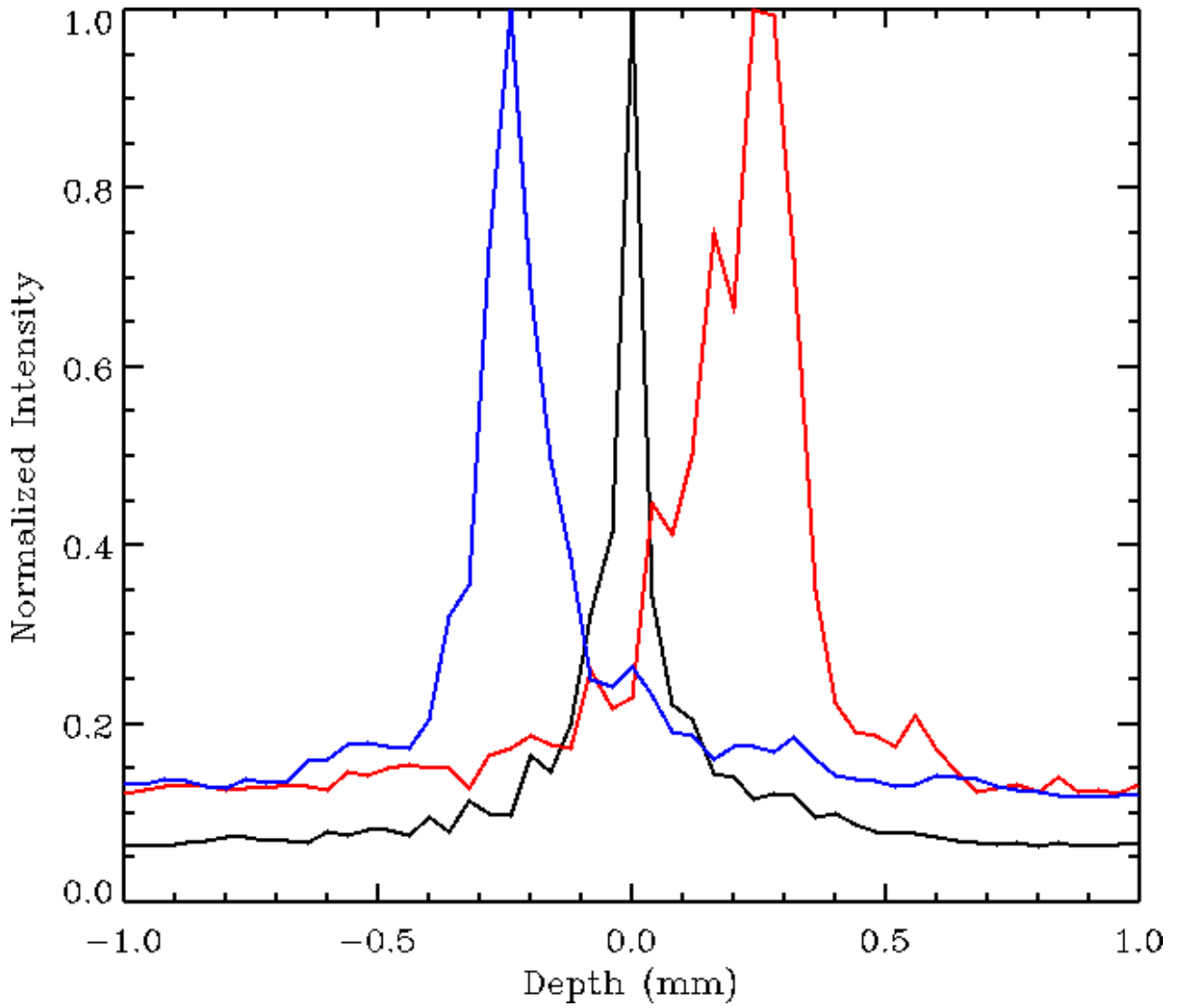
Figure 4.12: The intensity-normalized A-scan of the three interference patterns: -240 μm (blue), 0 μm (black), and +240 μm (red).
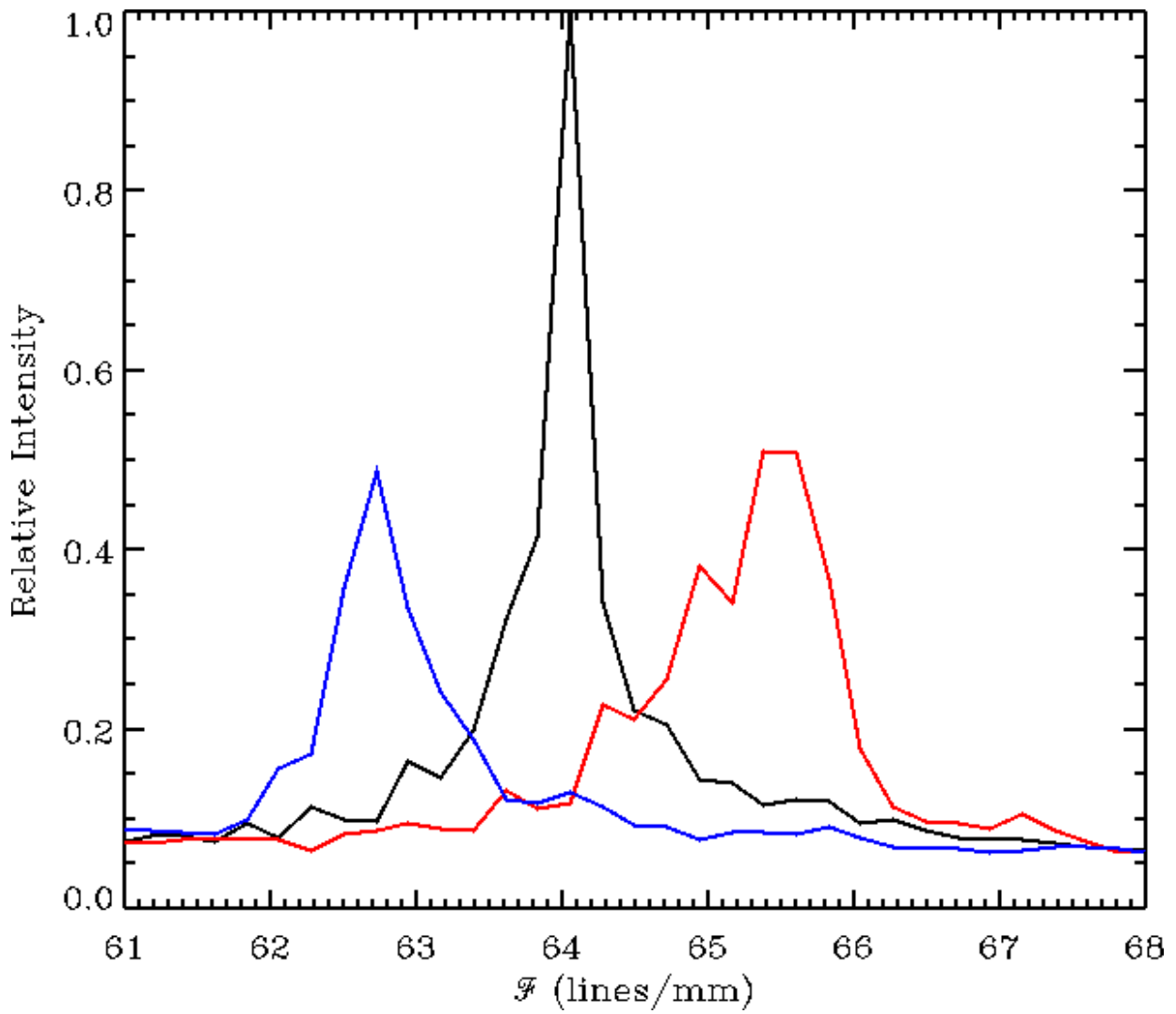
Figure 4.13: The fringe frequency ($\mathcal{F}$) of the three interference patterns: -240 μm (blue), 0 μm (black), and +240 μm (red).

Figures 4.12 and 4.13 show the A-scans of the metal block situated at the three different depths. The A-scan is shown in normalized intensity units to first demonstrate that the peak of all curves are at the correct depth location (0 and $\pm$ 240 μm) and second, for easier visualization of the noise level for each A-scan. The SNR of each A-scan is measured to be 15.97 for 0 μm, 8.09 for +240 μm, and 7.70 for -240 μm depths.

With a careful inspection of Figure 4.11, it can be seen that the fringe frequency increases going from the blue to black and on to the red sinusoid. Figure 4.13 shows the fringe frequency of each A-scan. Therefore, it has experimentally been shown that the fringe frequency decreases and increases as the sample is moved in front and behind the focal plane (towards and away from the lens).

4.4.2 Glass Slide

The next step in imaging with LIFT is to image a sample with a known thickness. The most important aspect of this experiment is to see if two layers that would scatter light, separated by a known thickness, can be detected using LIFT. Glass would serve as a suitable spacer between two layers because visible laser light would carry through it, unobstructed, and not interact with any structures within.

As a result, a new sample was constructed by shaving down a microscope specimen slide to 360 μm and sanding the exposed surfaces. This sample was then imaged by LIFT as well as an OCT system used for tissue biopsy. The result is shown in Figure 4.14. Both systems were able to detect the surfaces of the sample with the correct separation. The OCT depth profile was attained in order to verify the measurements made by LIFT. As seen in Figure 4.14, the depth profiles demonstrate some degree of correspondence. The intensity of the first peak is higher than the second because the change in the index of refraction going from air to glass would result in higher scattering than the opposite. The difference between the two A-scans is that the OCT measurement has much higher SNR than the LIFT measurement.
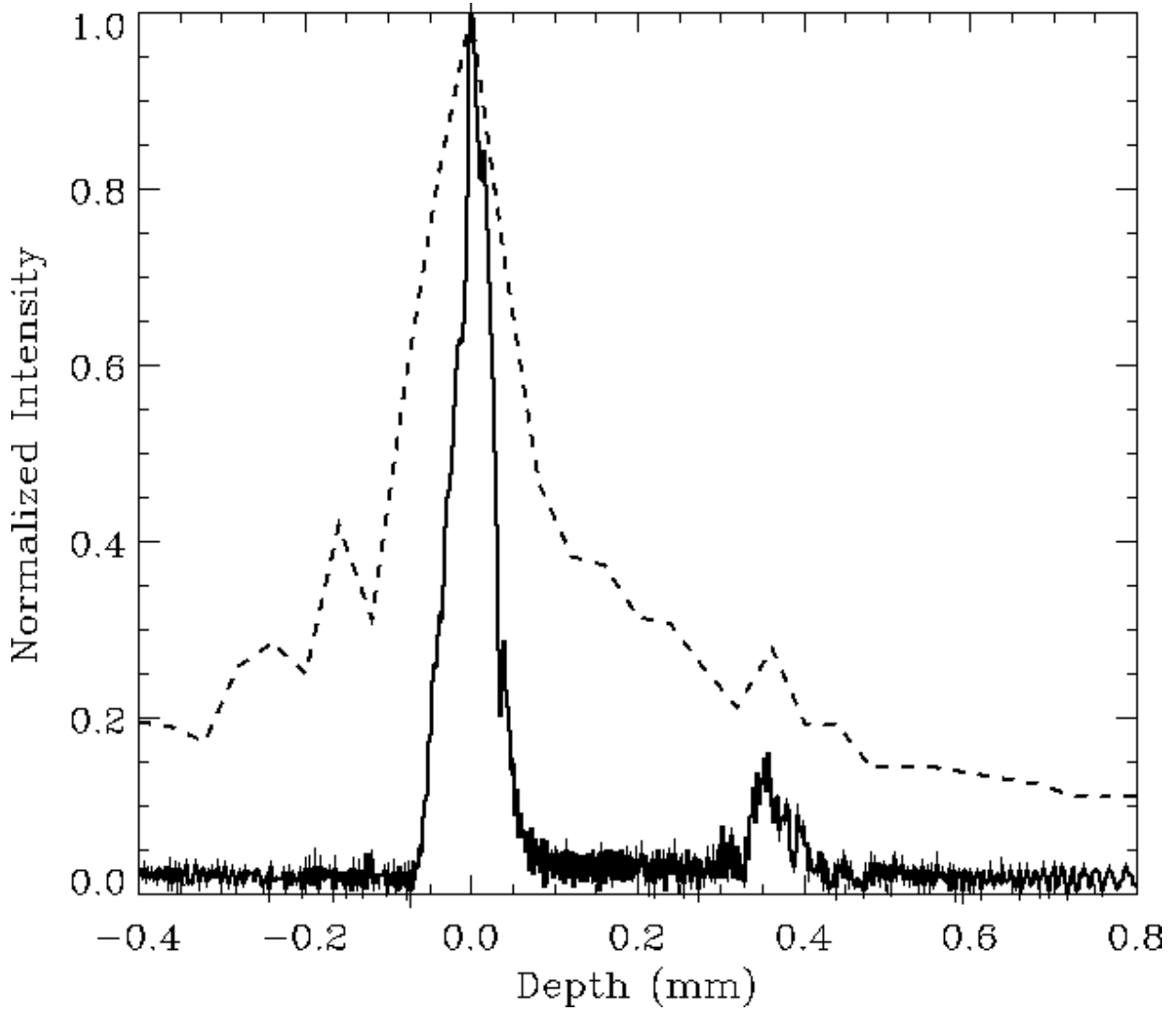
Figure 4.14: The A-scan of a 360 μm-thick glass sample imaged with an OCT (solid) and LIFT (dashed).

82

4.4.3 Human Breast Tissue Analog

For the last experiment in the proof-of-principle phase of this instrument, a sample with identical optical properties to that of human tissue was used. Along with imaging a more realistic sample, the goal was to acquire a B-scan of this sample. The sample was machined to have a staircase shape with prescribed height for each step (see Figure 4.15 middle). To be able get a B-scan of this sample, the sample had to be translated. The goal was to see the step structure of the phantom and to see the bottom of the sample by placing the sample on a highly scattering material, such as the aluminum block.
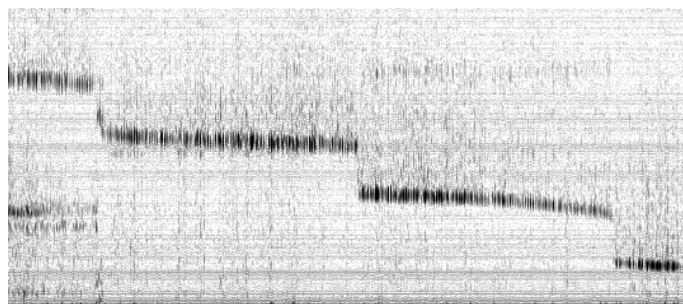
Figure 4.15: The B-scan of the staircase pattern of the human tissue analog sample imaged with LIFT (top) and with an OCT (bottom). The actual shape of the sample is shown in the middle.

This sample was probed with LIFT and with an OCT system for verification. Figure 4.15 shows the images taken by LIFT (top) and the OCT (bottom). Although the image of the staircase shape from LIFT is not as clear as that of the OCT, the step pattern is visible and discernible. Both B-scans correspond very well with the actual shape of the sample. The LIFT image seems to be very noisy compared to the image from the OCT. The noise level in the LIFT B-scan should be reduced with better pre-processing and processing of the data.

Chapter 5

Conclusions

Interferometric imaging is an established method used in many fields of science and medicine. In Laser Interference Fringe Tomography the simplest form of interference is being used to inquire about the internal structure of a sample. This form of interferometry was discovered in the mid-1800s and is a part of mainstream university physics labs. The chief benefit of this mode of imaging is that the instrument is very simple and extremely cost-effective. The imaging capabilities of the LIFT instrument complement the capabilities of the commercially available interferometric imaging devices by being a mid-resolution imager with modest tissue penetration capabilities as well as being very cost-effective.

The aim of this project was to invent a new imaging technique along with a functioning device, mathematically understand and model the device, carry out a proof-of-principle study of the performance of the LIFT instrument, and to evaluate its commercialization potential.

As described in the design and imaging chapters, LIFT is a very easy instrument to build and use. The limited number of critical optical elements reduces the alignment constraints in the device. This means that no elaborate alignment procedures are necessary before using the instrument which will allow for quicker setup time, data acquisition, and processing. Almost all components used in the instrument are standard off-the-shelf components that are readily available through any optical component provider. The instrument has an overall size of $60 \times 50 \times 50$ cm (L×W×H) and can produce A-scans of 42 μm lateral resolution and 40 μm axial resolution with $\sim$ 1.5 mm detection depth.

The instrument can be very elaborately described and modeled via mathematics which aids to gain a deeper understanding of the behavior of LIFT. There is almost exact agreement with the theoretical predictions, modeling results and the actual measurements made with LIFT. It was discovered that the sub-system that drives all other design criteria in an imaging system is the data acquisition back-end, the camera. It is discussed how some attributes of LIFT, such as axial resolution and the overall size, are effected based on the choice of detector for the LIFT prototype.

The wavelength at which LIFT is to be operated for optical microscopy is chosen to be around 650 nm. At this wavelength the light can more readily penetrate materials such as any living tissue. For other applications of LIFT like inspecting a Silicon wafer for faults, an infra-red light source will have to be used and the optical components will have to be adapted to suit. Other applications can be sought out after for such interferometric microscope and all the components in the device have to be adapted accordingly.

LIFT is designed to be a very stable and robust instrument. The imaging results of the instrument stay invariant under a slight mis-alignment of the optical components, wavelength fluctuations of an inexpensive light source, and minimally pre-processed datasets. The instrument is capable of producing reliable results under these conditions. The processing pipeline of LIFT is simple and adaptable and can be handled by any image processing software (such as IDL, MATLAB, etc.).

Starting with a very simple sample, an aluminum block, and moving on to a more realistic tissue-like sample, the imaging capabilities of LIFT were tested. Attaining A-scans of the metal block at different distances from the focal plane shows that the principles upon which LIFT was based upon and mathematically formalized are sound. The successful imaging of a glass sample with two scattering surfaces separated by a known thickness is very encouraging. Finally, reproducing OCT results of a tissue-like sample with LIFT demonstrates the full functionality and versatility of the instrument.

In most cases, when designing a new instrument for an already established field such as imaging microscopy, it is imperative that the instrument can compete with the existing technology. LIFT has the potential to compete with such systems as far as imaging capabilities go with a few modifications. Having said this, LIFT might never have comparable performance capabilities as some of the more established instruments in consumer market,

though it does have a much lower cost than its commercial counterparts.

The work presented in this document has demonstrated the successful inception, modeling , design, and performance testing of a new imaging modality and instrument. It can be considered as a successful proof-of-principle of LIFT imaging modality as well as demonstrating that LIFT is a commercially viable option. Bringing LIFT out of an academic setting and into a commercial setting would exponentially accelerate the development of this device. Fully developing this instrument would not only benefit the commercial partner, it would also provide a more cost-effective means for imaging microscopy.

Some of the results presented in this document were presented at 2011 SPIE Photonics West conference (PW11B-BO405-7) in San Francisco, U.S.A. [29].

Appendix

IDL Image Processing Code

```
;pro process

!p.charsize = 2
!P.charthick = 1.9
!x.thick = 1.6
!y.thick = 1.6
!p.thick= 2

word = 0

if word eq 0 then goto, PLOT

file_delete, 'int.txt',  /allow_nonexistent

sample = 50

cd, '/home/farnoud/data/nova/20110622_mount_+-240um/mount_0um'
data = double(read_bmp('mount_INT_0um_'+str(0)+'.bmp'))
datal = double(read_bmp('mount_LA_0um_'+str(0)+'.bmp'))
datar = double(read_bmp('mount_RA_0um_'+str(0)+'.bmp'))
back = double(read_bmp('mount_BACK_0um_'+str(0)+'.bmp'))
for i = 1, (sample-1) do begin
data += double(read_bmp('mount_INT_0um_'+str(i)+'.bmp'))
datal += double(read_bmp('mount_LA_0um_'+str(i)+'.bmp'))
datar += double(read_bmp('mount_RA_0um_'+str(i)+'.bmp'))
back += double(read_bmp('mount_BACK_0um_'+str(i)+'.bmp'))
endfor
cd, '/home/farnoud/research/lift-nova/experiments/20110622_mount_+-240um/mount_0um'

data = data - back
datar = datar - back
datal = datal - back
data_p = (data - datal - datar) / sqrt(abs(datar*datal))
idx = where(sqrt(abs(datar*datal)) lt 5)
data_p[idx] = 0

ordata = (data+back)/50
ordatas = size(ordata, /dimensions)
vis = findgen(ordatas[1]) * 0
for m = 0, (ordatas[1] - 1) do begin
Imax = max(ordata[*,m])
Imin = min(ordata[*,m])
vis[m] = (Imax - Imin) / (Imax + Imin)
endfor
```

```
idvis = where (vis gt 0.75)
idviss = size(idvis, /dimensions)
ascan = findgen(ordatas[0],idviss[0]) * 0
for n = 0, (idviss[0] - 1) do begin
ascan += abs(fft(data_p[*,idvis[n]]) - mean(data_p[*,idvis[n]]))
endfor
ascan = ascan/sample
rawdata = findgen(ordatas[0]) * 0
rawdata = data_p[*, median(idvis)] / sample

for i = 0, (n_elements(ascan)-1) do begin
openw, 1, 'int.txt', /append
printf, 1, i, ascan[i], rawdata[i]
close, 1

endfor

PLOT:

readcol, 'int.txt', x, int, /silent
window, xs = 700, ys= 600
!p.background = fsc_color('white')
!p.color = fsc_color('black')

plot,x, int, xtitle='!9F!6 (lines/mm)', ytitle='!6Intensity', xr=[40,90], /xstyle

;write_png, 'mount_0um_ascan_F.png', tvrd(true=1)

end
```

Bibliography

[1] R. Abelson. An mri machine for every doctor? some one has to pay. *New York Times*, 2004. viii, 2

[2] S.A. Akhmanov and S.Y. Nikitia. *Physical Optics*. Oxford University Press Inc., New York, USA, 1997. 11

[3] J. Alda. *Encyclopedia of Optical Engineering: Paraxial Optics*. Marcel Dekker Inc., New York, USA, 2003. 6, 7

[4] N. Blanc. ccd versus cmos - has ccd imaging come to an end? In *Photogrammetric*, pages 131– 137, 2001. 42

[5] D.A. Boas, D.H. Brooks, E.L. Miller, C.A. DiMarzio, M. Kilmer, R.J. Gaudette, and Q. Zhang. Imaging the body with diffuse optical tomography. *IEEE Signal Processing Magazine*, 18(6):57 – 75, 2001. 6

[6] M.L. Boas. *Mathematical Methods ib the Physical Sciences*. John Wiley and Sons Inc., Massachusetts, USA, third edition, 2006. 30, 33

[7] M. Born and E. Wolf. *Principles of Optics*. Pergamon Press Canada Ltd., Toronto, Canada, sixth edition, 1986. 9, 11, 13

[8] J. Canny. A computational approach to edge detection. *IEEE Transactions on Pattern Analysis and Machine Intelligence*, Pami-8(6):679 – 698, November 1986. 60

[9] B. Cense, N. Nassif, T. Chen, M. Pierce, S Yun, B. Park, B. Bouma, G. Tearney, and J. de Boer. Ultrahigh-resolution high-speed retinal imaging using spectral-domain optical coherence tomography. *Optics Express*, 12(11):2435 2447, 2004. 3

[10] S. Chang, Y. Mao, C. Flueraru, and S. Sherif. Optical coherence tomography: Technology and applications. *Proceedings of SPIE*, 7156:715606–1 – 715606–9, 2009. 3

[11] W. Drexler and J.G. Fujimoto. *Optical Coherence Tomography - Technology and Applications.* Springer, New York, USA, 2008. 10

[12] F. Feldchtein, G. Gelikonov, V. Gelikonov, R. Kuranov, Alexander Sergeev, N. Gladkova, A. Shakhov, N. Shakhova, L. Snopova, A. Terenteva, E. Zagainova, Yu Chumakov, and I. Kuznetzova. Endoscopic applications of optical coherence tomography. *Optical Express*, 3(6):257 – 270, 1998. 3

[13] J.G. Fujimoto, M.E. Brezinski, G.J. Tearney, S.A. Boppart, B. Bouma, M.R. Hee, J.F. Southern, and E.A. Swanson. Optical biopsy and imaging using optical coherence tomography. *Nature: New Technology*, 1(9):970 – 972, 1995. 3, 77

[14] K.J. Gasvik. *Optical Metrology.* John Wiley and Sons LTD, West Sussex, England, 2002. 23

[15] N. George. Confocal microscope systems - a comparison of technologies. *Bioscience Technology*, 11:12 – 14, 2003.

[16] D. Goodman. *Handbook of Optics: General Principles of Geometric Optics*, volume 1. McGraw-Hill Inc., USA, 1995. 10

[17] J. W. Goodman. *Introduction to Fourier Optics.* Roberts & Company, Colorado, USA, third edition, 2005. 9

[18] E. Gratton and M.J. vandeVen. *Handbook of Biological Confocal Microscopy: Laser Sources for Confocal Microscopy.* Springer Science + Business Media, USA, third edition, 2006.

[19] J.E. Greivenkamp. *Handbook of Optics: Interference*, volume 1. McGraw-Hill Inc., USA, 1995. ix, 11, 12, 13, 16, 21, 23

[20] CVI Melles Griot. All things photonic. Technical report, CVI Melles Griot, 2011. 9, 10, 35

[21] P. Gross, M. Storzer, S. Fiebig, M. Clausen, G. Maret, and C. M. Aegerterc. A precise method to determine the angular distribution of backscattered light to high angles. *Review OF Scientific Instruments*, 78:033105–1 – 033105–6, 2007. 35

[22] R.D. Guenther. *Modern Optics.* John Wiley and Sons Inc., USA, 1990. 11

[23] A.R. Hajian, F. Kazemzadeh, B.B. Behr, and T.M. Haylock. A device and method for generating a fringe pattern based on the depth of a surface of a substance, October 2010. viii, 21

[24] J.C. Hebdeny, S.R. Arridgez, and D.T. Delpyy. Optical imaging in medicine: I. experimental techniques. *Physics in Medicine and Biology*, 42:825 840, 1997. 8

[25] E. Hecht. *Optics.* Pearson Education Inc., San Franciso, USA, fourth edition, 2002. 11, 12, 13

[26] P. Herz, Y. Chen, A. Aguirre, J. Fujimoto, H. Mashimo, J. Schmitt, A. Koski, J. Goodnow, and C. Petersen. Ultrahigh resolution optical biopsy with endoscopic optical coherence tomography. *Optics Express*, 12(15):3532 – 3542, 2004. 3

[27] D. Huang, E.A. Swanson, C.P. Lin, J.S. Schuman, W.G. Stinson, W. Chang, M.R. Hee, T. Flotte, K. Gregory, C.A. Puliafito, and J.G. Fujimoto. Optical coherence tomography. *Science: New Series*, 254(5035):1178 – 1181, 1991.

[28] M. E. Kaiser and J. Kruk. Fuse archival instrument handbook. Technical report, NASA, June 2009. 8

[29] F. Kazemzadeh, T.M. Haylock, L.M. Chifman, A.R. Hajian, B.B. Behr, A.T. Cenko, J.T. Meade, and J. Hendrikse. Laser interference fringe tomography - a novel 3d imaging technique for pathology. In *SPIE - Photonics West Proceedings*, number PW11B-BO405-7, San Francisco, USA, 2011. 87

[30] D. Litwiller. ccd vs cmos: Fact or fiction. Technical report, DALSA, January 2001. 42

[31] D. Litwiller. cmos vs ccd: Maturing technologies, maturing markets. Technical report, DALSA, August 2005. 42

[32] R. Loudon. *The Quantum Theory of Light.* Oxford University Press, New York, USA, third edition, 1973. 13

[33] L. Mandel and E. Wolf. *Optical Coherence and Quantum Optics.* Cambridge University Press, New York, USA, 1995. 13, 14, 15

[34] M. Mansuripur. *Handbook of Optics: Principles of Optical Disk Data Storage*, volume 1. McGraw-Hill Inc., USA, 1995. 10

[35] G. De Marchi, M. Sirianni, R. Gilliland, R. Bohlin, C. Pavlovsky, M. Jee, J. Mack, R. van der Marel, and F. Boffi. Detector quantum efficiency and photometric zero points of the acs. Instrument science report, Space Telescope Science Institute, June 2004. 42

[36] R. Paschotta. *Encyclopedia of Laser Physics and Techniology*, volume A-M. Wiley-VCH, Weinheim, Germany, 2008. 14

[37] S.A. Prahl. Optical absorption of hemoglobin. Technical report, Oregon Medical Laser Center, Oregon, USA, 1999.

[38] L.V. Wang and H. Wu. *Biomedical Optics - Principles and Imaging.* John Wiley and Sons Inc., New Jersey, USA, 2007. 37

[39] A. Wax, C. Yang, V. Backman, M. Kalashnikov, R.R. Dasari, and M.S. Feld. Determination of particle size by using the angular distribution of backscattered light as measured with low-coherence interferometry. *Journal of Optical Society of America A*, 19(4):737 – 744, 2002. 35

[40] P. Xue and J.G. Fujimoto. Ultrahigh resolution optical coherence tomography with femtosecond ii:sapphire laser and photonic crystal fiber. *Chinese Science BulletinS*, 53(13):1963 1966, 2008.

[41] A.M. Zysk, F.T. Nguyen, A.L. Oldenburg, D.L. Marks, and S.A. Boppart. Optical coherence tomography: A review of clinical development from bench to bedside. *Journal of Biomedical Optics*, 12(5):051403–1 – 051403–21, 2007. 8